MEASUREMENT OF THE $2S_{1/2}, f = 0 \rightarrow 2P_{1/2}, f = 1$ TRANSITION IN ATOMIC HYDROGEN

NIKITA BEZGINOV

A DISSERTATION SUBMITTED TO THE FACULTY OF GRADUATE STUDIES
IN PARTIAL FULFILMENT OF THE REQUIREMENTS
FOR THE DEGREE OF

DOCTOR OF PHILOSOPHY

GRADUATE PROGRAM IN PHYSICS AND ASTRONOMY
YORK UNIVERSITY
TORONTO, ONTARIO
MARCH 2020

Abstract

A high-precision measurement of the transition frequency between the $2S_{1/2}, f = 0$ and $2P_{1/2}, f = 1$ states in atomic hydrogen is presented. The interval is measured by using a fast beam of hydrogen atoms and a novel method of frequency-offset separated oscillatory fields (FOSOF), an extension of the separated-oscillatory-fields (SOF) method.

Our result for the $2S_{1/2}, f = 0 \to 2P_{1/2}, f = 1$ interval is $909\,871.7 \pm 3.2\,\mathrm{kHz}$, which is the most precise measurement of this transition to date.

The root-mean-squared charge radius of the proton, determined from this measurement, is $r_p = 0.833(10)\,\mathrm{fm}$, in agreement with the proton radius determined from muonic-hydrogen spectroscopy, and 4.2 standard deviations away from the CODATA 2014 recommended value, which is determined entirely using electrons (using hydrogen spectroscopy and electron-proton scattering).

Acknowledgements

First and foremost, I would like to thank my supervisor, Eric Hessels, for his mentorship and guidance throughout my undergraduate and graduate studies. This work would not be possible without his encouragement and optimism, knowledgeable and timely advice, and almost daily discussions about the experiment. Eric told me that a high-precision measurement of the (n=2) Lamb shift was one of his dreams since his undergraduate studies. It was my pleasure to help to make this dream come true.

I would like thank Amar Vutha for being my postdoc for the first half of my doctoral studies. In truth, Amar led initial stages of the experimental design. The FOSOF technique, the mechanical and electrical design of FOSOF regions, designing and building quenching cavities – these are some of Amar's contributionsto this experiment. Amar's contagious enthusiasm helped us to establish a very friendly, dynamic and engaging atmosphere in our group. Amar was our Wikipedia for physicists. It seemed that he knew everything (I bet this is the case!), and almost always had an intuitive explanation of difficult concepts. Currently, Amar is a faculty member at University of Toronto, and I wish him all the best. Undoubtedly, Amar will make significant contributions to the field of physics.

I would like to thank Matthew George for his helpful suggestions on parts of the experiment and open discussions on topics outside of physics. Matthew is an

enthusiastic and a passionate lecturer. His door is always open for students to drop in and ask questions, and because of that his office is almost never empty. I am thankful to Matthew for having me as a teaching assistant for multiple course that he was the course director for. I could see for myself what it means to be a true teacher.

I want to extend my thanks to Cody Storry for his valuable suggestions on the mechanical design of the Lyman-α detector and other components of the experiment. Cody established a very friendly link between his and our teams, and I personally felt that we were working as a single team. As a side effect, this allowed for easy exchange of expensive equipment. I lost count of how many times I went to PSE 308 to borrow yet another set of copper gaskets.

I would like to thank Kumar (Kumarakrishnan Anantharaman) for his valuable feedback provided during research evaluations. In my opinion, the PHYS 4061 and 4062 courses that were taught and developed under Kumar's supervision are the most carefully structured courses that the physics department has in its curriculum. These two courses are one of the reasons I decided to pursue my graduate studies in the field of atomic physics.

In my first year as an undergraduate student majoring in computer science, I had Marko Horbatsch as my physics professor. He was the one who persuaded me to change my major to physics, and since then I have never regretted this decision. I would like to thank Marko for that. Also, I would like to thank Marko for his help in understanding the behavior of the Lyman-α detector. In collaboration with Eric, Marko made significant contributions to the resolution of the proton radius puzzle.

I would like to thank Alain Marsman – a postdoctoral researcher under the supervision of Marko Horbatsch. Alain performed density-matrix calculations for

this measurement to determine frequency shifts due to various systematic effects. For example, values of the AC Stark shift for different experimental configurations were calculated by Alain.

I would like to thank Marlene and Cristalina - our department's administrative assistants. They were very helpful to resolve administrative issues that I had.

I would like to thank Kosuke Kato for working with me in the same lab for 7 years and becoming my best friend. I cannot remember how many times Kosuke, as a more experienced researcher, gave me valuable advice, helped me in the machine shop, and by his own example pushed me to work harder. Currently Kosuke is a postdoc at University of Toronto, and I wish to him to be as successful as he was in his graduate studies.

I would like to thank my friend, Travis Valdez, for working with me on this experiment. Although Travis joined the experiment several years after me, I believe that both of us contributed equally to this measurement. As an example of his contributions to this experiment, Travis designed and built magnetic-field-canceling coils and a proton deflector. In the final stages of the experiment, Travis was also in charge of the analysis of FOSOF data.

I would like to thank Taylor Skinner for his valuable advice on the experiment. Thank you for being a great friend and for enduring my unsuccessful attempts to mock New Zealand accent.

To my brothers, Alex and Nicholas, thank you for always being here for me. You give me confidence that not matter what happens, I can always rely on your support.

No words can express how grateful I am to my parents for their love and support during my graduate studies. From my mother I learned that hard work is a necessary ingredient of success. My farther, by his own example, taught me to

never give up. If not for them, I would not succeed in completing this measurement.

Most importantly, to Diliara, my beloved wife, thank you for standing by my side. Out of everyone, you had the most difficult role to play: every day, you had to endure me talking about this measurement. Thank you for your understanding, believing in me and your full support. And thank you for the best gift of all – our daughter Victoria.

Table of Contents

List of Tables

List of Figures

1 Motivation and method

1.1 The hydrogen atom and the proton radius

The hydrogen atom is perhaps the simplest electromagnetically-interacting, stable, bound system. Its spectrum can be precisely calculated and compared to measured energy differences. High-precision spectroscopy of the hydrogen atom is used to test fundamental physics.

Historically, the development of quantum mechanics was highly correlated with advancements in understanding of the hydrogen spectrum. In 1947, Lamb and Retherford [1] measured a frequency difference of 1000 MHz between the $2S_{1/2}$ and $2P_{1/2}$ states of atomic hydrogen (states that were expected to be degenerate according to the Dirac theory). This frequency difference was crucial to the emergence of quantum electrodynamics (QED) [2], the accepted framework for the description of charged particles interacting with photons. More than sixty years worth of experimental tests with ever-increasing precision have not found any conclusive deviations from QED predictions. For example, precision measurements of the electron magnetic moment [3] and the recoil frequency of cesium-133 atoms in a matter-wave interferometer [4] lead to two most precise determinations of the fine-structure constant[1]. These two determinations are

[1]The fine-structure constant sets the scale for the strength of the electromagnetic interaction between elementary charged particles.

consistent with each other.

The energy difference between the $2S_{1/2}$ and $2P_{1/2}$ states is known as the Lamb shift. The two largest contributions to the Lamb shift are QED contributions: the self-energy of the electron and vacuum polarization from virtual electron-positron pairs. The third-largest contribution is due to relativistic recoil. The effect of the proton size is the fourth-largest contribution (it contributes only 0.014% of the Lamb shift). The proton-size contribution primarily affects S states, since there is a significant overlap of the electron S wavefunction with the volume occupied by the proton. The potential inside the proton is smaller than it would have been if the proton was a point particle, and thus the binding energy of the S states becomes less negative.

The leading-order expression [5] for the frequency shift due to the proton size is

$$E_{\mathrm{NS}}/h = \frac{2}{3}\frac{m_{\mathrm{r}}^3}{m_{\mathrm{e}}^3}\frac{2\alpha^2 c R_\infty}{n^3}\frac{r_{\mathrm{p}}^2}{\lambda\!\!\!^{-}_{\mathrm{C}}^2}\delta_{l0}, \tag{1.1}$$

where m_e is the electron mass, m_p is the proton mass, $m_r = \dfrac{m_e m_p}{m_e + m_p}$, α is the fine-structure constant, c is the speed of light in vacuum, R_∞ is the Rydberg constant, r_{p} is the root-mean-squared (RMS) charge radius of the proton, $\lambda\!\!\!^{-}_{\mathrm{C}} = \hbar/(m_e c)$ is the reduced Compton wavelength of the electron, n is the principal quantum number, $\hbar$ is the reduced Planck constant (h), and δ is the Kronecker delta. Experimentally determined hydrogen-level differences, when combined with QED theory, can be used to extract the Rydberg constant and the proton radius. The other constants required are known with sufficient precision from other experiments.

The proton radius can also be determined from electron-proton scattering experiments. CODATA uses both types of data to determine the recommended value of the proton RMS charge radius [5, 6].

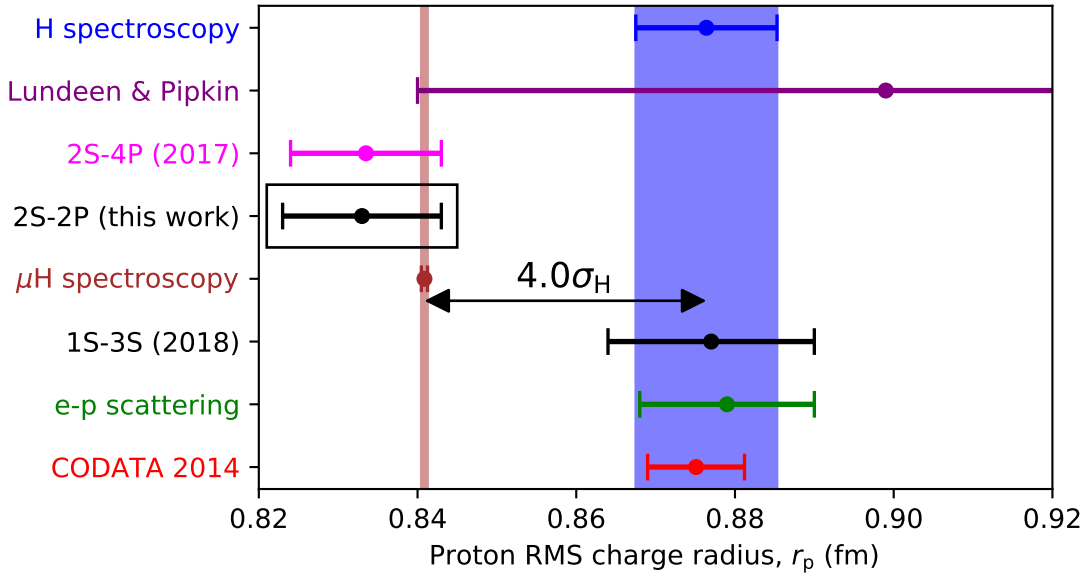

Figure 1.1: Values of the proton radius obtained from experiments. The red point is the CODATA 2014 recommended value obtained by combining the radius extracted from the electron-proton scattering experiments (shown in green), and spectroscopic measurements in hydrogen and deuterium (shown in blue, adjustment 12 in [5]). Two new values obtained from hydrogen spectroscopy in 2017 and 2018 are not included in CODATA 2014, and are shown in magenta and black, respectively. The proton radius obtained from measurements of the $2S \leftrightarrow 2P$ interval in muonic-hydrogen spectroscopy is shown in brown [8]. The purple point is the recently reanalyzed hydrogen Lamb-shift measurement performed in 1981 [9]. Note that the original value [10], used by CODATA, has a factor of 2.2 smaller uncertainty and the extracted proton radius is smaller by 0.020 fm than the reanalyzed result. The value of the proton radius extracted from this work [11] is enclosed in a rectangle.

1.2 The proton radius puzzle

In 2010, a new determination of the proton radius was extracted from a measurement of the Lamb shift in muonic hydrogen [7]. The muon is approximately 200 times heavier than the electron, and, in hydrogenic atoms, its wavefunction has about 6 million times larger overlap with the proton. Therefore, the muonic hydrogenic atom is conceptually a better system for a proton-size measurement. The muonic hydrogen measurement led to the determination of the proton radius with an order-of-magnitude smaller uncertainty than the CODATA 2010 value, and was 5.0 standard deviations away from it. This discrepancy is now known as the proton-radius puzzle, which until the time of the current measurement had no convincing resolution. The high-precision measurement of the Lamb shift in ordinary hydrogen (the measurement described in this work) is an important contribution towards resolving the puzzle.

Current determinations for the value of the proton radius are shown in Fig. 1.1. As seen from the figure, the experimentally determined value of the proton radius from muonic-hydrogen spectroscopy is 4.0 standard deviations away from the proton radius obtained from earlier electronic-hydrogen spectroscopy[2]. The value in blue is comprised of 15 measurements. The proton radii determined from these 15 experiments are shown in Fig. 1.2. The figure shows the majority (except one) of the radii are within 2 standard deviations from the muonic-hydrogen value. To test for unaccounted systematic effects, higher-precision measurements of the hydrogen spectrum should be performed.

In 2017 and 2018, two such experiments were performed by measuring 1S $\rightarrow$ 3S [13] and 2S $\rightarrow$ 4P [14] transitions, shown in black and magenta, respectively, in

[2]The deviation is 5.6σ if the electron-proton scattering data is included. However, the analysis of the scattering data is complicated, and different data analysis methods yield proton radii that agree with the muonic-hydrogen value as well [12].

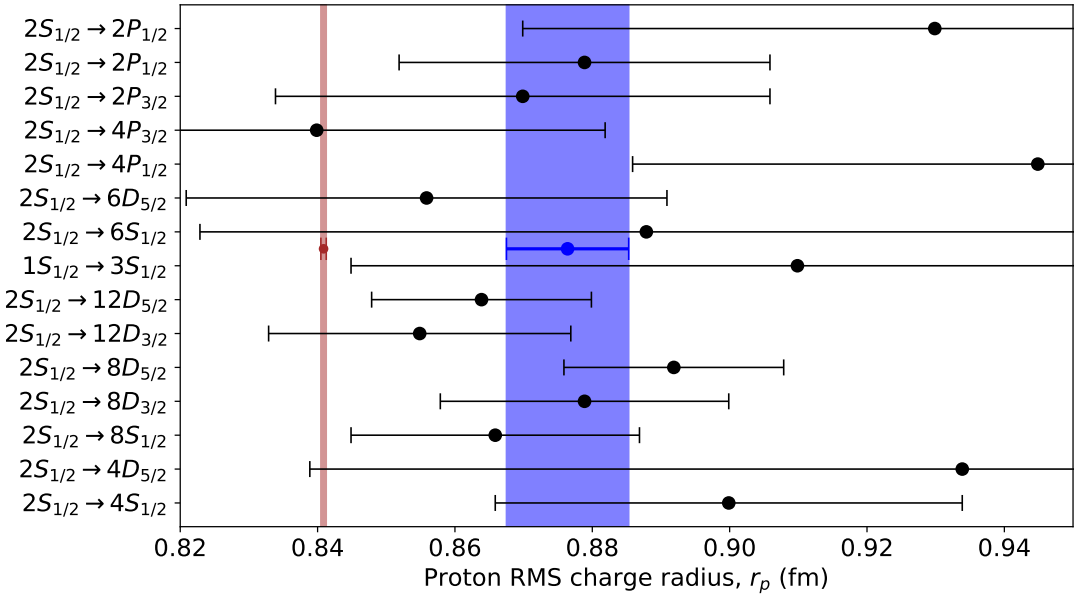

Figure 1.2: Proton radius values determined from hydrogen spectroscopy experiments. The data are obtained from Table VII of Ref. [15]. The labels on the y axis correspond to the interval that was measured and from which the proton radius was calculated. As in Fig. 1.1, the blue band is the weighted average of all of the proton radius measurements obtained from hydrogen spectroscopic experiments, and the brown band is the proton radius determined from the measurements of the $n = 2$ Lamb shift in muonic hydrogen.

Fig. 1.1. The former agrees with the CODATA 2014 value for the proton radius, and the latter is consistent with the muonic-hydrogen value. This situation demands additional high-precision hydrogen-spectroscopy experiments.

A precision measurement of the Lamb shift in ordinary hydrogen serves two purposes. It allows the direct comparison between the muonic- and electronic-hydrogen spectroscopy. Also, it adds an important data point to the set of the radii determined from the transitions measured in hydrogen, which also has the effect of testing the theory of the hydrogen atom.

1.3 The interval being measured

An energy eigenstate of hydrogen atom is denoted by

$$nL_j, f, m_f, \tag{1.2}$$

where n is the principal quantum number, L is the orbital angular momentum quantum number (represented by S, P, D, etc for the $l = 0, 1, 2, \ldots$ states), j and f are the angular momentum quantum numbers with inclusion of the electron spin, and of both the electron and proton spins, respectively. Finally, m_f is the quantum number proportional to the projection of the total angular momentum along a specified axis.

Various contributions to the $n = 2$ Lamb shift in hydrogen, as well as of the hyperfine correction for the $2S_{1/2}, f = 0 \to 2P_{1/2}, f = 1$ interval, are shown in Table 1.1, and the energy diagram is depicted in Fig. 1.3. The first column of Table 1.1 contains contributions to the Lamb shift calculated by using the CODATA 2014 values for the Rydberg constant and the proton RMS charge radius. Due to the relatively large uncertainty in the proton radius, the uncertainty of 2.1 kHz in $E_{\rm NS}$ (the contribution of the proton size) limits the uncertainty in the predicted value

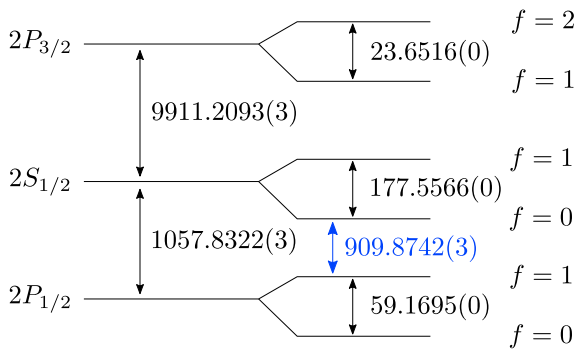

Figure 1.3: Energy levels of the $n = 2$ manifold in hydrogen. The energy differences (not to scale) are specified in megahertz. The transition frequencies are calculated by assuming the value of the proton radius from muonic-hydrogen spectroscopy. The $2S_{1/2}, f = 0 \to 2P_{1/2}, f = 1$ interval measured is shown in blue.

for the Lamb shift. The second column uses the more precise value for the proton radius from the CREMA collaboration[3], which gives a Lamb shift that is 11.5 kHz different from the shift in the first column.

The difference of 11.5 kHz corresponds to about 1 part in 10^4 of the natural linewidth of the transition[4]. Determining the linecenter by mapping out the Lorentzian lineshape to such precision poses prohibitive practical difficulties. To overcome the limitation imposed by the natural linewidth, the well-known technique of the separated-oscillatory-fields (SOF) could be used. This method was employed for the previous measurement of the $n = 2$ Lamb shift, performed by Lundeen and Pipkin [10, 23]. However, for measurement described here, we use a novel extension of the SOF technique: the frequency-offset separated oscillatory fields (FOSOF) technique [24, 25].

[3]Fixing the proton radius allows for calculation of the Rydberg constant from precisely measured $1S \to 2S$ interval [15].

[4]Due to the spontaneous decay rate of the $2P_{1/2}$ state to the ground state of $6.26 \times 10^8\,\mathrm{s}^{-1}$ [22]. This gives a 1.60-ns-long lifetime for the $2P_{1/2}$ state, and the natural width of the transition is 99.7 MHz.

Table 1.1: Leading contributions to the energy difference (in frequency units) between the $2S_{1/2}, f = 0$ and $2P_{1/2}, f = 1$ states in hydrogen. The expressions for the contributions are obtained from Refs. [5, 6, 15–20]. The first column uses CODATA 2014 values for the proton charge RMS radius, and the Rydberg constant, whereas the second column uses the more precise value of the proton radius from CREMA collaboration [8]. The numbers in parentheses are the uncertainty in the final digits shown. The $n = 2$ Lamb shift, E_{LS}, is equal to the sum of all of the contributions less the hyperfine correction.

Correction		$\Delta\nu_{\mathrm{CD}}$(kHz)	$\Delta\nu_{\mathrm{CR}}$(kHz)[c]
Electron self-energy	E_{SE}	1 084 127.9(0)	1 084 127.9(0)
Hyperfine structure	E_{HFS}	−147 958.1(0)	−147 958.1(0)
Vacuum polarization	$E^{(2)}_{\mathrm{VP}}$	−26 853.8(0)	−26 853.8(0)
Relativistic recoil	E_{SR}	357.1(0)	357.1(0)
Proton RMS charge radius[a]	E_{NS}	149.8(21)	138.3(1)
Two-photon contribution	$E^{(4)}$	65.4(3)	65.4(3)
Recoil (Dirac)[b]	E_{M}	−2.2(0)	−2.2(0)
Radiative recoil	E_{RR}	−1.5(1)	−1.5(1)
Proton self-energy	E_{SEN}	0.6(0)	0.6(0)
Three-photon contribution	$E^{(6)}$	0.4(1)	0.4(1)
$n = 2$ Lamb shift	E_{LS}	1 057 843.7(21)	1 057 832.2(3)
$2S_{1/2}, f = 0 \to 2P_{1/2}, f = 1$	$E_{\mathrm{LS}} + E_{\mathrm{HFS}}$	909 885.7(21)	909 874.2(3)

[a] Spherically symmetric charge distribution is assumed. The model has negligible dependence on the exact radial charge distribution, as long as the RMS radius is the same [21].

[b] This shift arises from the Dirac equation, as the consequence of including the reduced mass term.

[c] Only the correction due to the size of the proton is significantly different for this column.

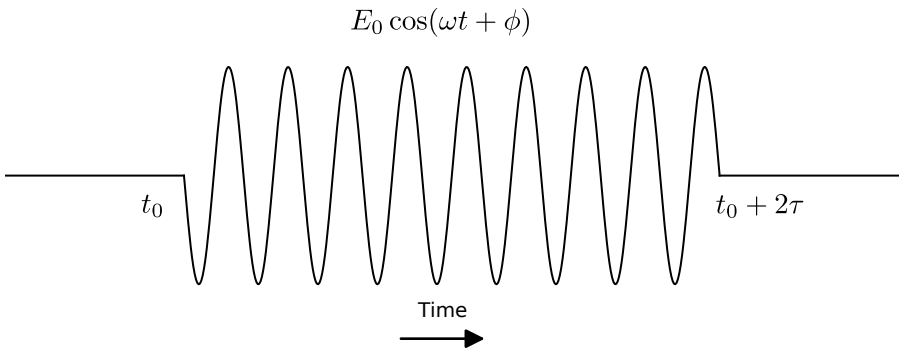

Figure 1.4: Single region of linearly polarized oscillating electric field of duration 2τ.

1.3.1 The method of separated oscillatory fields (SOF)

Consider a hydrogen atom in the $2S_{1/2}, f = 0$ state, at time t_0 exposed to a single region of linearly polarized radio-frequency (rf) electric field with amplitude E_0 and duration 2τ (Fig. 1.4). The frequency of the field, $f = \omega/2\pi$, is in the vicinity of the frequency difference $(E_1 - E_2)/h$ between the $|1\rangle = |2S_{1/2}, f = 0\rangle$ and $|2\rangle = |2P_{1/2}, f = 1, m_f = 1\rangle$ states. This system can be approximately treated as a two-level system, with the Hamiltonian represented as

$$H = H_0 + W(t), \tag{1.3}$$

with

$$H_0 = \hbar \begin{pmatrix} \omega_1 - \frac{1}{2}i\gamma_1 & 0 \\ 0 & \omega_2 - \frac{1}{2}i\gamma_2 \end{pmatrix}, \tag{1.4}$$

and

$$W(t) = E_0 p_z \begin{pmatrix} 0 & \cos(\omega t + \phi) \\ \cos(\omega t + \phi) & 0 \end{pmatrix}, \tag{1.5}$$

where the $|i\rangle$ state has an energy eigenvalue of $\hbar\omega_i$ and a spontaneous transition rate to the ground state of γ_i, $\omega = 2\pi f$, $p_z = \sqrt{3}ea_0$ is the matrix element of the

z-component of the electric-dipole-moment operator, a_0 is the Bohr radius, e is the charge of the proton, and ϕ is the phase of the electric field.

It is useful to transform Eq. 1.3 from the Schrödinger picture to the interaction picture. In this picture, the Hamiltonian for the system is:

$$W_I(t) = U_0^\dagger(t, t_0) W(t) U_0(t, t_0), \tag{1.6}$$

with

$$U_0(t, t_0) = \begin{pmatrix} e^{-i\omega_1(t-t_0)} e^{\frac{1}{2}\gamma_1(t-t_0)} & 0 \\ 0 & e^{-i\omega_2(t-t_0)} e^{\frac{1}{2}\gamma_2(t-t_0)} \end{pmatrix}. \tag{1.7}$$

Therefore,

$$\begin{aligned} W_I(t) = \frac{1}{2} &\begin{pmatrix} e^{\frac{1}{2}(\gamma_1-\gamma_2)(t-t_0)} & 0 \\ 0 & e^{-\frac{1}{2}(\gamma_1-\gamma_2)(t-t_0)} \end{pmatrix} \Bigg\{ \\ &\begin{pmatrix} 0 & e^{i(\omega_1-\omega_2+\omega)t} e^{-i[(\omega_1-\omega_2)t_0-\phi]} \\ e^{-i(\omega_1-\omega_2+\omega)t} e^{i[(\omega_1-\omega_2)t_0-\phi]} & 0 \end{pmatrix} + \\ &+ \begin{pmatrix} 0 & e^{i(\omega_1-\omega_2-\omega)t} e^{-i[(\omega_1-\omega_2)t_0+\phi]} \\ e^{-i(\omega_1-\omega_2-\omega)t} e^{i[(\omega_1-\omega_2)t_0+\phi]} & 0 \end{pmatrix} \Bigg\} E_0 p_z. \end{aligned} \tag{1.8}$$

The anti-resonant terms, of the form $e^{\pm i(\omega_1-\omega_2+\omega)t}$, are oscillating at a much higher frequency than the resonant terms, $e^{\pm i(\omega_1-\omega_2-\omega)t}$ [5]. In the rotating-wave approximation (RWA) the anti-resonant terms are omitted. The Hamiltonian in the interaction picture, with the rotating-wave approximation applied, is

$$\begin{aligned} W_I^{(\mathrm{RWA})}(t) = \frac{1}{2} E_0 p_z &\begin{pmatrix} e^{\frac{1}{2}(\gamma_1-\gamma_2)(t-t_0)} & 0 \\ 0 & e^{-\frac{1}{2}(\gamma_1-\gamma_2)(t-t_0)} \end{pmatrix} \\ &\begin{pmatrix} 0 & e^{-i(\omega t+\phi)} e^{i(\omega_1-\omega_2)(t-t_0)} \\ e^{i(\omega t+\phi)} e^{-i(\omega_1-\omega_2)(t-t_0)} & 0 \end{pmatrix}. \end{aligned} \tag{1.9}$$

[5] To reiterate, the assumption is that the field angular frequency, ω, is close to the resonant angular frequency of the transition, $\omega_1 - \omega_2$.

Transforming Eq. 1.9 back to the Schrödinger picture, gives

$$W^{(\mathrm{RWA})}(t) = \frac{1}{2} E_0 p_z \begin{pmatrix} 0 & e^{-i(\omega t+\phi)} \\ e^{i(\omega t+\phi)} & 0 \end{pmatrix}. \tag{1.10}$$

The Schrödinger equation, with the Hamiltonian $H^{(\mathrm{RWA})} = H_0 + W^{(\mathrm{RWA})}(t)$, can be solved exactly, and the solution is developed in Ref. [26]. The probability for the atom to remain in state $|1\rangle$ at time $t_0 + 2\tau$ is

$$P^{(\text{one pulse})} = e^{-(\gamma_1+\gamma_2)\tau} |\cos\alpha\tau + i\cos\beta\sin\alpha\tau|^2, \tag{1.11}$$

where

$$\omega_0 = \omega_1 - \omega_2; \tag{1.12}$$

$$\Omega = \omega - \omega_0; \tag{1.13}$$

$$Q = \frac{1}{2}(\gamma_1 - \gamma_2); \tag{1.14}$$

$$V = -\frac{1}{2}\frac{E_0 p_z}{\hbar}; \tag{1.15}$$

$$\alpha = (4V^2 + (\Omega + iQ)^2)^{1/2}; \tag{1.16}$$

$$\sin\beta = 2V/\alpha; \tag{1.17}$$

$$\cos\beta = (\Omega + iQ)/\alpha. \tag{1.18}$$

The spontaneous decay rate to the ground state for the $2S_{1/2}, f = 0$ state, γ_1, is almost exactly zero because of its 0.122-second-long lifetime [27], and, for the $2P_{1/2}, f = 1$ state, the spontaneous decay rate to the ground state is $\gamma_2 = 6.26 \times 10^9\,\mathrm{s}^{-1}$ [22]. The plot of the $2S_{1/2}, f = 0 \rightarrow 2P_{1/2}, f = 1$ transition probability in a single square region of electric field as a function of frequency for $2\tau = 19.4\,\mathrm{ns}$ and $E_0 = 14\,\mathrm{V/cm}$ is shown in Fig. 1.5 in dashed black. The lineshape is centered at the resonant frequency, but the resonance is quite broad.

For the method of separated oscillatory fields (SOF), instead of applying a single pulse for duration 2τ, two pulses of equal duration τ are used, with a time interval

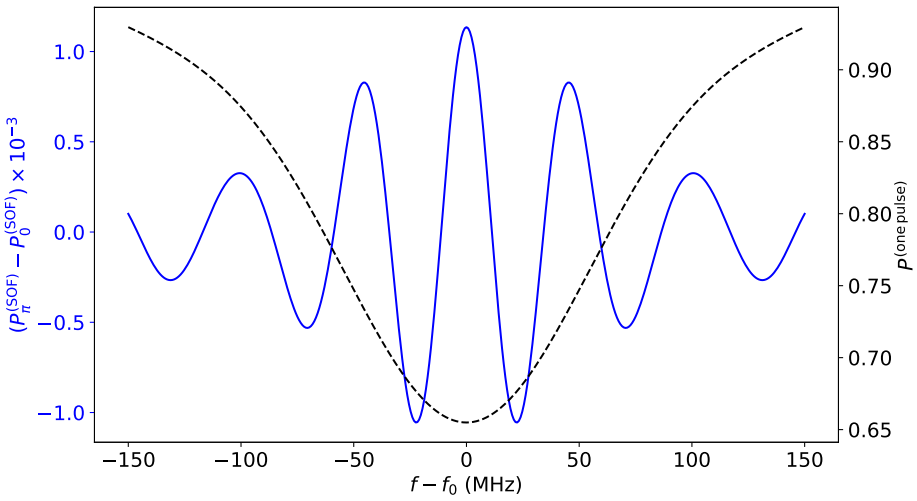

Figure 1.5: Calculated SOF lineshape for two square pulses of the rf electric field for the case of $\tau = 9.7\,\text{ns}$, $T = 16.2\,\text{ns}$, and $E_0 = 14\,\text{V/cm}$. The SOF lineshape is the difference in the $2S$ population obtained with the pulses driven separately in-phase (represented by $P_0^{(\text{SOF})}$) and out-of-phase (represented by $P_\pi^{(\text{SOF})}$). The lineshape obtained with a single field-interaction region (with a duration 2τ and the same field amplitude) is shown in dashed black (and uses the axis labeled in black at the right of the plot).

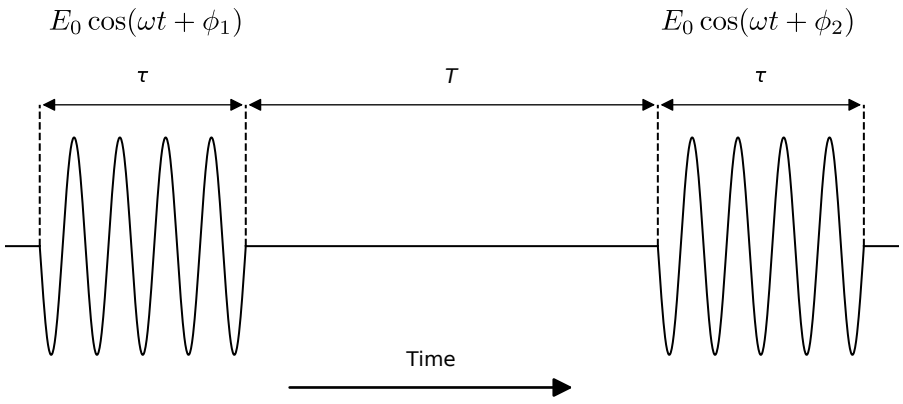

Figure 1.6: SOF pulse sequence. The pulses, spaced by the time interval T, are of equal duration τ.

T between the pulses, as shown in Fig. 1.6. Note that the phases of the electric fields for the two pulses (ϕ_1 and ϕ_2, respectively) can be different. For the SOF method, the probability for the atom to remain in state $|1\rangle$, after exposure to the pulses (for a phase difference $\delta\phi = \phi_2 - \phi_1$) is [26]

$$P_{\delta\phi}^{(\mathrm{SOF})} = e^{-(\gamma_1+\gamma_2)\tau-\gamma_1 T} \times |(\cos\frac{1}{2}\alpha\tau + i\cos\beta\sin\frac{1}{2}\alpha\tau^2) - \\ -e^{\frac{1}{2}(\gamma_1-\gamma_2)T - i(\delta\phi+\Omega T)}\sin^2\beta\sin^2\frac{1}{2}\alpha\tau|^2. \tag{1.19}$$

This expression can be written as

$$P_{\delta\phi}^{(\mathrm{SOF})} = P^{(0)} + A\cos(\theta+\delta\phi), \tag{1.20}$$

with the amplitude of the atomic interference given by

$$A = e^{-\frac{1}{2}(\gamma_1+\gamma_2)(2\tau+T)}|\cos\frac{1}{2}\alpha\tau + i\cos\beta\sin\frac{1}{2}\alpha\tau|^2|\sin\beta\sin\frac{1}{2}\alpha\tau|^2, \tag{1.21}$$

$$\delta\phi = \phi_2 - \phi_1, \tag{1.22}$$

$$\theta = \Omega T + \Gamma(f,\tau,E_0), \tag{1.23}$$

$$\Gamma = 2[\arg(\cos\frac{1}{2}\alpha\tau + i\sin\frac{1}{2}\alpha\tau)^* + \arg(\sin\beta) + \arg(\sin\frac{1}{2}\alpha\tau)], \tag{1.24}$$

and $P^{(0)}$ is the term that is independent of the phase difference between the fields, $\delta\phi$.

The interference term can be extracted by determining the difference of probabilities for the case, when $\delta\phi = \pi$ and $\delta\phi = 0$ radians:

$$P_{\pi}^{(\mathrm{SOF})} - P_{0}^{(\mathrm{SOF})} = 2A\cos(\theta). \tag{1.25}$$

This expression is plotted in blue in Fig. 1.5, and it constitutes the SOF lineshape. The width of the SOF lineshape is smaller than that of the lineshape obtained with a single pulse, and becomes progressively smaller for larger T. On the other hand, the size of the signal is significantly smaller than the single-pulse lineshape.

1.3.2 Frequency-offset separated-oscillatory-fields technique (FOSOF)

The SOF lineshape is realized by changing the phase difference, $\delta\phi$, between 0 and π radians, and determining the change in the probability for the range of frequencies, f, or, equivalently, for the range of detunings, $f - f_0$. If, rather than toggling $\delta\phi$ between 0 and π, $\delta\phi$ is varied continuously (a linear increase in $\delta\phi$ as a function of time), then the probability for an atom to remain in the initial state, $|1\rangle$, oscillates sinusoidally in time.

A linear change in $\delta\phi$ can be achieved by slightly changing the frequency of the rf in one of the pulses, by an amount $\Delta f \ll f_0$, called the offset frequency, as shown in the upper portion of Fig. 1.7, and therefore we refer to this method as frequency-offset separated oscillatory fields (FOSOF). The probability of remaining in state $|1\rangle$ is obtained from the derivation in the previous section (cf. Eqs. 1.12 and 1.23):

$$\begin{aligned} P^{(\mathrm{FOSOF})}_{\Delta\omega t} &= P^{(0)} + A\cos(\theta + \Delta\omega t + \phi_2 - \phi_1) \\ &= P^{(0)} + A\cos\big[(\omega - \omega_0)T + \Gamma(f,\tau,E_0) + \Delta\omega t + \phi_2 - \phi_1\big]. \end{aligned} \tag{1.26}$$

The crucial difference between the SOF technique and the new method of frequency-offset separated oscillatory fields is the following: instead of extracting the magnitude of the interference term for the range of frequencies (which is the basis of the SOF technique) for each rf frequency $f = \omega/(2\pi)$, we determine the phase of the probability oscillation, θ (Eq. 1.23, Fig. 1.7), with respect to the phase difference between the fields, $\delta\phi = \Delta\omega t + \phi_2 - \phi_1$. The phase, θ, can be extracted from the phase difference between the product of the two fields, oscillating at the frequency $\Delta f = \Delta\omega/2\pi$, and the sinusoidally oscillating interference term (cf. the bottom plot of Fig. 1.7). The phase, θ, obtained in such a way, is called the FOSOF phase.

The FOSOF lineshape, which is the FOSOF phase measured for a range of

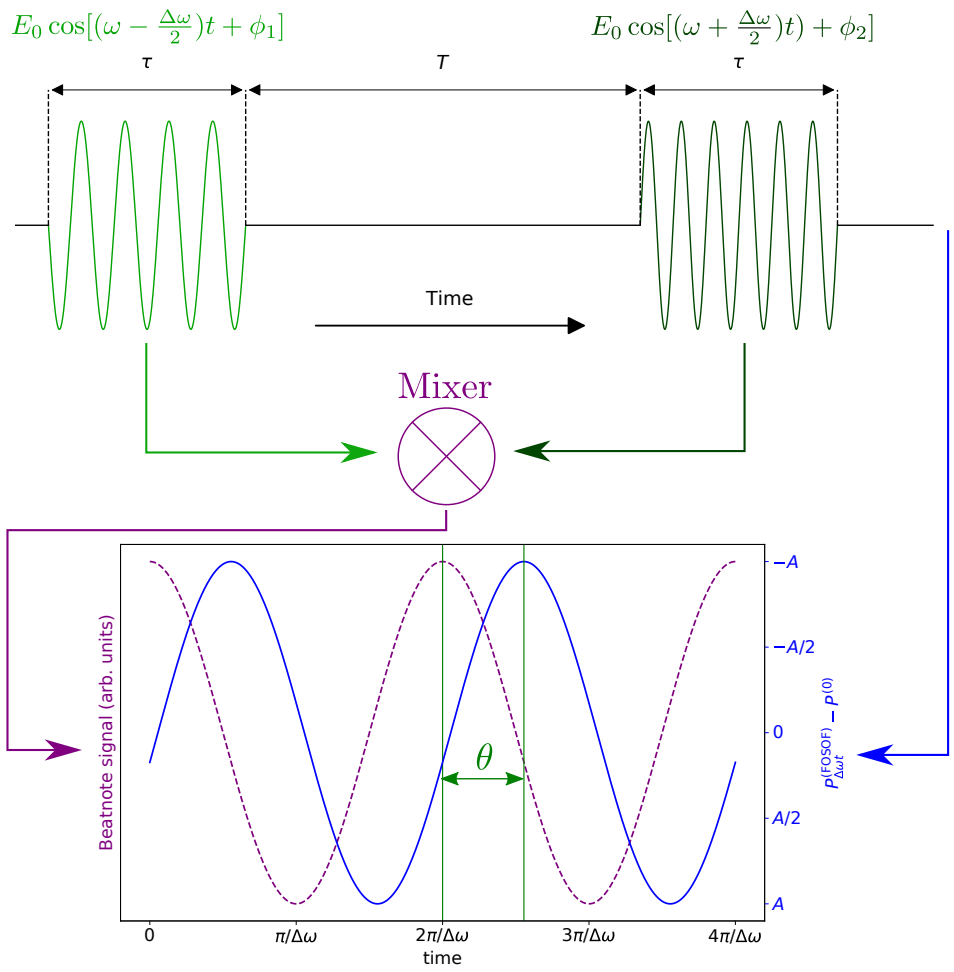

Figure 1.7: Schematic representation of the FOSOF technique. The top of the figure is the diagram of the rf pulses, experienced by a hydrogen atom in the initial state $|1\rangle$. The pulses of rf electric field are separated by the time interval, T, and are of equal duration, τ. Unlike the SOF pulse sequence, the pulses for the FOSOF method are frequency offset from each other by $\Delta f = \Delta\omega/2\pi$. The fields of the two pulses are fed into a mixer that produces the beatnote of frequency Δf (shown as the purple dotted line on the plot), the phase of which is equal to the phase difference $\phi_2 - \phi_1$ between the fields. The probability for an atom to remain in state $|1\rangle$ after the sequences of the pulses, oscillates sinusoidally at frequency Δf (shown as the solid blue curve). The phase difference between the probability oscillation and the beatnote is equal to the FOSOF phase, θ, as indicated with the green arrow.

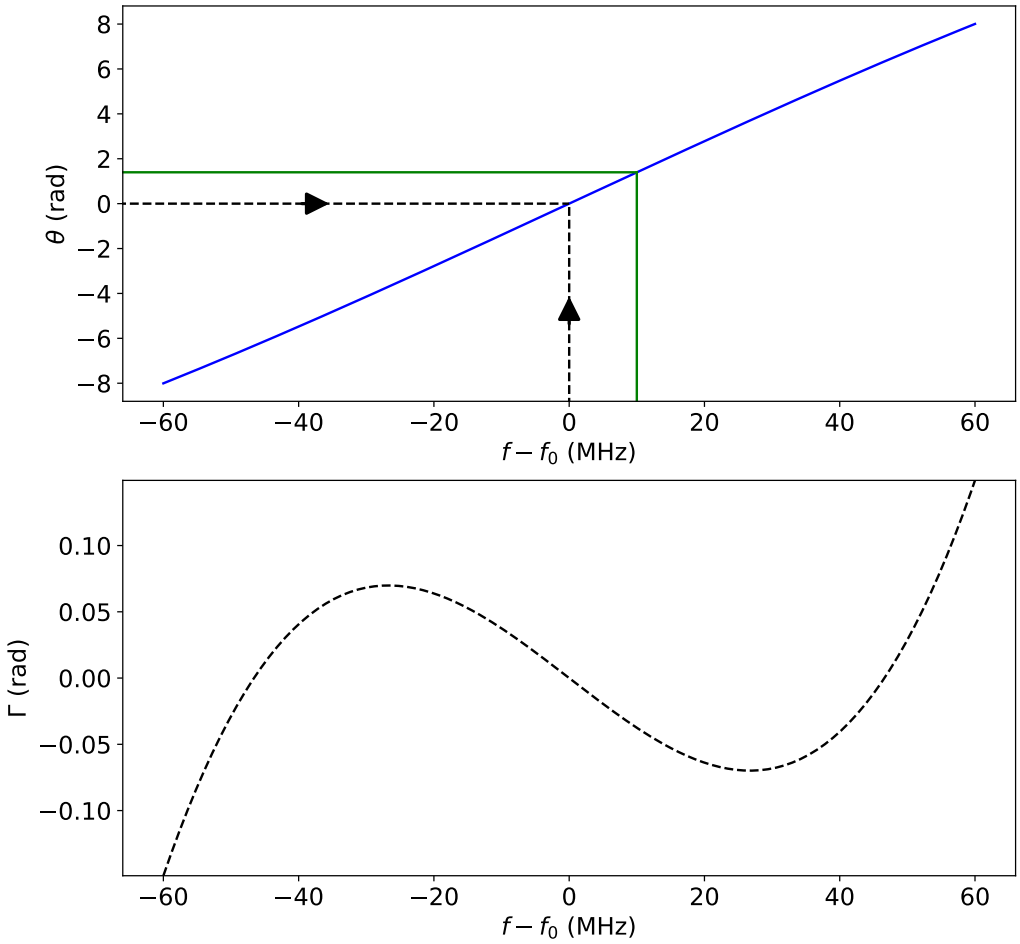

Figure 1.8: FOSOF lineshape for the case of $\tau = 9.7\,\text{ns}$, $T = 16.2\,\text{ns}$, and $E_0 = 14\,\text{V/cm}$ (the same parameters as for the SOF lineshape plotted in Fig. 1.5). The FOSOF phase, θ, is obtained from the procedure described in the text and in Fig. 1.7. The FOSOF lineshape is slightly nonlinear, with an odd (with respect to $f - f_0$) deviation from linearity, as shown at the bottom plot of the figure where the linear component of the lineshape has been subtracted. The nonlinearity is contained in the term $\Gamma(f, \tau, E_0)$ (in Eqs. 1.26 and 1.24). The resonance occurs at the FOSOF phase $\theta = 0$ radians, and the zero-phase-crossing of the fit to a straight line gives the correct resonance frequency, as indicated by the black arrows. Referring to Fig. 1.7, if the beatnote is in phase with the probability for the atom to remain in state $|1\rangle$, then the frequency, $f = \omega/2\pi$ is equal to the resonant frequency, $f_0 = \omega_0/2\pi$. The green lines correspond to the phase θ, indicated in Fig.1.7, for a detuning of $f - f_0 = 10\,\text{MHz}$.

frequency detunings, is plotted in Fig. 1.8. Compared to the SOF lineshape (Fig. 1.5), the FOSOF lineshape is simpler. In particular, the very small term Γ of Eq. 1.24 is an odd function with respect to detuning $f - f_0$. Hence, it is sufficient to fit the FOSOF lineshape to an odd polynomial. Moreover, $\Gamma(f, \tau, E_0)$, plotted at the bottom of Fig. 1.8, is sufficiently linear for the frequency range ($|f - f_0| < 2\,\mathrm{MHz}$) used in this work[6], and therefore the FOSOF lineshape is approximately a line:

$$\theta = 2\pi(f - f_0)T', \tag{1.27}$$

where T' would be T in the limit of zero rf power, but is modified by the linear contribution from $\Gamma(f, \tau, E_0)$. Zero phase ($\theta = 0$) occurs at the resonant frequency f_0:

$$f_{zc} = f_0, \tag{1.28}$$

where f_{zc} is the zero-phase-crossing frequency determined from the fit of the FOSOF lineshape to a line. In Eq, 1.27, the slope of the line is given by

$$S = 2\pi T', \tag{1.29}$$

and it is called the FOSOF slope.

A simplified representation of the experiment, presented in this work, is shown in Fig. 1.9. A monoenergetic beam of hydrogen atoms, all in the state $|1\rangle = |2S_{1/2}, f = 0\rangle$, is sent through two regions of linearly polarized radio-frequency (rf) electric field in the FOSOF configuration. The remaining state-$|1\rangle$ population is measured by a detector.

[6]In the low-power limit the FOSOF lineshape is a line – the simplest lineshape, as shown in Appendix A.

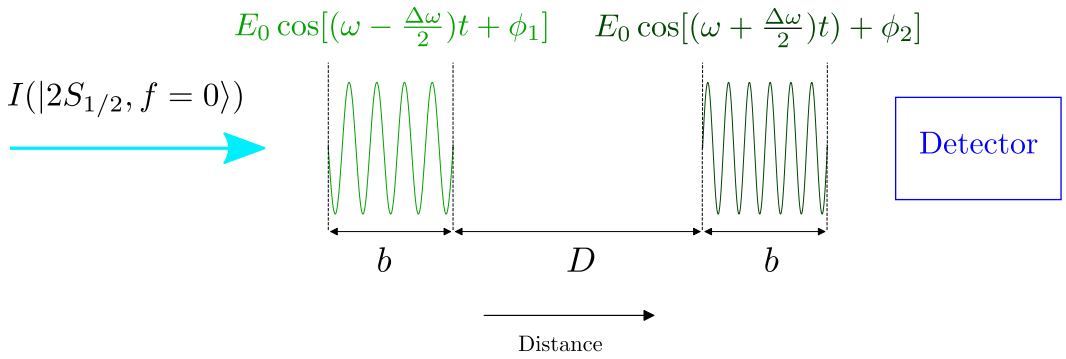

Figure 1.9: Schematic of the experiment. A beam of metastable hydrogen atoms, of current I, in the state $2S_{1/2}, f = 0$, travels through two regions of rf field. The fields are in the FOSOF configuration. The width of each interaction region is b, and the distance between the interaction regions is D. After the fields, the remaining population of the atoms in the $2S_{1/2}, f = 0$ state is detected.

2 Experimental setup

2.1 Overview of the experiment

Figure 2.1 shows a schematic of the experimental setup. A Thonemann-type ion source [28] with inductive coupling produces a high-current (50 µA) collimated beam of protons (as discussed in Sec. 2.2), moving at about 1% of the speed of light (approximately 3 mm/ns). The protons pass through a region containing molecular hydrogen gas, where charge exchange occurs (as discussed in Sec. 2.3) and atomic hydrogen (H) is formed. Of the neutral H formed, about 5% are expected to be in the $2S_{1/2}$ metastable state [29], which has a lifetime of 0.122 s. The vast majority of the remaining 95% of the hydrogen atoms are in the ground state, with only a very small population in $n > 2$ states. A 70-cm-long section of dc electric field is used to deflect the protons and to quench $n > 2$ states (as discussed in Sec. 2.4). Radio-frequency cavities, driven at 1088 and 1147 MHz, positioned after the proton deflector, remove the population in the metastable $f = 1$ hyperfine state by driving it to the $2P_{1/2}$ state (see Figure 2.2 and Sec. 2.5 for details). (The 910-MHz cavity is only used to control the population in the $2S_{1/2}, f = 0$ state for the study of systematic effects, as described in Sec. 3.2.1[7].) The atoms then travel through two standing-wave waveguides, which contain radio-frequency (rf) fields that can be

[7]To clarify, the 910-MHz cavity means the cavity is driven at 910 MHz. Similarly, the 1088-, and 1147-MHz cavities are driven at 1088 and 1147 MHz, respectively.

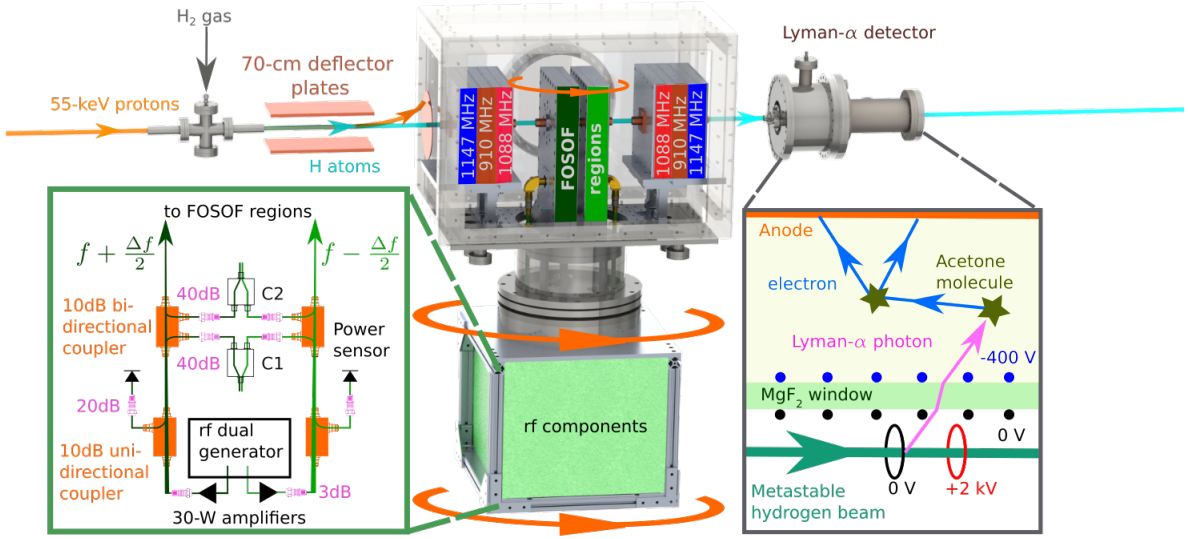

Figure 2.1: The experiment. Protons (shown in orange) with typical energy of 55 keV undergo charge exchange with molecular hydrogen gas. The neutral beam – a mixture of ground, high-n ($n > 2$), and metastable hydrogen atoms (shown in cyan) – travels through a section of dc electric field that quenches the high-n states and deflects the remaining protons. The population in the metastable $2S_{1/2}, f = 1$ state is quenched by two sets of cavities, driven at 1088 and 1147 MHz. The $2S_{1/2}, f = 0$ atoms pass through two coherently-driven radio-frequency waveguides, with frequencies of $f + \frac{\Delta f}{2}$ in one waveguide and $f - \frac{\Delta f}{2}$ in the other waveguide (with the offset frequency $\Delta f \ll f$). In the Lyman-α detector, the surviving population of metastable atoms is quenched via mixing with the fast-decaying $2P_{1/2}$ state, and emitted Lyman-α radiation is detected. The rf system for the FOSOF regions, including the waveguides, is on a large 30-cm-diameter flange, which can be rotated in situ. The figure is adopted from [11].

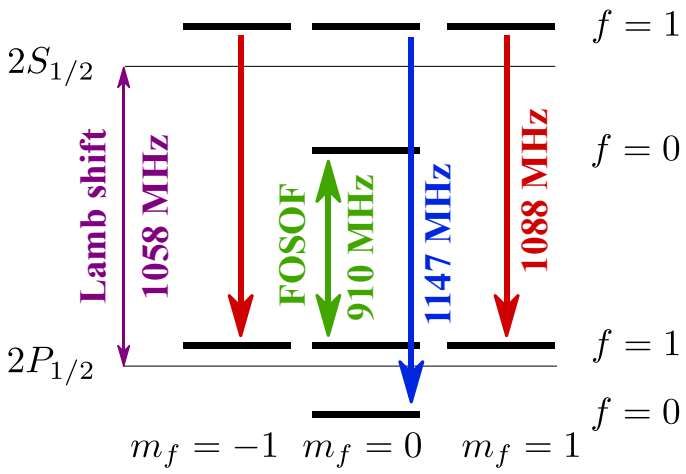

Figure 2.2: $\Delta m_f = 0$ transitions driven in the experiment. The transitions at 1088 and 1147 MHz (shown in red and in blue) are driven to empty the population in the magnetic sublevels of the $2S_{1/2}, f = 1$ states. The main transition is indicated in green, and its frequency is determined in the current measurement using the FOSOF technique.

tuned across the $2S_{1/2}, f = 0 \rightarrow 2P_{1/2}, f = 1$ resonance, where the method of the frequency-offset separated oscillatory fields is performed.

The relative phase between the FOSOF field regions (Fig. 2.1) is continuously varied by having a small (approximately 1 kHz) frequency offset (Δf) between the two rf fields. The beatnote between the fields is formed twice, by combining the rf fields in combiner C1 and in C2 (these are shown as part of the rf system, enclosed in the green box, in Fig. 2.1)[8].

After the FOSOF regions the metastable beam passes through another set of quench cavities, resonant at 1088 and 1147 MHz. These cavities quench small populations in the $2S_{1/2}, f = 1, m_f = \pm 1$ or $2S_{1/2}, f = 1, m_f = 0$ states, most of which result from $n > 2$ states that decay somewhere between the two sets of quench cavities.

[8]Details about the waveguides and the rf system are presented in Sec. 2.6. This section also described the reason for having two combiners at different locations for combining the fields.

Finally, the beam passes through a Lyman-α detector (described in Sec. 2.7) that outputs a voltage proportional to the number of metastable atoms that make it to the detector. This signal includes a component oscillating at the offset frequency (Δf). The phase difference between this component and the beatnote formed by combining the rf fields in the FOSOF regions leads to the FOSOF phase θ [9].

2.2 Proton beam

An important part of the experiment is the production of protons and the maintenance of a stable proton beam current, since the stability is essential for obtaining a stable detection signal at the Lyman-α detector.

A schematic of the proton source is shown in Fig. 2.3. The protons are extracted from a Pyrex tube filled with hydrogen gas with an rf-driven plasma discharge. The protons, along with other heavier positively charged species, are accelerated and focused. The magnetic field of the deflecting electromagnet is adjusted to allow only protons to pass to the rest of the experiment.

The proton source floats at a high voltage V_{HV} (supplied by a Heinzinger PNChp power supply), and the electronics for the production of the 500-watt, approximately 100-MHz rf field used to ignite and maintain the plasma, the power supplies for controlling the probe, the solenoid, and most of the ion optics are located inside a metal enclosure maintained at V_{HV}. An isolation transformer is used to provide 60-Hz AC-line voltage as the power source for the power supplies. The proton source is operated by setting the voltages applied to the probe electrode (in the range of 0-10 kV with respect to V_{HV}), the ion optics (in the

[9] The phases of the beatnotes, produced by each of the combiners, are not equivalent to the phase difference, $\delta\phi$, between the fields in the FOSOF regions. Section 2.8 discusses this important problem.

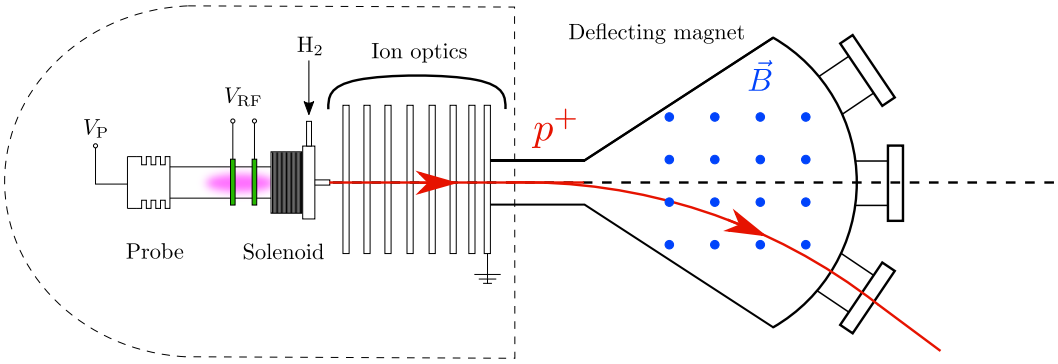

Figure 2.3: Schematic diagram of the proton source (top view, not to scale). The metal shield (dashed line) and all of the components inside are floating at $V_{HV} \approx 50\,\text{kV}$. The voltages shown inside are with respect to V_{HV}. The plasma (shown in purple) is from molecular hydrogen, which is dissociated and ionized via application of a high-power rf fields, which are applied via the copper rings, shown in green. An axial magnetic field of the solenoid confines the plasma. The protons are repelled by the probe electrode, and travel through the set of einzel lenses, accelerating rings, and the quadrupole doublet – all collectively denoted as "ion optics". The deflecting magnet acts as a velocity filter used to select only protons. Before the magnet there are two mutually-orthogonal square coils (not shown) for left-right and up-down beam steering. Right after the plasma-discharge tube there is a metallic ion extractor (its nozzle is visible right after the solenoid) that is largely responsible for determining the initial shape and divergence of the beam.

range of 0-30 kV relative to V_{HV}), and the rf-field-generating circuit, as well as the electric currents flowing in the solenoid and the deflecting magnet, and, lastly, the flow of hydrogen gas into the discharge tube.

The settings of the proton source are adjusted until a sufficiently large proton current is created and the frequency spectrum of the Lyman-α-detector signal has the minimum noise around the FOSOF offset frequency[10]: generally, no subsequent tweaking of the proton source settings are necessary for several days.

[10]The offset frequency (of either 625 or 800 Hz) is chosen to avoid the AC-line harmonics, that were often the strongest frequency components in the Lyman-α-detector signal. These harmonics are probably due to insufficient low-pass filtering of the AC-DC power supplies used inside the proton source enclosure.

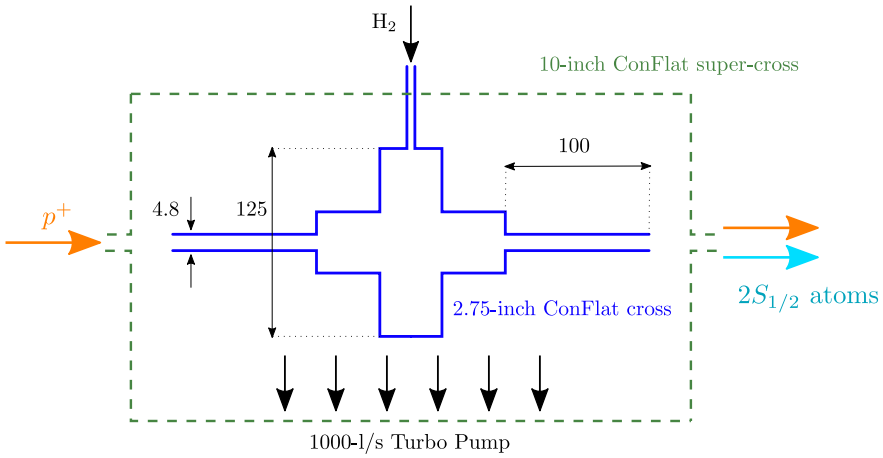

Figure 2.4: Diagram of the charge-exchange apparatus. The figure is not to scale. The charge-exchange cell is a 2.75-inch ConFlat cross with welded 10-cm-long pumping restrictions with an inner diameter of 4.8 mm, fixed inside of a 10-inch ConFlat 6-way cross which has two shorter pumping restrictions of the same diameter. The pressure inside the cell is controlled with a mass-flow controller. A high-pumping-speed turbo pump prevents the increase of pressure outside the charge-exchange apparatus. Dimensions are in millimeters.

The total kinetic energy of the protons after the deflecting magnet is approximately

$$T_p \approx e(V_{\mathrm{HV}} + V_{\mathrm{P}}), \tag{2.1}$$

where V_{P} is the probe voltage, and V_{HV} is called the nominal accelerating voltage, with $V_{\mathrm{HV}} > V_{\mathrm{P}}$. For most of the experiment the nominal accelerating voltage is set to $V_{\mathrm{HV}} = 49.86\,\mathrm{kV}$. Two other values are used: 22.17 and 16.27 kV. Note that V_{HV} is adjusted only when we want to deliberately change the beam speed for the studies of the systematic effects (as described in section 3.1).

2.3 Charge exchange

The charge-exchange cell is depicted in Fig. 2.4. It is described in detail in Ref. [29]. At about 50 keV of kinetic energy, a proton that captures an electron from molecular hydrogen gas has about a 5% probability to form a hydrogen atom in the metastable state [29]. The pressure in the cell is adjusted to maximize the number of metastable atoms produced, as measured by the Lyman-α-detector signal (see Fig. 2.1). Referring to Fig. 2.4, the pressure inside the 10-inch ConFlat 6-way cross, but outside of the 2.75-inch ConFlat cross (the charge-exchange cell) is maintained at 1.6 μTorr.

As will be discussed in Sec. 2.5, we have experimental evidence for the presence of small populations in the high-n states in our metastable beam, which indicates that the charge-exchange process may have a non-negligible probability for forming hydrogen atoms in $n > 2$ states. The effect of these states on the resonant frequency obtained with the FOSOF technique, is discussed in Sec. 3.2.

2.4 Proton deflector

The space charge due to a proton beam overlapped with the neutral hydrogen beam creates an electric field that shifts the energy difference between the $2S_{1/2}, f = 0$ and $2P_{1/2}, f = 1$ states. Assuming that the beam has a cylindrical shape and has a uniform density, the rms electric field that the metastable atoms would experience is

$$E_{\mathrm{rms}} = \frac{I_{\mathrm{p}}}{2\pi v \epsilon_0 r}, \tag{2.2}$$

where I_{p} is the proton current, v is the beam speed, r is the beam radius, and ϵ_0 is the permittivity of free space. For the protons with a kinetic energy of 50 keV, and a beam current of 50 µA, with a diameter of 4 mm, the rms electric field would be

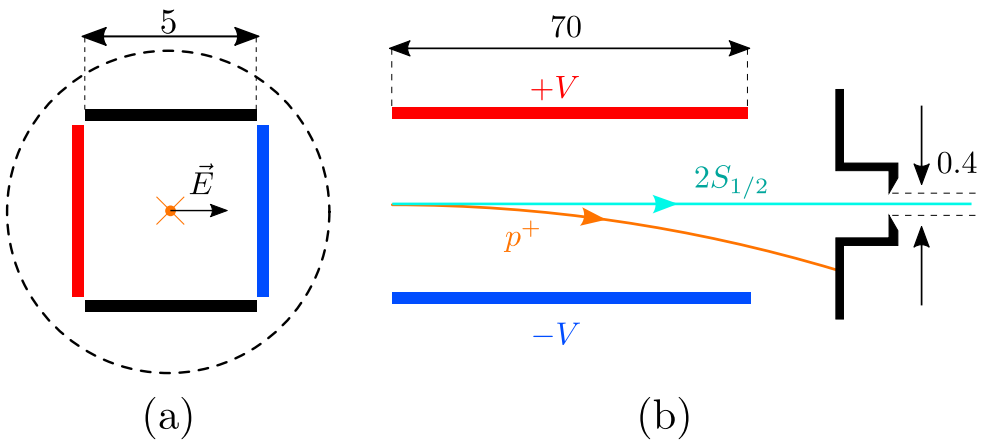

Figure 2.5: The proton deflector (not to scale). All dimensions are in centimeters. Four copper plates are symmetrically placed inside a 6-inch ConFlat nipple section. The plates in black are grounded. The drawing on the left (a) is a frontal cross-section of the deflector, and the drawing on the right (b) is the side view (with the grounded plates not shown). The protons are deflected onto the copper cylindrical cup, and surviving metastable atoms pass through a 4-mm round aperture in this cup.

about 1.5 V/cm. The DC Stark shift of the $2S_{1/2}, f = 0$ to $2P_{1/2}, f = 1$ interval is quadratic in electric field, and is equal to[11]:

$$\Delta f_{\rm DC} = 9.9\,{\rm kHz}/({\rm V/cm})^2 E_{\rm eff}^2. \tag{2.3}$$

With the rms electric field of 1.5 V/cm, the frequency shift would be about 22 kHz.

Because of the magnitude of the possible DC-Stark shift from space charge (and because the protons could charge up surfaces near the beam), it is desirable to deflect the protons after the charge-exchange cell. This deflection is achieved by applying an electric field, transverse to the beam axis, in the region right after the charge-exchange cell (as shown in Fig. 2.1). The proton deflector is shown

[11]Taking into account the repulsion of the $2S_{1/2}$ state by the $2P_{1/2}$ and $2P_{3/2}$ states, and the repulsion of the $2P_{1/2}$ state by the $2S_{1/2}$ state. Also, the Stark shift depends on the direction of the electric field. For simplicity it is assumed that the electric field is parallel to the rf electric field in the FOSOF regions.

schematically in Fig. 2.5. The potential difference between the plates (shown in red and blue in Fig. 2.5) is increased until the maximum current on the Faraday cup, used to block the protons, is observed to ensure that all of the protons are deflected[12]. For the nominal accelerating voltage, V_{HV}, set to 16.27, 22.17, and 49.86 kV, the maximal current on the Faraday cup is observed when the potential difference between the plates is set to 37.7, 82.5, and 120.0 V, respectively. The electric field at the position of the beam due to these potential differences is 6.3, 13.8, and 20.0 V/cm, respectively.

The proton deflector was designed with a second purpose in mind: to maximally reduce the populations in $n > 2$ states. The method for quenching $n > 2$ states is explained in Ref. [30]. In short, when a hydrogen atom in an $n > 2$ state is exposed to the electric field of the proton deflector, the lifetime of the longer-lived states within the manifold are reduced by mixing with the shorter-lived states. Therefore, in the electric field of the proton deflector, the unwanted populations in $n > 2$ states are reduced. Unfortunately, the deflector field reduces the population in the $2S_{1/2}$ state as well. The reduction of the population in the $2S_{1/2}$ state can be minimized by increasing the length of the proton deflector and reducing the magnitude of its electric field. For our experiment the length of the deflector was chosen to be 70 cm. It was calculated that after the beam of atoms passes through the resulting 20-V/cm field in the proton deflector, the populations of states with $2 \leq n \leq 5$ are reduced by factors of 1.3 ($2S$ state), 24 ($3S$ state), 450 ($4S$ state), and at least by a factor of 1.3 ($5S$ state).

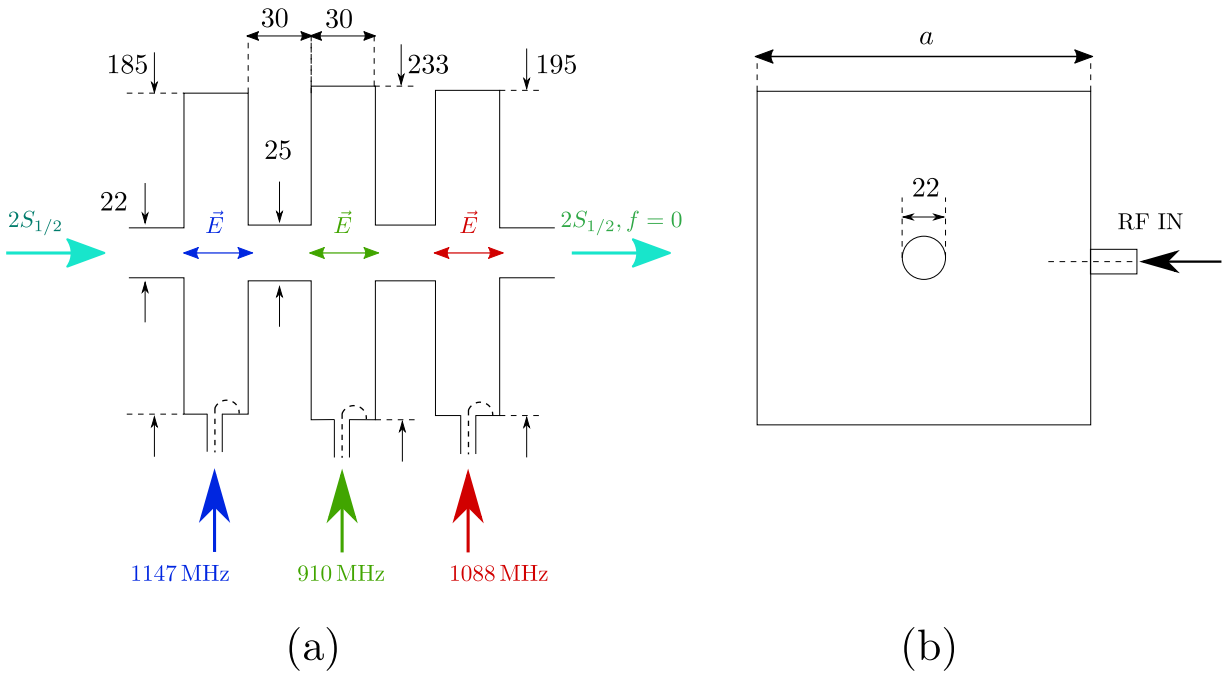

Figure 2.6: Pre-quench rf-cavity stack. The dimensions indicated are in millimeters. The cavities are machined out of aluminum. (a) shows the top view, and (b) is the frontal view. For each cavity the TE_{101} mode is excited with a small loop of wire which is a continuation of the inner conductor of the coaxial cable that supplies rf waves to the cavity, shown by the dashed lines at the bottom of panel (a). An electric field parallel to the beam axis (indicated with the cyan arrow) drives $\Delta m = 0$ transitions. The middle cavity is used to control the population in the $2S_{1/2}, f = 0$ state. The cavities are separated from each other by 30-mm-long 25-mm-diameter cylindrical aluminum tubes. These tubes suppress the leakage of the rf fields between the cavities. The rf powers in the cavities are set to drive π pulses for the appropriate $\Delta m_f = 0$ transitions shown in Fig. 2.2. When no rf power is supplied to the 910-MHz cavity, only atoms in the $2S_{1/2}, f = 0$ state survive the passage through the cavities. Dimension a in panel (b) is 185, 233 and 195 mm for the 910-, 1088-, and 1147-MHz cavities, respectively.

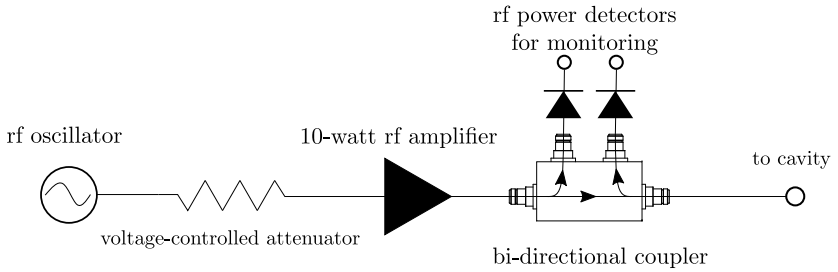

Figure 2.7: Simplified diagram of an rf system for a quench cavity. The power output of an rf oscillator (SynthUSBII) is controlled by adjusting the voltage applied to a voltage-controlled attenuator. The rf oscillator frequency is set to one of 910, 1088, or 1147 MHz.

2.5 Hyperfine-state selection

In the charge-exchange cell, hydrogen atoms in the $2S_{1/2}, f = 0$ and $2S_{1/2}, f = 1$ states are formed. Population in the $2S_{1/2}, f = 1$ state could cause a systematic shift in the resonant frequency of the $2S_{1/2}, f = 0 \rightarrow 2P_{1/2}, f = 1, m_f = 0$ transition determined using the FOSOF technique (as discussed further in Sec. 3.6). This shift could result from $\Delta m_f = 0$ transitions between the $2S_{1/2}, f = 1$ and $2P_{1/2}$ states that are off-resonantly driven (the transition frequencies are shown in Fig. 2.2.). Therefore, it is important to minimize the population in the $2S_{1/2}, f = 1$ state. To accomplish this, two pre-quench rf cavities driven at 1088 and 1147 MHz are positioned before the FOSOF regions, as shown in Figs. 2.1 and 2.6.

A set of post-quench cavities driven at 1088 and 1147 MHz is located after the FOSOF regions (see Fig. 2.1), and these cavities quench any small population of $2S_{1/2}, f = 1$ atoms that are created by radiative decay from high-n states. 910-MHz cavities are included in both the pre- and post-quench regions to allow for quenching $2S_{1/2}, f = 0$ atoms for systematic tests.

The rf systems for the quench cavities are identical, and are shown in Fig. 2.7.

[12]The Faraday cup is represented in Fig. 2.1 as the orange disk between the proton deflector and the first set of the quench cavities.

Radio-frequency powers supplied to the cavities are controlled by a set of voltage-controlled rf attenuators. For each of the cavities, the voltage supplied to the respective voltage-controlled rf attenuator is adjusted until the Lyman-α-detector signal is minimized, as shown in Fig. 2.8. The minimum Lyman-α-detector signal is an indicator that the rf powers supplied to the 910-, 1088-, and 1147-MHz cavities are set to drive a π pulse for the $2S_{1/2}f = 0 \rightarrow 2P_{1/2}, f = 1, m_f = 0$, $2S_{1/2}, f = 1, m_f = \pm 1 \rightarrow 2P_{1/2}, f = 1, m_f = \pm 1$, and $2S_{1/2}, f = 1, m_f = 0 \rightarrow 2P_{1/2}, f = 0$ transitions, respectively (shown in Fig. 2.2).

The optimal rf power that minimizes the Lyman-α-detector signal for, for example, the pre-quench 910-MHz cavity is realized in the following way[13]. Firstly, the power input for the post-quench cavity, driven at the same frequency of 910 MHz, is set to zero. For the other four cavities (the 1088- and 1147-MHz cavities), the powers are set to our best estimates of the rf powers required to drive their respective π pulses. The rf power supplied to the pre-quench 910-MHz cavity is varied, and changes in the Lyman-α-detector signal are measured, as shown in blue in Fig. 2.8. The obtained data is called a quench curve, from which an optimal rf power that minimizes the Lyman-α-detector signal is determined (as further described in Sec. 3.6.2). This optimal power is then used as the best estimate of the rf power required to drive a π pulse for the $2S_{1/2}f = 0 \rightarrow 2P_{1/2}f = 1, m_f = 0$ transition in the pre-quench 910-MHz cavity. A similar procedure is used to determine the optimal power for each of the pre-quench cavities. The procedure for determining the optimal power for the post-quench regions is also similar, but in this case, the pre-quench cavity at the same frequency is set to zero power.

This procedure is repeated again for all of the six cavities, until each of the

[13]The pre- and post-910-MHz cavities are not used for quenching of the $2S_{1/2}, f = 1$ state. However, they are used for studies of systematic effects, as described in Sec. 3.2.

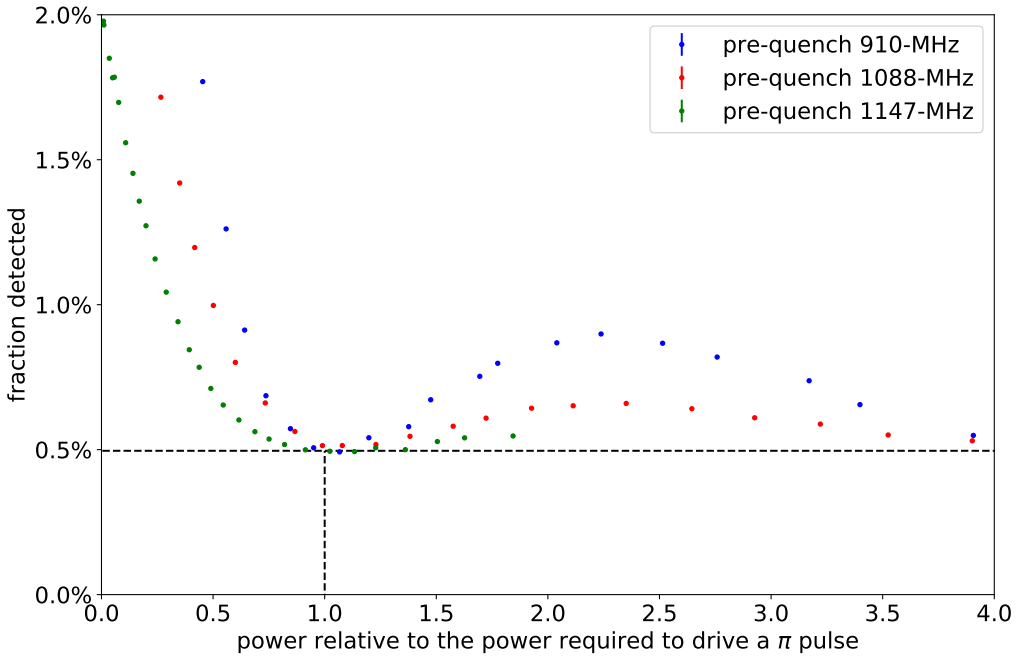

Figure 2.8: Quench curves for the pre-quench cavities. The y axis is the signal from the Lyman-α detector relative to the Lyman-α-detector signal when no rf power is supplied to the quench cavities. The x-axis is the measured rf power supplied to the quench cavities, relative to the power required to drive π pulse. The rf power is measured with rf power detectors attached to bi-directional couplers (shown in Fig. 2.7).

optimal powers converge. The quench curves obtained for the pre-quench cavities, after the optimal set of the rf powers was determined, is shown in Fig. 2.8.

The quench curves shown in Fig. 2.8 indicate that at optimal rf powers the surviving population is not zero, but is about 0.5% of the total $2S_{1/2}$ population. When the pre- and post-quench 910 MHz cavities are disabled, then only 6.8% of the $2S_{1/2}$ population survives[14], and therefore the 1088- and 1147-MHz cavities reduce the $2S_{1/2}, f = 0$ population by 73% (since one would expect to have 25% of

[14]If only the pre-quench 1088- and 1147-MHz cavities or post-quench 1088 and 1147-MHz cavities are set to π pulses and the rest of the cavities is de-energized, then about 26% of the $2S_{1/2}, f = 0$ population survives.

the total $2S_{1/2}$ population to be in the $2S_{1/2}, f = 0$ state before entering the quench cavities). The offset is 7.3% of the size of this surviving $2S_{1/2}, f = 0$ population. The quench curves in Fig. 2.8 are acquired with a higher than typical pressure in the experiment region (where the FOSOF regions and the quench cavities are located). At lower pressures the offset is lower – typically the offset is about 3% of the surviving $2S_{1/2}, f = 0$ atoms. This offset is very likely due to the presence of high-n states in the beam. The offset and its effect on the resonant frequency is discussed in more detail in Sec. 3.2.

2.6 FOSOF regions and radio-frequency system

The FOSOF regions are shown in Fig. 2.9. The FOSOF regions are constructed using two radio-frequency waveguides. The waveguides have an electrical short on one end. The design allows more than 99% of power to be coupled into the FOSOF regions over the 900-980-MHz range. The tubes through which the atomic beam enters and exits the waveguides complicates the profile of the radio-frequency fields, and these electromagnetic fields are calculated in the EMPIRE software package[15]. The details of the design of the waveguides are given in Ref. [31]. Only a single TE_{10} mode is excited, and this mode has an electric field which is polarized along the beam axis. However, off-axis, the tubes allow for small perpendicular components of the field.

The rf systems for the two FOSOF waveguides are symmetric (that is, the rf system for one of the waveguides is the mirror image of the rf system for the other waveguide), as shown in Figs. 2.1 and 2.9. The rf generator (Aeroflex IFR2026B dual generator) for the rf system outputs two separate rf signals, frequency offset from each other by Δf. The rf signals are routed through the left and right arms

[15]This software was used in Ref.[9]

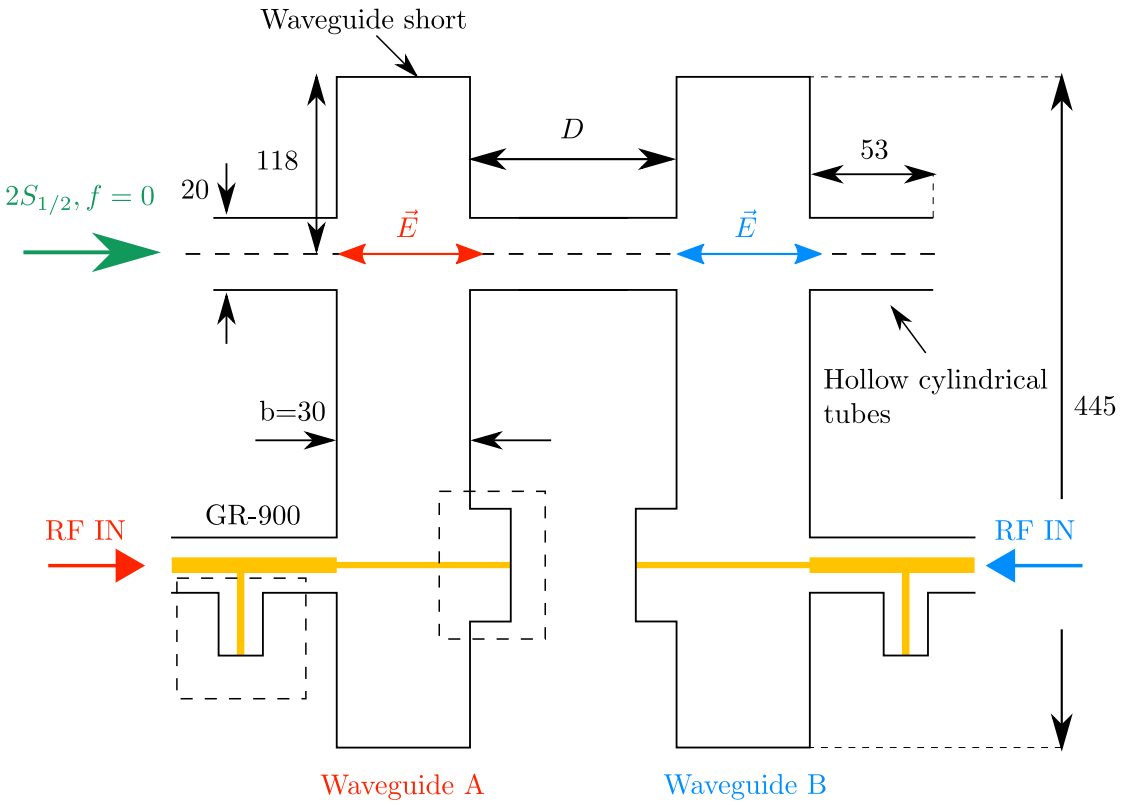

Figure 2.9: Radio-frequency waveguides used in our experiment. The waveguides are machined out of aluminum. The figure is not to scale. The dimensions are shown in millimeters. The beam axis is indicated by a long dashed line, where an antinode of the electric field is located. The separation between the waveguides is denoted by D, which can be varied. Two cylindrical stubs (within dashed rectangular boxes), ensure an efficient coupling of the rf power from the GR-900 coaxial cable into the waveguide. The inner conductor of the coaxial cable is shown in yellow. The width of the rectangular waveguides (the dimension into the page) is 23.0 cm. The inner diameter of the cylindrical tubes at the ends of and in between the waveguides is chosen to suppress the cross-talk between the waveguides and the leakage of radiation from the waveguides.

of the rf system (green box in Fig. 2.1), respectively. The accuracy of the internal reference clock of the rf generator is sufficient for the measurement accuracy of the current experiment, as was verified by both a rubidium clock and a GPS clock. Power sensors (KRYTAR 109B Schottky detectors) monitor the rf power after the rf amplifiers (Mini-circuit ZHL-30W-252X-S+). Power readings from these power detectors are recorded with a Keithley 2701 multimeter. All of the rf components after the 3-dB attenuators (see green box in Fig. 2.1) are inside of a temperature-stabilized metal enclosure.

Power combiners C1 and C2 (Mini-circuits ZAPD-2-21-3W-N+) combine rf from the two arms of the rf system. In particular, combiner C1 combines samples of the rf traveling into the waveguides, and combiner C2 combines samples of the rf returning from the waveguides. Bi-directional couplers (see Fig. 2.1) (Mini-circuits ZGBDC10-362HP+) are used to obtain the samples for C1 and C2. The beatnote (with a frequency of Δf) is extracted using logarithmic rf-power detectors (Mini-Circuits ZX47-55LN+, not shown on the diagram), connected directly to the output of C1 and C2. The phase difference between the outputs of these two power detectors is a critically-important indicator of the path-length stability of the rf system, as discussed in Sec. 3.8.

The two combiners provide a path for a tiny fraction of the rf power from one rf system to leak into the other rf system. An example of such a path through combiner C2 is shown (in blue) in Fig. 2.10. To improve the isolation between the two rf systems, 40-dB attenuators are placed between the bi-directional couplers and the combiners. Taking into account a 10-dB coupling of the bi-directional couplers, and a 20-dB isolation of the power combiners, the isolation between the rf systems for the paths though the combiners is better than 120 dB. Another path for the rf from one system to leak into the other rf system is though a coupling

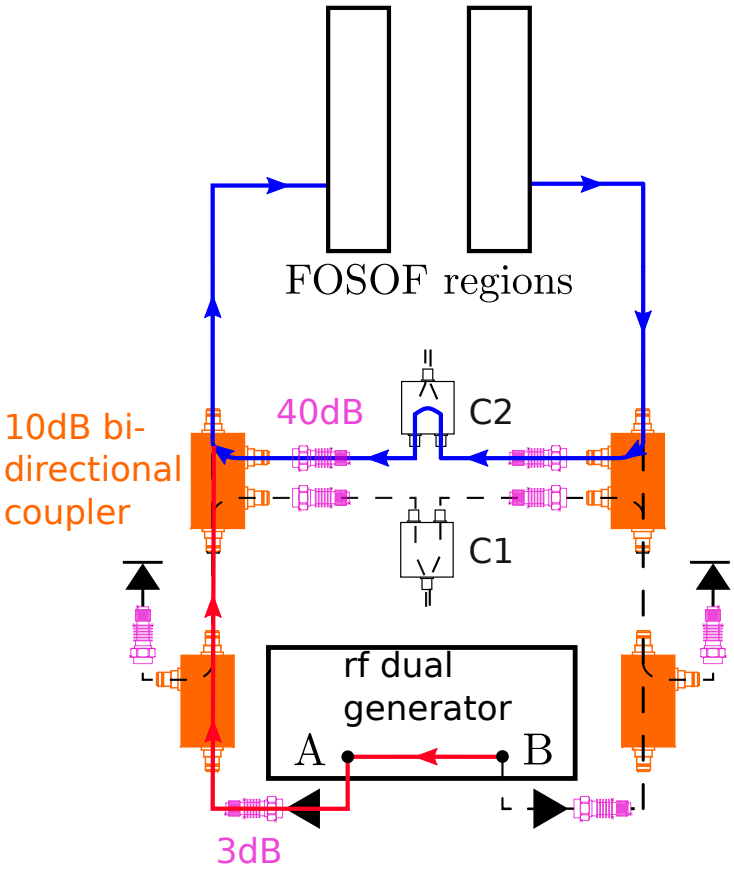

Figure 2.10: Coupling between rf systems for the FOSOF regions. The rf systems are identical to the ones shown in Fig. 2.1 (enclosed in the green dashed box), and the interconnections between the rf components are shown with dashed lines. A path for the rf signal to leak from one rf system to another (shown in blue) is through combiner C2: an rf signal returning from one of the FOSOF regions (an example of the leakage of the rf from the right rf system into the left rf system is shown) enters a bi-directional coupler, and a small fraction of the signal (attenuated by a total of 50 dB) enters combiner C2. The two inputs of the combiner are not perfectly isolated from each other – about 1% of the rf from one input is coupled into the other input. The rf coupled into the other rf system is attenuated by another 50 dB and travels toward the FOSOF waveguide for this rf system. Therefore, about -120 dB of the rf from one rf system is coupled into the other. Another rf-leakage path is through the two outputs of the rf generator (shown in red). The isolation between the outputs is measured to be better than 100 dB.

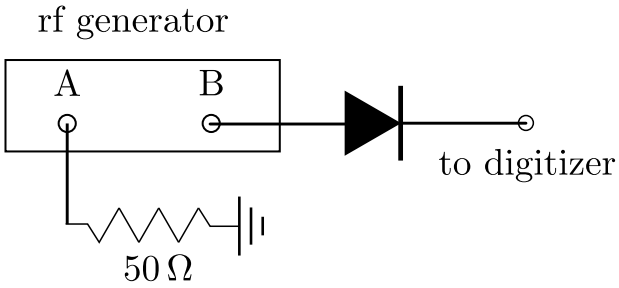

Figure 2.11: Setup to measure the isolation between the outputs of the rf generator. Output A is terminated with a 50 Ω terminator. An rf power detector is connected to output B. The output of the power detected is connected to a digitizer. The rf generator outputs rf powers P_A and P_B with frequencies f_A and f_B from outputs A and B, respectively. The two rf frequencies are offset from each other by less than 1 kHz.

between the two rf outputs of the rf generator, as shown in red in Fig. 2.10.

The isolation between the outputs of the rf generator is measured with the setup shown in Fig. 2.11. A 50 Ω terminator and an rf power detector are attached to outputs A and B of the rf generator, respectively. Two outputs A and B are set to output rf powers P_A and P_B with frequencies f_A and f_B, respectively, offset from each other by less than 1 kHz. The power in the rf that leaks from output A to output B, $P_{A\to B}$, is determined from the amplitude of the beatnote observed on the rf power detector. The isolation is defined as $P_A/P_{A\to B}$, and it is measured to be better than 100 dB.

2.7 Lyman-α detector

The detector of metastable atoms is shown schematically in Figs. 2.1 and 2.12. A large potential difference of 2 kV between two metal rings with a diameter of 2 cm, separated by 2.6 cm, mixes the $2S$ and $2P$ states. The mixture has a decay rate (to the ground state via a Lyman-α photon) of approximately $3 \times 10^8\,\mathrm{s}^{-1}$ or approximately half of the spontaneous transition rate of the $2P$ state to the ground

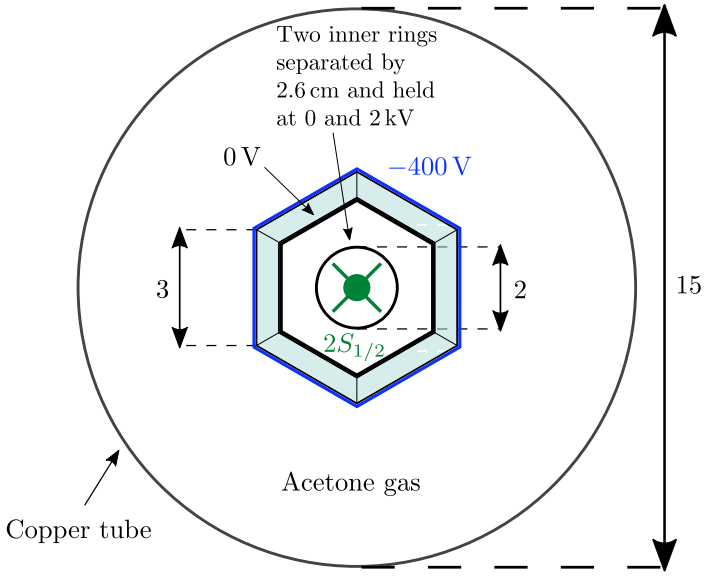

Figure 2.12: Simplified frontal view of the Lyman-α detector. The dimensions are shown in centimeters. In this drawing, atoms in the $2S_{1/2}$ state travel into the page (green). In pale blue is a 9-cm-long hexagonal tube comprised of six separate precision-cut MgF_2 wedges glued together with a Henkel Loctite STYCAST 2850FT Black epoxy. Close to the inner and outer surfaces of the hexagonal tube there are two meshes. The outer mesh is held at a potential of −400 V (shown in blue), and the inner mesh (shown in black) is grounded to shield the atoms from this negative potential. Two thin metal rings of a diameter of 2 cm (shown in black) are centered inside the hexagonal tube. Only the first ring is visible and the other ring is 2.6 cm behind the first ring. The potential difference between the rings is 2 kV. The atoms in the $2S_{1/2}$ state are quenched between the rings causing them to emit 121-nm ultraviolet photons. About 40% of these photons pass through the MgF_2 tube and ionize an acetone molecule. The photoelectrons are accelerated towards a copper tube that surrounds the hexagonal tube, and in the process they collide with more acetone molecules. Amplified electron current is collected by the copper tube, which acts as an anode.

state. Emitted Lyman-α photons, with a wavelength of 121.6 nm, pass through a magnesium-fluoride window[16] and ionize acetone gas that acts as a gain medium[17].

The produced photoelectrons are accelerated away from the window by a repelling wire mesh (at a negative potential) that is wrapped around the magnesium-fluoride window. The photoelectrons collide with other acetone molecules, liberating further electrons. The electron current is detected on the outer copper tube of Fig. 2.12, which acts as a Faraday cup and is connected to a low-noise transimpedance amplifier (FEMTO DLPCA-200).

The gain of the detector depends on the pressure of the acetone gas, which is controlled by a mass-flow controller[18], and on the repelling voltage. Care is taken not to exceed the breakdown voltage of the acetone gas.

2.8 Phase offsets in the FOSOF signal

To determine the FOSOF phase for an rf frequency f, the phase difference between the electric fields in the waveguides has to be known (as was discussed in Sec. 1.3.2). The beatnotes from combiners C1 and C2 (in Fig. 2.1) both have a frequency equal to the offset frequency Δf, and, in the ideal case, each would give a phase that directly reflects the phase difference in the rf fields in the two FOSOF regions: $\phi_{\text{beat}} = \phi_2 - \phi_1$. However, due to filtering effects, delays, unmatched electrical lengths, and imperfections in the combiner systems the beat-signal phase may give a phase offset $\phi_{\text{beat}} = \phi_2 - \phi_1 + \delta\phi_{\text{beat}}$. This phase offset, $\delta\phi_{\text{beat}}$, could be rf-

[16]One of a few available materials sufficiently transparent in the vacuum ultraviolet region.

[17]We decided not to use carbon disulphide gas, that has five times larger photoionization efficiency than acetone gas [32], due to its toxicity.

[18]There is a constant flow of the acetone gas during the operation of the Lyman-α detector. The gas is slowly pumped out with an oil free pump (Agilent SH-110 Dry Scroll Vacuum Pump) through a small aperture.

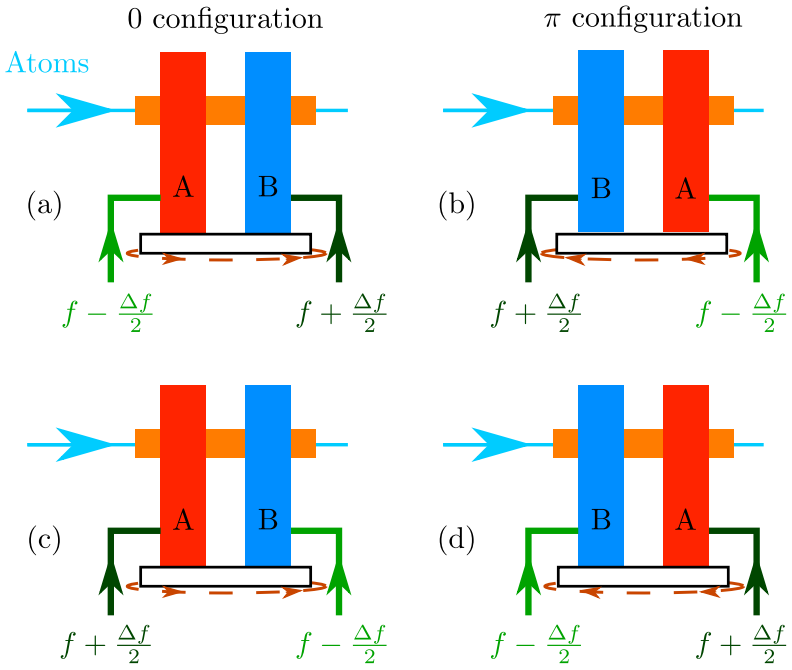

Figure 2.13: Experiment configurations. The atoms travel from left to right, and waveguides A and B are placed on a rotary stage. In (a) and (b) (and similarly in (c) and (d)) the waveguides are reversed (using the rotary stage which rotates the entire rf system – including all components in and outside of vacuum), but the applied rf frequencies, $f + \frac{\Delta f}{2}$ and $f - \frac{\Delta f}{2}$, are unchanged. Configurations in (a) and (c), or (b) and (d) show waveguides in the same orientation, however the frequencies are applied to the opposite waveguides.

frequency-dependent, and could be different for C1 and C2.

The Lyman-α-detector signal has a component oscillating at the offset frequency Δf. Ideally, the phase of this component is equal to the sum of the FOSOF phase and the phase difference in the rf fields in the two FOSOF regions: $\phi_{\text{det}} = \theta + \phi_2 - \phi_1$. However, the Lyman-$\alpha$ detector has a limited bandwidth of about 2 kHz[19], which depends on the detector gain, and also on the gain of the

[19]Determined experimentally by AM-modulating the power in one of the waveguides and observing the phase shift between the beatnote produced by combiner C1 and the Lyman-α-detector signal oscillating at the modulation frequency.

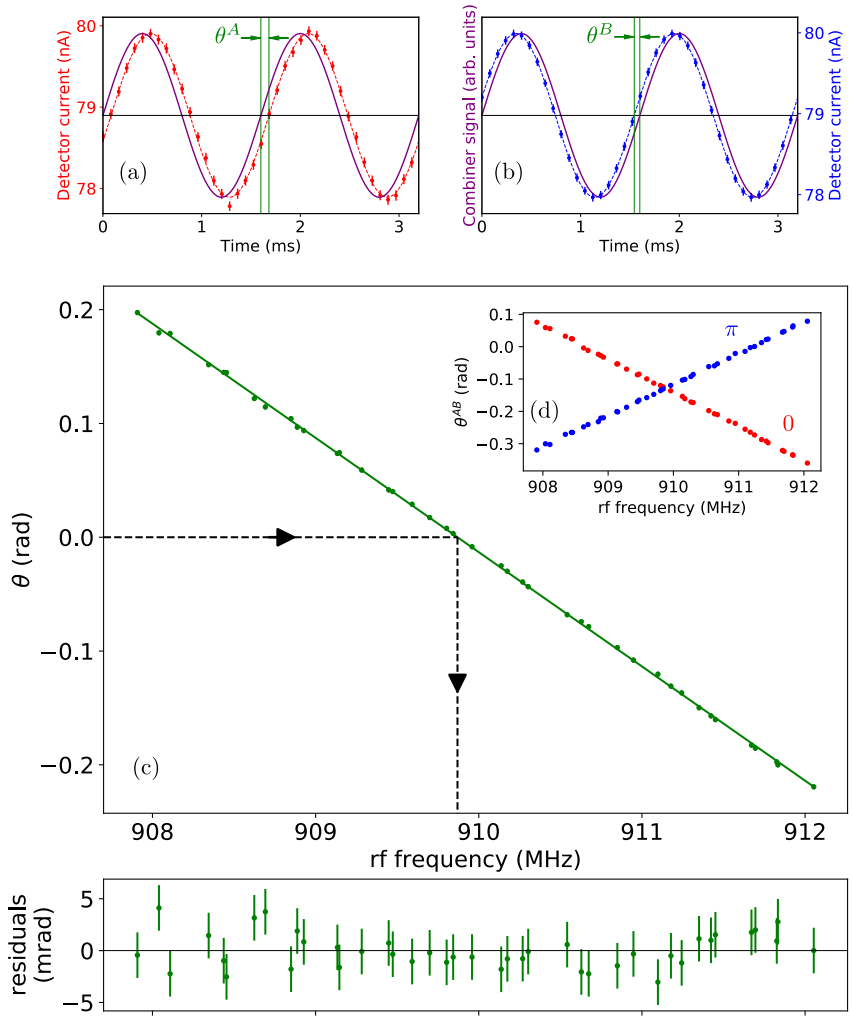

Figure 2.14: Extraction of the FOSOF phase. An example of experimental data is shown. In (a) half of the offset frequency is added to the frequency of the rf signal in the rf system for waveguide A (and half of the offset frequency is subtracted from the frequency of the rf signal supplied to the rf system for waveguide B), yielding the phase difference θ^A between the detector signal and the beatnote from one of the rf combiners. On the other hand, in (b) half of the offset frequency is added to the frequency of the rf signal in waveguide B, resulting in θ^B. The combination, $\theta^{AB} = \frac{1}{2}(\theta^A - \theta^B)$, which is free from phase offsets due to the frequency response at the offset frequency, is shown in red for the 0 configuration and in blue for the π configuration (d). Half the difference of these two curves gives the FOSOF phase $\theta = \frac{1}{2}(\theta^{AB}_{(0)} - \theta^{AB}_{(\pi)})$, as shown in (c). For this data set (acquired in less than 90 minutes), a linear fit gives an uncertainty of 2.2 kHz in the zero-crossing frequency with $\chi^2 = 29.1$ for 39 degrees of freedom.

transimpedance amplifier attached to the detector. Therefore, there is an additional phase offset $\delta\phi_{\rm det}$ that depends on the offset frequency: $\phi_{\rm det} = \theta + \phi_2 - \phi_1 + \delta\phi_{\rm det}$.

Therefore, the phase difference between the component of the Lyman-α-detector signal oscillating at Δf and the beatnote from combiners C1 and C2 is not equal to the FOSOF phase θ, but is equal to

$$\phi_{\rm det} - \phi_{\rm beat} = \theta + \delta\phi_{\rm det} - \delta\phi_{\rm beat}. \tag{2.4}$$

A way to eliminate these phase offsets ($\delta\phi_{\rm beat}$ and $\delta\phi_{\rm det}$) from Eq. 2.4 is to perform two FOSOF experiments, shown in panels (a) and (b) (or (c) and (d)) of Fig. 2.13. The entire rf system (including waveguides A and B, the cables, combiners, power monitors, dual rf generator, and amplifiers) is rotated as a unit (including in- and out-of-vacuum components) to move from one of these configurations to the other. The phase of the rf field in waveguides A and B is $2\pi(f - \frac{\Delta f}{2}) + \phi_1$ and $2\pi(f + \frac{\Delta f}{2}) + \phi_2$, respectively, where f is the rf frequency. In the first experiment (Fig. 2.13 (a)), the atoms travel through waveguide A and then through waveguide B (the 0 configuration). In this case, the phase difference between the offset-frequency (Δf) component of the Lyman-α-detector signal and the beatnote from the combiners is given by the same expression as in Eq. 2.4:

$$\theta_{(0)} = \phi_{\rm det(0)} - \phi_{\rm beat(0)} = \theta + \delta\phi_{\rm det} - \delta\phi_{\rm beat}. \tag{2.5}$$

In the second experiment (Fig. 2.13 (b)), the order of the waveguides is reversed (the π configuration). In this case, the component of the Lyman-α signal oscillating at the offset frequency has the phase equal to $\phi_{\rm det(\pi)} = -\theta + (\phi_2 - \phi_1) + \delta\phi_{\rm det}$, and the expression for the phase of the beatnote from the combiners, $\phi_{\rm beat(\pi)}$, is the same as for the first experiment. The difference between $\phi_{\rm det(\pi)}$ and $\phi_{\rm beat(\pi)}$ is equal

to:

$$\theta_{(\pi)} = \phi_{\mathrm{det}(\pi)} - \phi_{\mathrm{beat}(\pi)} = -\theta + \delta\phi_{\mathrm{det}} - \delta\phi_{\mathrm{beat}}. \tag{2.6}$$

Half of the difference of the FOSOF phases acquired for the 0 and π configurations (Eq. 2.5 and 2.6) yields a phase-offset-free phase, equal to the FOSOF phase θ:

$$\theta = \frac{1}{2}(\theta_{(0)} - \theta_{(\pi)}). \tag{2.7}$$

An example of data acquired for the 0 and π configurations is shown in panel (d) of Fig. 2.14. Panel (c) of Fig. 2.14 shows the FOSOF phase extracted from combining the data from these two configuration using Eq. 2.7.

The waveguide reversal is performed in situ by rotating the whole rf system (including the amplifiers, the rf generator and all of the interconnecting cables) by 180 degrees every 30-60 minutes, while ensuring that none of the rf components are disturbed during the rotation.

This method negates the unwanted phase shifts ($\delta\phi_{\mathrm{beat}}$ and $\delta\phi_{\mathrm{det}}$), provided that these phase offsets stay constant for the duration of data acquisition for both the 0 and π configurations. The stability of the phase offset ($\delta\phi_{\mathrm{beat}}$) related to the rf system is discussed in Sec. 3.8. As for the detector-related phase offset ($\delta\phi_{\mathrm{det}}$), it was determined that the detector-gain stability over the period of 30-60 minutes was not sufficient for the accuracy of the current measurement[20].

A different method is used to correct for the Lyman-α-detector phase offset at the offset frequency at much faster time scale (about every 10 seconds). Note that in addition to changing the orientation of the waveguides, we can also change which rf arm has half of the offset frequency, $\frac{\Delta f}{2}$, added (see the first or the second column of Fig. 2.13). Consider panel (a) of Fig. 2.13. Half of the offset frequency is added

[20]For example, we determined that the detector bandwidth is a function of the beam current and it also depends on the pressure of the acetone gas in the detector.

to waveguide B and subtracted from waveguide A, and the phase difference between the offset-frequency component of the Lyman-α-detector signal and the beatnote from the combiners is given by Eq. 2.5, which we will now denote by $\theta^B_{(0)}$. In panel (c) of Fig. 2.13, half of the offset frequency is now added and subtracted from the opposite waveguides. In this case, the phase of the component oscillating at the offset frequency from the Lyman-α detector is given by

$$\phi^A_{\mathrm{det}(0)} = -(\theta + (\phi_2 - \phi_1)) + \delta\phi_{\mathrm{det}}, \tag{2.8}$$

while the phase of the beatnote from the combiners is:

$$\phi^A_{\mathrm{beat}(0)} = -(\phi_2 - \phi_1) - \delta\phi_{\mathrm{beat}}. \tag{2.9}$$

The phase difference between these two phases is

$$\theta^A_{(0)} = -\theta + \delta\phi_{\mathrm{det}} + \delta\phi_{\mathrm{beat}}. \tag{2.10}$$

The half-difference of the extracted phase differences, yields the phase difference:

$$\theta^{AB}_{(0)} = \frac{1}{2}(\theta^B_{(0)} - \theta^A_{(0)}) = \theta - \delta\phi_{\mathrm{beat}}, \tag{2.11}$$

which is free of the offset-frequency-dependent phase offset in the Lyman-α-detector signal. Examples of A and B data are shown in panels (a) and (b) of Fig. 2.14. A similar procedure is used for the other orientation of the waveguides (the π configuration) to obtain $\theta^{AB}_{(\pi)} = -\theta - \delta\phi_{\mathrm{beat}}$. Half the difference of $\theta^{AB}_{(0)}$ and $\theta^{AB}_{(\pi)}$ gives the FOSOF phase θ:

$$\theta = \frac{1}{2}(\theta^{AB}_{(0)} - \theta^{AB}_{(\pi)}). \tag{2.12}$$

2.9 Power calibration for the rf system

The FOSOF lineshape (Eq. 1.23) depends on the amplitude of the rf electric field (which affects the slope of the linear fit to the FOSOF lineshape). The consequence

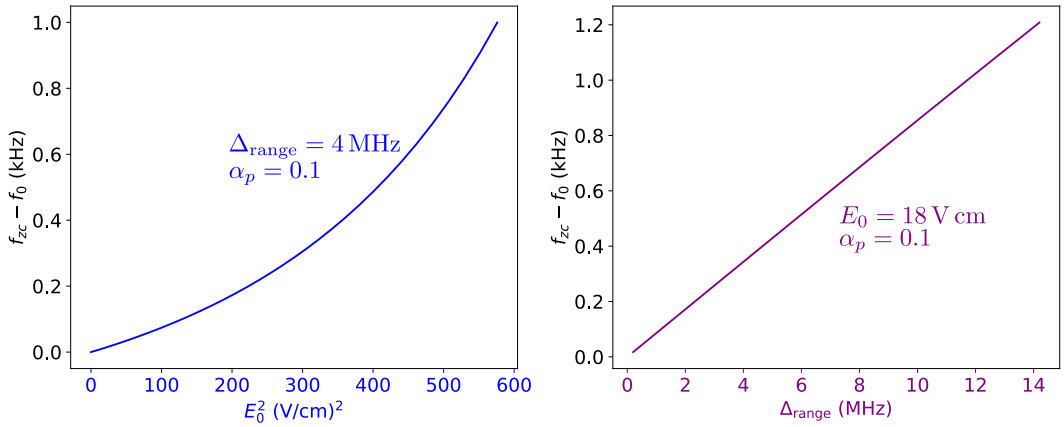

Figure 2.15: Effect of the power-flatness level on the zero-phase-crossing frequency, f_{zc}. $f_{zc} - f_0$ is the shift of the zero-crossing frequency from the resonant frequency f_0. In both panels (a) and (b), symmetric frequencies about f_0 are used. α_p (Eq. 2.14) is the total fractional linear change in the square of the electric field amplitude across the detuning range (Eq. 2.16). In both (a) and (b), $\alpha_p = 0.1$, equivalent to a 10% change in the power across the detuning range (about 5% change in the field amplitude). In (a), the frequency detuning range is $\Delta_{\text{range}} = 4\,\text{MHz}$, and in (b), the electric field amplitude at f_0 is $E_0 = 18\,\text{V cm}$. The frequency shift, $f_{zc} - f_0$ is proportional to α_p for the same δf and E_0.

of this is that the lineshape obtained with imperfect power flatness across the detuning range, Δ_{range}, could lead to a shift in the observed FOSOF resonant frequency. To be more specific, the power flatness can be represented as

$$P - P_0 = P'\delta f + \frac{1}{2!}P''\delta f^2 + \frac{1}{3!}P'''\delta f^3 + \ldots, \tag{2.13}$$

where P_0 is the field power at the resonant frequency f_0, P is the power at a frequency detuning $\delta f = f - f_0$.

As an example of a frequency shift due to a dependence of the rf electric field in the FOSOF regions on the frequency detuning, we consider a case of a small monotonic change in the power across the detuning range. For simplicity, we also assume that in the FOSOF regions, the pulses of the rf electric field are square, as

shown in Fig. 1.7. In this case, it is useful to define a total fractional power change across the detuning range:

$$\alpha_P = \frac{P[\delta f_{\max}] - P[\delta f_{\min}]}{P_0}, \tag{2.14}$$

where $P[\delta f_{\max}]$ and $P[\delta f_{\min}]$ are the rf powers at the maximum and minimum detunings in the detuning range Δ_{range}, respectively. For small values of the parameter α_P, the first-order term in Eq. 2.13 is the largest contribution to the power flatness. The power as a function of the frequency detuning can be expressed as

$$P = (\alpha_P \frac{\delta f}{\Delta_{\text{range}}} + 1)P_0. \tag{2.15}$$

Eq. 2.15 can be written in terms of the square of the rf electric field amplitude, E:

$$E^2 = (\alpha_P \frac{\delta f}{\Delta_{\text{range}}} + 1)E_0^2, \tag{2.16}$$

with $E^2 \propto P$ and $E_0^2 \propto P_0$. Deviations of the zero-crossing frequency f_{zc} from the resonant frequency f_0 for various values of α_P, Δ_{range}, and E_0 are shown in Fig. 2.15 for the same T (separation between the FOSOF regions) and τ (duration of each of the rf pulses in the FOSOF regions) as in Fig. 1.5. Fig. 2.15 indicates that the effect of the imperfect power flatness on the deviation of the zero-phase crossing frequency from the resonant frequency is smaller for smaller rf electric field amplitudes and for smaller range of detunings. In our experiment, we use a frequency range of 4 MHz, and field amplitudes of up to 24 V/cm. Figure 2.15 indicates that for a frequency range of 4 MHz and an electric field amplitude of 24 V/cm, for square interaction regions and with a total change in the field power (varying linearly with the frequency detuning) of $\alpha_P = 10\%$, the zero-crossing frequency determined from the FOSOF lineshape is shifted from the resonant frequency by about 1 kHz, which is a significant shift. The concern is that it is possible that the coupling of the

power output by the rf generator into the FOSOF regions may have insufficient power flatness. Therefore, given a value of the rf electric field amplitude that atoms experience while traversing the two FOSOF regions, we need to determine the power output by the rf generator that corresponds to this field amplitude. Such a correspondence between the desired set of the field amplitudes and the rf powers output by the rf generator is determined experimentally for each of the two FOSOF regions and for the range of frequencies (of 4 MHz) used in our experiment by comparing the dependence of the observed Lyman-α-detector signal on the power setting of the rf generator with simulations of the survivability of the $2S$ atoms versus rf intensity in this FOSOF waveguide[21].

The setup to calibrate the power for the rf system for waveguide A is shown in part (a) of Fig. 2.16, and an example of the acquired data for power calibration is shown in Fig. 2.17. The figure depicts the process of determining the output power by the rf generator that corresponds to the field amplitude of 18 V/cm at a frequency of 910 MHz in waveguide A. First, we use simulated data (surviving $2S_{1/2}, f = 0$ populations after passing through a single FOSOF region as a function of rf field amplitude) to determine the surviving $2S_{1/2}, f = 0$ population that corresponds to a field of 18 V/cm in the FOSOF region. We then use the experimental data of Lyman-α-detector signal (normalized to the Lyman-α-detector signal at zero power in waveguide A) as a function of the output power by the rf generator to determine the output power at which the detector signal is equal to this simulated surviving population at 18 V/cm. There are two complications to this process. The Lyman-α-detector signal needs to be corrected for the fractional offset that was discussed in Sec. 2.5, since this offset is not related to the $2S_{1/2}, f = 0$ population. This corrections has an effect of shifting the rf power supplied to the FOSOF

[21]Details about the simulations are in Sec. 3.3.1.

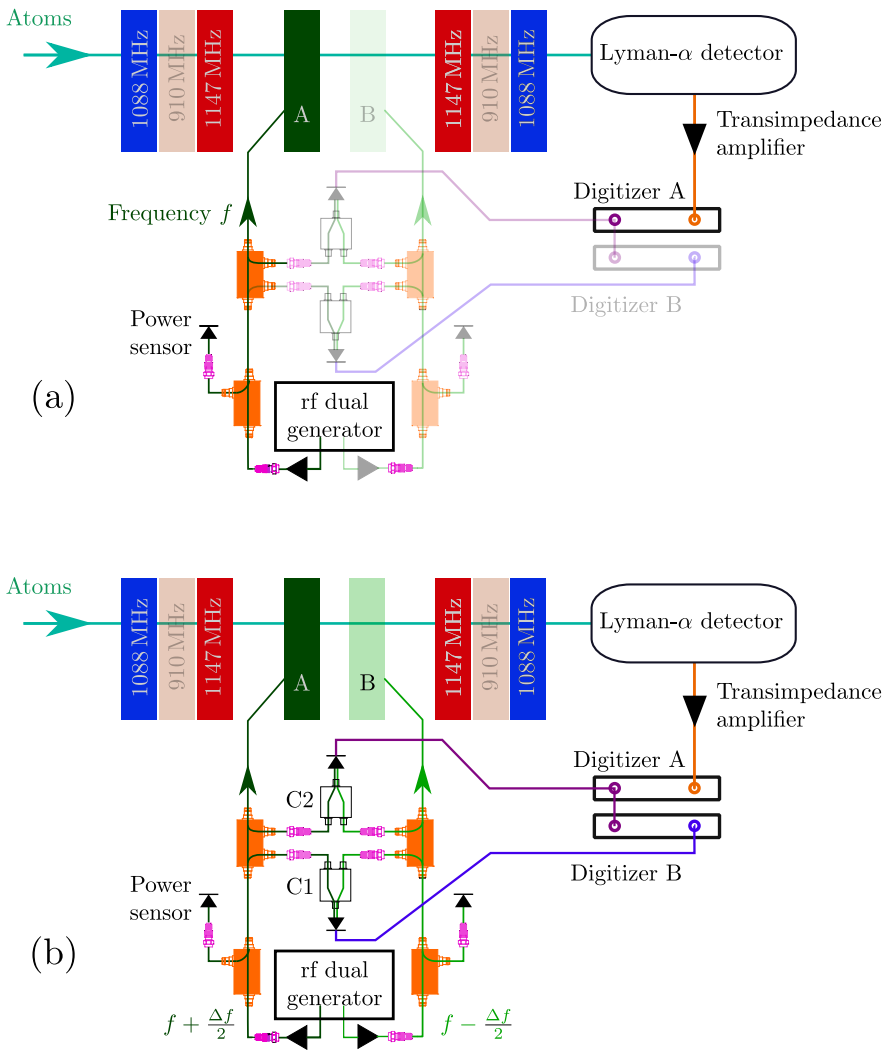

Figure 2.16: Data acquisition setups. Figure (a) is the setup for performing power calibrating for the rf system for waveguide A. Semi-transparent portions of the figure indicate the components that were not used in the calibration procedure. The quench cavities were set to their respective π pulses (except the 910-MHz cavities). Figure (b) shows the setup used for the FOSOF data acquisition. In this case the pre- and post-910-MHz cavities are not used. The waveguides are shown in the 0 configuration with half of the offset frequency added to the frequency of the rf wave in the left arm of the rf system (for waveguide A) and half of the offset frequency subtracted from the frequency of the rf wave in the right arm of the rf system (for waveguide B). The power sensors are connected to a precision multimeter (not shown).

regions by approximately the same amount for all of the frequencies in the ±2 MHz range around 910 MHz – the range of frequencies used in our experiment. The frequency shift associated with our knowledge of the fractional offset is discussed in Sec. 3.3.3. Another complication is that the power calibration procedure of Fig. 2.17 assumes that all of the atoms travel through the FOSOF regions along the same trajectory (along the central beam axis of the tubes on the waveguides), but in our experiment, the beam of $2S_{1/2}, f = 0$ atoms has nonzero size. It turns out that simulated data, such as the one in panel (a) of Fig. 2.17 differs negligibly for atoms traveling at different distances away from the beam axis (indicated by a dashed line that passes through the waveguides in Fig. 2.9). In particular, for the simulated data in Fig. 2.17, for the atoms that travel 2 mm away from the beam axis, the surviving $2S_{1/2}, f = 0$ population changes by at most 0.2%. Such a small difference in surviving populations for atoms moving at different distances away from the beam axis has a negligible effect on the power calibration[22].

2.10 Data acquisition procedure

One of the reasons for performing this high-precision measurement of the $n = 2$ Lamb shift was to compare extracted proton radii from muonic and electronic hydrogen. To have an unbiased comparison, we applied a hidden offset to all of the frequencies output by the rf generator while acquiring spectroscopic data using the FOSOF technique. The hidden offset was revealed to us only after all of the FOSOF data was acquired and its analysis was completed[23]. The front panel

[22]There is still a frequency shift associated with the beam size. This shift is discussed in Sec. 3.3.2.

[23]It took us six years to finally "unblind" the measurement! The hidden offset was constrained to be within ±100 kHz, which is more than ten times the uncertainty of the Lundeen and Pipkin measurement [10].

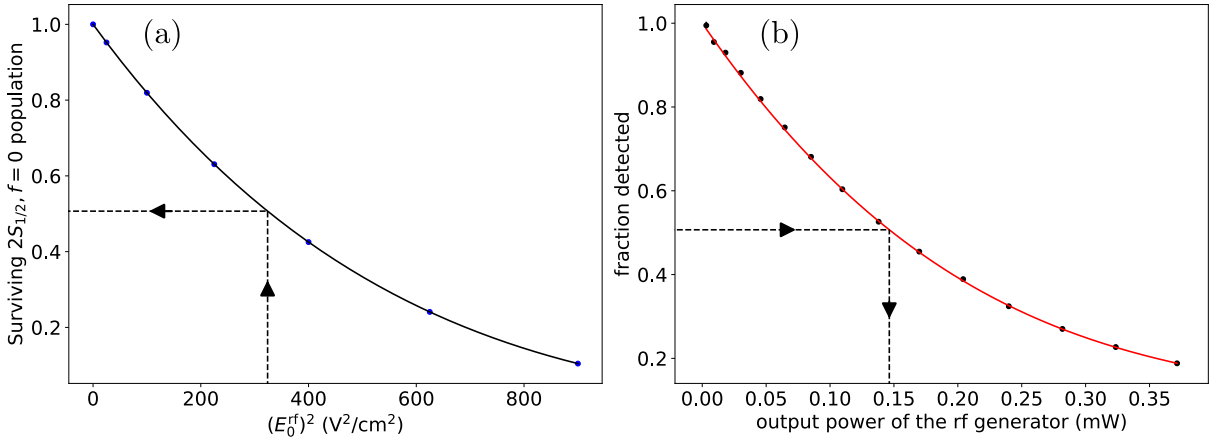

Figure 2.17: Example of data used for power calibration for an rf frequency of 910 MHz. Panel (a) is the simulated quench curve – fractional $2S_{1/2}, f = 0$ population after passing through a single FOSOF region as a function of rf field amplitude in the FOSOF region (at 910 MHz). Panel (b) shows the experimental data of Lyman-α-detector signal as a function of the output power by the rf generator into waveguide A (no power is supplied to waveguide B for these data). The signal from the detector is normalized to when no power is supplied to waveguide A. Dashed lines and arrows indicate the procedure for determining the power that needs to be output by the rf generator in order to establish an rf field amplitude of $E_0^{\mathrm{rf}} = 18\,\mathrm{V/cm}$ in waveguide A. In particular, the dashed arrows show that the simulations in (a) indicate that $E_0^{\mathrm{rf}} = (18\,\mathrm{V/cm})^2 = 324\,\mathrm{V^2/cm^2}$ leads to a survival fraction of 0.51. In (b), it can be seen that an observed survival fraction of 0.51 occurs at rf generator output power of 0.15 mW. A similar procedure was used for a set of rf frequencies within the 4-MHz range of rf frequencies used.

display of the rf generator was turned off so that we could not see the actual frequency requested from the generator. Additionally, the frequencies used were not round numbers and were not evenly spaced, to ensure that even if we accidentally saw the frequency reading on the front panel of the rf generator, we would not immediately be able to determine the blind offset.

The separation between the waveguides D (Fig. 2.9) is set by two spacers, as shown in Fig. 2.18. To change D, the waveguides are physically removed from the vacuum chamber to replace the spacers and the copper tube between the waveguides. After putting back the waveguides, the air is evacuated from the system, until a pressure of approximately $0.2\,\mu$Torr is reached. The voltage applied to the plates of the proton deflector is set to deflect the protons (Sec. 2.4) and then the settings for the proton source are adjusted, until a stable signal is observed on the Lyman-α detector (Sec. 2.2). Afterwards, the power supplied to the hyperfine-state-selecting cavities is set to π pulses by following the procedure described in Sec. 2.5. Finally, a new power calibration for the two FOSOF waveguides is performed (Sec. 2.9) following any change in D.

The phase difference between the beatnote signals from combiners C1 and C2 is continuously monitored to help ensure that before starting to collect spectroscopic data the rf system is stable. We wait whenever the rf power is changed before starting data acquisition. That is, when we set the rf generator to output the power corresponding to the new electric field amplitude (of, for example, $5\,\mathrm{V/cm}$), we wait for the temperature distribution for the overall rf system to stabilize. An example of the change in the phase difference between the two combiners after changing the electric field amplitude in the waveguides is shown in Fig. 2.19. In this figure, the change of about $0.8\,$mrad is observed, which corresponds to a frequency shift of about $8\,$kHz. This example shows the importance of having at least two locations

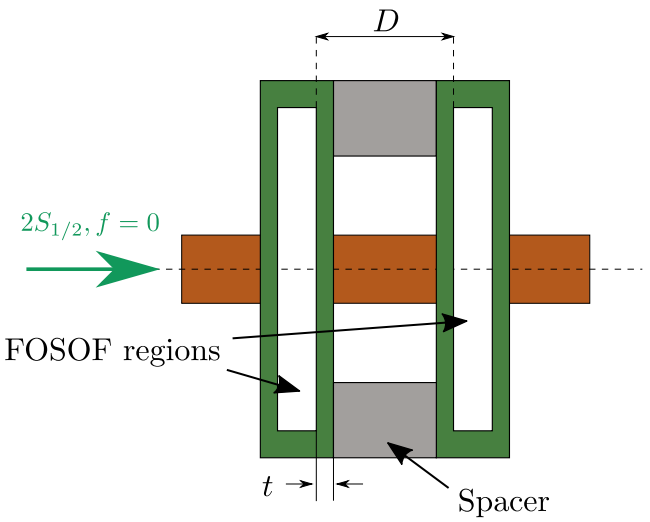

Figure 2.18: Top cross-sectional view of the FOSOF waveguides. The beam axis (Fig. 2.9) is indicated by a horizontal dashed line. The walls of the waveguides of thickness $t = 0.750 \pm 0.005$ inches are shown in green. Two aluminum spacers set the separation D between the waveguides. They have a thickness of $D - 2t$, and are machined to a tolerance of 0.002 inches. Their length (the dimension into the page) matches the length of the waveguides of 445 mm (Fig. 2.9).

(using C1 and C2) for monitoring the beatnote between the two arms of the rf system.

The setup for the data acquisition is shown in panel (b) of Fig. 2.16. Two 2-channel Keysight L4532A digitizers are used to simultaneously record signals from the Lyman-α detector, combiner C1, and combiner C2. The sampling rate is set to be much higher than the offset frequency, and the trace length is chosen such as to prevent spectral leakage from both the AC harmonics and the offset frequency, and also to have large enough signal-to-noise ratio in the Lyman-α-detector signal

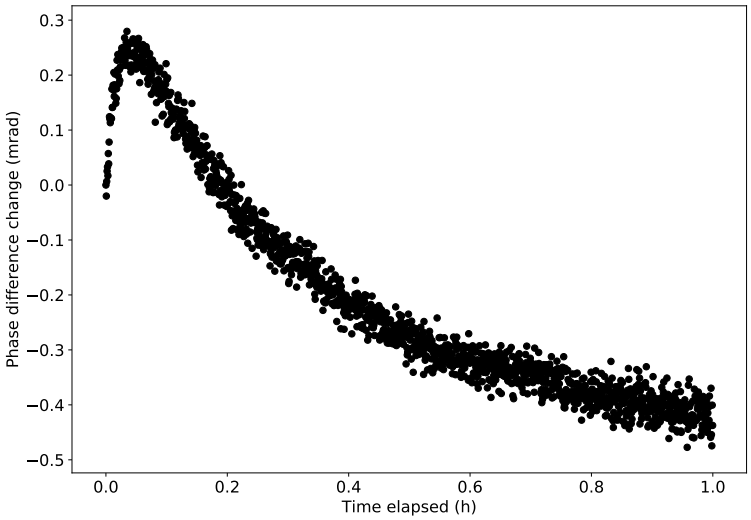

Figure 2.19: Drift in the phase difference between combiners C1 and C2. The electric field amplitude in the waveguides was changed from 18 V/cm to 5 V/cm. The rf frequency was set to 910 MHz and the offset frequency is equal to 800 Hz.

for reliable phase determination[24].

During the FOSOF data acquisition, the order of rf frequencies is randomized, which are listed in Table B.2[25]. The choice of waveguide to which half of the offset frequency is added (i.e., the one with $f + \frac{\Delta f}{2}$) is randomized as well, with the other waveguide having this higher frequency in the subsequent measurement. The acquisition scheme is shown in Fig. 2.20. For this particular example, after the data is collected for the 0 configuration the waveguides are reversed and the acquisition is performed for the π configuration. As described in Sec. 2.8, both of these data sets are required to determine the resonant frequency. To acquire another 0- and

[24]Depending on the separation between the waveguides and the electric field amplitude, the trace length varied from 1-10 seconds. The sampling rate was usually set to 100 kilo-samples per second. Much smaller values for the sampling rate would suffice, but we wanted to have an opportunity to examine if there were any indications of unexpected signals at frequencies higher than the offset frequency (none were found).

[25]For this measurement, FOSOF data sets are acquired with the same set of 41 rf frequencies.

π-configuration pairs, we start with the waveguides in the π configuration, and then rotate the waveguide to change to the 0 configuration.

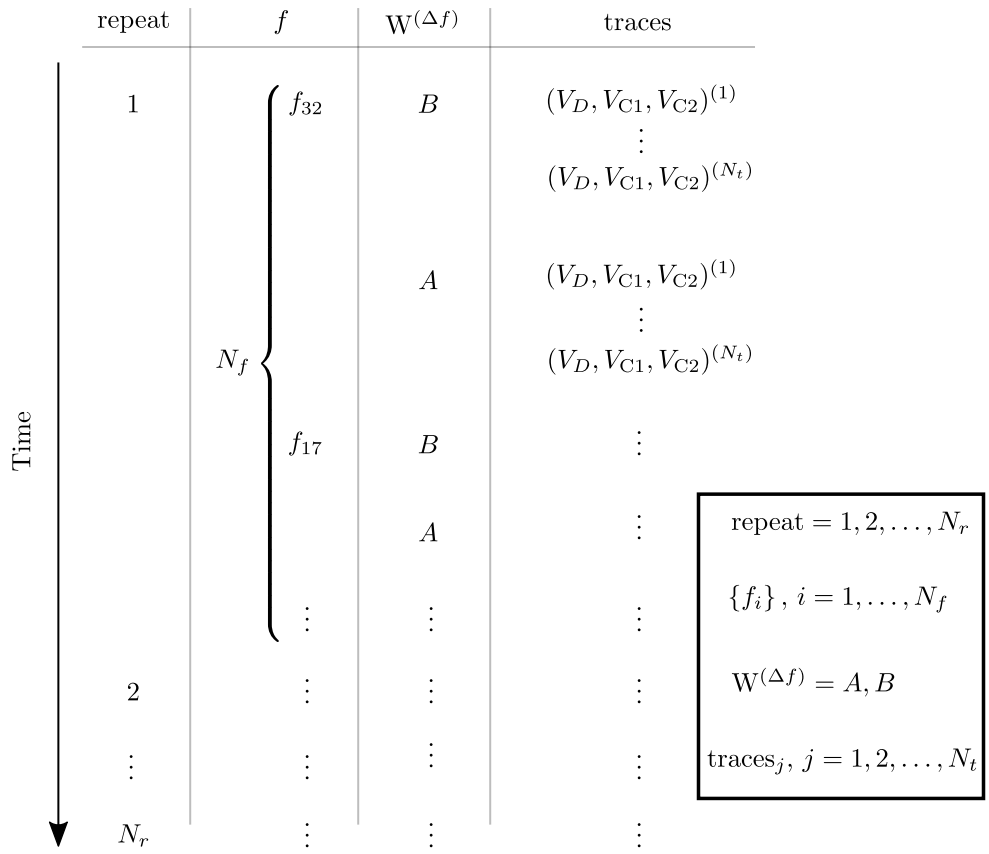

Figure 2.20: Data collection diagram arranged as a table. Each data set is acquired by cycling through the following procedure N_r times (the first column). The rf frequency is randomly picked out of the set of rf frequencies $\{f_i\}$ (the second column). Then, randomly as well, it is chosen whether half of the offset frequency $\frac{\Delta f}{2}$ is added to the frequency of the rf signal in waveguide A or B, indicated by $\mathrm{W}^{(\Delta f)}$ in the third column. It is shown, as an example, that at first (shown in the first row) the signal in waveguide A has frequency $f_{32} - \frac{\Delta f}{2}$, and in waveguide B the field is oscillating at frequency $f_{32} + \frac{\Delta f}{2}$. Traces of the signals acquired from the Lyman-α detector (V_D), combiner C1 (V_{C1}), and combiner C2 (V_{C2}) form the tuple of traces $(V_D, V_{\mathrm{C1}}, V_{\mathrm{C2}})$. These traces are acquired N_t times (the fourth column). After the set of traces is collected, half of the offset frequency is added to the frequency of the signal in waveguide A, and another set of traces is acquired N_t times. The process continues until the data for all of the N_f frequencies is collected. Each tuple of traces can be uniquely labeled by a tuple of four numbers: $(\mathrm{repeat}, f, \mathrm{W}^{(\Delta f)}, \mathrm{traces})$, i.e., by the numbers in the four columns.

3 Systematic shifts

The zero-phase-crossing frequencies, f_{zc}, determined from FOSOF lineshapes are subject to several systematic effects, which are discussed in this chapter. A final list of systematic corrections applied is shown in Table 4.1.

3.1 Second-order Doppler shift

The first-order Doppler effect is expected to be very small, and will be treated in Sec. 3.7. Due to relativistic time dilation, in a reference frame co-moving with the atomic beam, an rf frequency seen by the atoms is higher than the frequency of the fields in the laboratory frame. This leads to a second-order Doppler shift[26]:

$$\Delta_{\mathrm{SOD}} \equiv f' - f = (\gamma - 1) f \approx \frac{1}{2}\frac{v^2}{c^2} f, \tag{3.1}$$

where f' is the frequency in the atom's reference frame, f is the frequency in the laboratory frame, c is the speed of light in vacuum, v is the speed of the atoms, and $\gamma = (1 - v^2/c^2)^{-1/2}$. For the atoms moving at 1% of the speed of light, the approximation of Eq. 3.1 is justified since the v^4/c^4 (fourth-order Doppler shift)

[26]One might expect the frequency to actually decrease based on the following argument. Consider an atom exposed to a traveling wave, perpendicular to the velocity of the atom. In the atom's reference frame, the rf generator is moving with some velocity $\vec{v}$, and thus emission of radiation of period T in the reference frame of an observer should be time-dilated by a factor γ in the atom's frame, which concludes that the frequency seen by the atom should be smaller. However, one has to be careful about the aberration of light: the wave vector is not normal to the velocity $\vec{v}$ in the atom's frame. Details are discussed Ref. [33] (pp. 139 to 144).

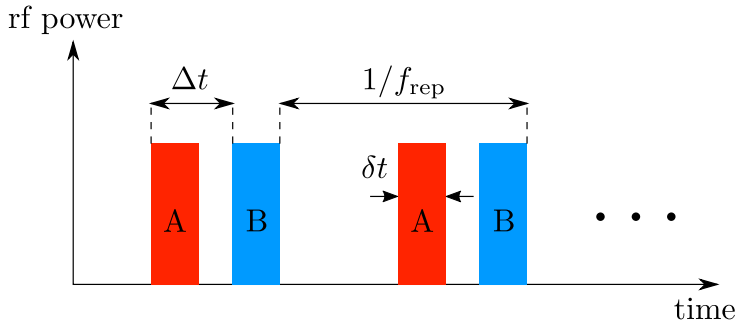

Figure 3.1: Radio-frequency pulse timing for the beam-speed measurement. The rf power for waveguides A (red) and B (blue) (these waveguides are the two FOSOF regions shown in Figs. 2.1 and 2.9) is pulsed with the timing shown. The pulse duration δt and repetition rate f_{rep} is chosen such that the atoms are not exposed to more than one electric field pulse while inside a single waveguide. The delay Δt between the pulse for waveguide A (in red) and waveguide B (in blue) is varied and the Lyman-α-detector signal is recorded.

term would lead to a shift of less than 5 Hz. The second-order Doppler shift for this speed is approximately 50 kHz. The speed of the atoms needs to be known to an accuracy of about 1% to allow for an uncertainty of less than 1 kHz in the second-order Doppler shift correction of Eq. 3.1.

In principle, the accelerating voltage (Eq. 2.1) could be used to calculate the speed of the atoms. However, we are concerned about a possibility of significant electric fields at the entrance aperture of the charge-exchange cell (Fig. 2.4) due to protons colliding with the face of the aperture, and such a potential could slow down the protons before they neutralize into hydrogen atoms.

As a result of this concern, we instead measure the speed of the atoms by pulsing the rf power in the two waveguides (the two FOSOF regions of Figs. 2.1 and 2.9) as shown in Fig. 3.1, and measuring the change in the Lyman-α-detector signal detected as a function of the delay between the pulses (as shown, for example, in Fig. 3.2). The pulsing of the rf power is realized with a SRS DG645 delay generator and two rf switches (Mini-circuits ZASWA-2-50DRA+), one for each arm of the rf

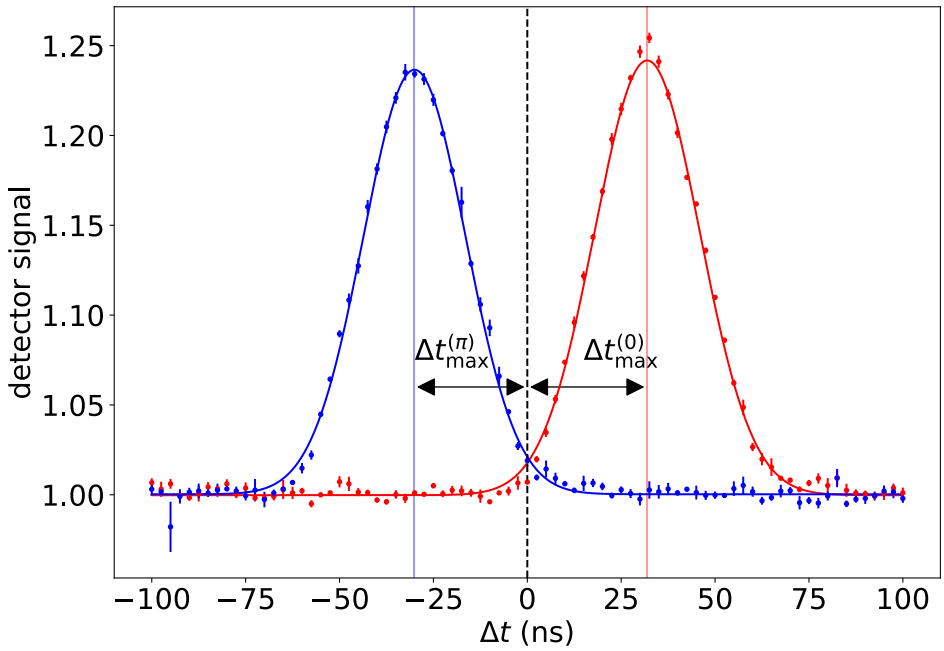

Figure 3.2: Example of data for the beam-speed measurement. The separation between the waveguides (D of Fig. 2.9) is 7 cm for this data, with the nominal accelerating voltage set to 49.86 kV. The data in red is acquired for the waveguides in the 0 configuration, and for the data in blue the waveguides are in the π configuration. The data shown is the metastable current (measured by the Lyman-α detector) normalized to the metastable current observed for large delays between the pulses. The data are fit to Gaussian functions. Pulse separations ($\Delta t^{(0)}_{\max}$ and $\Delta t^{(\pi)}_{\max}$) that correspond to the (normalized) maximal metastable currents are extracted from the fits to Gaussian functions. These two fit parameters and values of the reduced chi-squared for the two fits are shown in the last row of Table 3.1. The average of $|\Delta t^{(0)}_{\max}|$ and $|\Delta t^{(\pi)}_{\max}|$ yields a delay time Δt that is not influenced by time delays in the rf system.

system[27]. The maximal metastable current occurs when the delay between the pulses $\Delta t_{\max}$ is equal to the average time it takes for hydrogen atom to travel from one waveguide to the other. The average beam speed is

$$v = (b + D)/\Delta t_{\max}, \tag{3.2}$$

where b is the width of the waveguide (see Fig. 2.9) and D is the separation between the waveguides (as shown in Fig. 2.9). Both b and D can be measured to an accuracy of better than 0.01 cm, so that the relative uncertainty in $b + D$ is much smaller than the relative uncertainty in $\Delta t_{\max}$. The quantity $\Delta t_{\max}$ is not, in general, equal to the delay between the pulses set on the delay generator, because the two arms of the rf system (i.e., the arms that feed waveguide A and waveguide B) are not perfectly identical. Performing the experiment for the 0 and π configurations (i.e., with the two orientations of the FOSOF system), and averaging the $\Delta t_{\max}$ from the two orientations, cancels the time delays associated with the length mismatch between the rf arms. As a check for systematic effects, the beam speed is measured for several nominal accelerating voltages, defined to be equal to the floating voltage of the proton source V_{HV} (refer to Sec. 2.2).

[27]They are placed before the 30-W rf amplifiers, shown in Fig. 2.1.

Table 3.1: Data for determining second-order Doppler shifts. D is the waveguide separation, V_{HV} is the nominal accelerating voltage. The third column specifies when the data set was acquired. For each data set, we first fit the data to a Gaussian function and determine the pulse separation ($\Delta t^{(0)}_{\mathrm{max}}$ or $\Delta t^{(\pi)}_{\mathrm{max}}$ for 0 or π configurations, respectively) that corresponds to the maximal change in the metastable current (as shown in Fig. 3.2). Then, a range of ±20- and ±30-ns pulse separations about this pulse separation is selected, and these subsets of data are again fit to Gaussians functions. $\chi^2_{r(0)}$ and $\chi^2_{r(\pi)}$ are the reduced chi-squared values for the fits for the data acquired with the waveguides in the 0 and π configurations, respectively. DOF is the number of degrees of freedom for fits to Gaussian functions.

D (cm)	V_{HV} (kV)	Date (yyyy-mm-dd)	Range (ns)	$\Delta t^{(0)}_{\mathrm{max}}$(ns)	$\Delta t^{(\pi)}_{\mathrm{max}}$(ns)	$\chi^2_{r(0)}$	$\chi^2_{r(\pi)}$	DOF
4	16.27	2018-05-25	20	34.71(8)	−35.85(6)	0.9	2.8	12
4	16.27	2018-05-25	30	34.71(5)	−35.82(4)	2.1	2.2	20
4	16.27	2018-05-25	All	34.68(4)	−35.77(4)	2.6	3.8	77
4	22.17	2018-05-22	20	32.305(20)	−29.820(13)	7.3	7.1	12
4	22.17	2018-05-22	30	32.348(16)	−29.729(10)	7.4	18.9	20
4	22.17	2018-05-22	All	32.369(15)	−29.743(10)	12.1	37.2	77
4	49.86	2018-05-18	20	22.68(4)	−20.21(5)	13.6	2.3	12
4	49.86	2018-05-18	30	22.68(4)	−20.23(4)	10.6	2.3	20
4	49.86	2018-05-18	All	22.67(4)	−20.14(4)	8.5	5.1	77
5	49.86	2017-06-21	20	14.98(7)	−34.550(23)	1.0	7.7	16
5	49.86	2017-06-21	30	15.11(7)	−34.488(23)	3.5	25.1	26
5	49.86	2017-06-21	All	15.11(7)	−34.491(23)	2.0	9.0	87
5	49.86	2018-05-10	20	25.97(5)	−24.13(9)	1.9	3.2	12
5	49.86	2018-05-10	30	26.01(4)	−24.00(7)	4.0	2.6	20
5	49.86	2018-05-10	All	26.02(4)	−23.98(7)	4.6	2.8	77

Continued on next page

Table 3.1 – continued from previous page

D (cm)	V_{HV} (kV)	Date (yyyy-mm-dd)	Range (ns)	$\Delta t_{\mathrm{max}}^{(0)}$(ns)	$\Delta t_{\mathrm{max}}^{(\pi)}$(ns)	$\chi^2_{r(0)}$	$\chi^2_{r(\pi)}$	DOF
7	49.86	2017-10-23	20	20.6941(19)	−41.862(8)	24.4	42.3	16
7	49.86	2017-10-23	30	20.7066(19)	−41.858(8)	451.0	222.9	26
7	49.86	2017-10-23	All	20.7066(19)	−41.809(8)	385.1	115.7	87
7	49.86	2018-06-27	20	31.79(6)	−30.16(10)	7.9	0.4	12
7	49.86	2018-06-27	30	31.78(4)	−30.09(6)	8.6	1.7	20
7	49.86	2018-06-27	All	31.91(4)	−30.04(6)	6.6	3.0	77

Figure 3.2 shows an example of data for one of the experiments used for determining beam speed (for the case of a separation D between the FOSOF regions of 7 cm and a nominal accelerating voltage V_{HV} of 49.86 kV). In the figure, the metastable current as a function of the pulse separation set on the delay generator (Δt) is shown: the data in red and blue is acquired with the FOSOF regions in the 0 and π configurations, respectively. For each of the sets of data, to determine the pulse separation that corresponds to the maximal metastable current ($\Delta t_{\mathrm{max}}^{(0)}$ and $\Delta t_{\mathrm{max}}^{(\pi)}$ for the 0 and π configurations, respectively), the following analysis is performed. The metastable current for the whole range of pulse delays ($\Delta t \in [-100\,\mathrm{ns}, 100\,\mathrm{ns}]$ in Fig. 3.2) is fit to a Gaussian function. However, the fit quality is poor, as indicated by large reduced chi-squared values ($\chi^2_{r(0)}$ and $\chi^2_{r(\pi)}$) in Table 3.1. Therefore, the uncertainty in $\Delta t_{\mathrm{max}}^{(0)[\mathrm{All}]}$ and $\Delta t_{\mathrm{max}}^{(\pi)[\mathrm{All}]}$ from fits to Gaussian functions, when the whole range of data is considered, cannot be used as a metric of a standard deviation of $\Delta t_{\mathrm{max}}^{(0)}$ and $\Delta t_{\mathrm{max}}^{(\pi)}$. Instead, we also fit Gaussian functions to subsets of data within the ranges of $\Delta t \in [-20\,\mathrm{ns}, 20\,\mathrm{ns}]$ and $\Delta t \in [-30\,\mathrm{ns}, 30\,\mathrm{ns}]$ about the values of $\Delta t_{\mathrm{max}}^{(0)[\mathrm{All}]}$ and

Table 3.2: Pulse separations that correspond to the maximal metastable currents. The first two columns are experimental parameters: the separation between the waveguides, D, and the nominal accelerating voltage, V_{HV}. Dates when data were acquired are listed in the third column. Beam speeds are determined from Eq. 3.2 with the width of the FOSOF waveguides equal to $b = 3.000(3)\,\mathrm{cm}$. The beam speeds are listed in the last column.

D (cm)	V_{HV} (kV)	Date (yyyy-mm-dd)	Δt_{max}(ns)	v(cm/ns)
4	16.27	2018-05-25	35.257(10)	0.1985(4)
4	22.17	2018-05-22	31.072(35)	0.2253(7)
4	49.86	2018-05-18	21.445(7)	0.3264(7)
5	49.86	2017-06-21	24.82(5)	0.3224(21)
5	49.86	2018-05-10	25.04(5)	0.3195(14)
7	49.86	2017-10-23	31.283(5)	0.3197(5)
7	49.86	2018-06-27	31.019(24)	0.3224(7)

$\Delta t_{\mathrm{max}}^{(\pi)[\mathrm{All}]}$ determined when the whole range of the data is used. From these fits, we obtain four values of the pulse delays that correspond to the maximal metastable current: $\Delta t_{\mathrm{max}}^{(0)[20]}$, $\Delta t_{\mathrm{max}}^{(0)[30]}$, $\Delta t_{\mathrm{max}}^{(\pi)[20]}$, and $\Delta t_{\mathrm{max}}^{(\pi)[30]}$. We define $\Delta t_{\mathrm{max}}^{(0)}$ and $\Delta t_{\mathrm{max}}^{(\pi)}$ to be equal to $\Delta t_{\mathrm{max}}^{(0)[\mathrm{All}]}$ and $\Delta t_{\mathrm{max}}^{(\pi)[\mathrm{All}]}$, respectively. The uncertainty of $\Delta t_{\mathrm{max}}^{(0)}$ and $\Delta t_{\mathrm{max}}^{(\pi)}$ is defined to be equal to the standard deviation of $\{\Delta t_{\mathrm{max}}^{(0)[20]}, \Delta t_{\mathrm{max}}^{(0)[30]}\}$ and $\{\Delta t_{\mathrm{max}}^{(\pi)[20]}, \Delta t_{\mathrm{max}}^{(\pi)[30]}\}$, respectively[28]. Pulse separations Δt_{max} determined by averaging $\Delta t_{\mathrm{max}}^{(0)}$ and $\Delta t_{\mathrm{max}}^{(\pi)}$ and corresponding beam speeds determined with Eq. 3.2 are listed in Table 3.2.

Table 3.3 shows the comparison of the slopes calculated from simulated FOSOF lineshapes (the simulations are discussed in Sec. 3.3.1) with the slopes from fits of

[28]This definition is a reasonable choice, because the variability of the pulse separations extracted from the fits for different ranges of data is smaller than the fit uncertainty times the square root of the reduced chi squared would indicate.

the experimentally acquired FOSOF lineshapes (the slope of the FOSOF lineshape is defined in Eq. 1.29). This data acts as an independent test of the consistency of the measured beam speeds since the slope is approximately proportional to the time that it takes for the atoms to go from one FOSOF waveguide to the other one (and therefore inversely proportional to the beam speed). In all cases, the agreement between the slopes is excellent, generally much better than the 5% uncertainty attributed to the simulations (refer to Sec. 3.3.1). Specifically, for small electric field amplitudes of 5 and 8 V/cm, where the AC Stark shift is small, and therefore the simulations should be more accurate, the difference between the slopes determined from the simulations and the experiments is at a level of 1%. The low-rf-power FOSOF slopes confirm the measured speeds at the 1% level, and this 1% uncertainty is reflected in the beam speeds and the corresponding second-order Doppler-effect corrections listed in Table 3.4. The beam speeds are close to the expected beam speeds estimated with Eq. 2.1.

3.2 Shifts due to states other than the $2S_{1/2}, f = 0$ state

The nonzero offset in the quench curves (see Fig. 2.8 and Sec. 2.5) likely indicates the presence of other states in the atomic beam that contribute to the signal by cascading down to the $2S$ state after the quench regions, or down to the $2P$ state inside of the detector. It could be possible that the population in these states could be influenced by the rf fields as they pass through the FOSOF regions due, for example, to off-resonant transitions between states within an n manifold. If there were such an influence, the population in these states could depend on the phase difference between the FOSOF regions. It is then possible that the atoms in these states could perturb the FOSOF lineshape and lead to a shift in the measured linecenter. This concern is heightened by the fact that in [34] it is shown that an

Table 3.3: Comparison between FOSOF slopes determined from simulations, denoted by S_{sim}, and from experiments, denoted by S. The fractional uncertainty of 5% is assigned to all of the slopes in column S_{sim}, which is the uncertainty for the simulations (discussed in Sec. 3.3.4). Each value of the slope in column S represents the weighted average of all of the slopes for the FOSOF data sets acquired for the set of experimental parameters listed in the first three columns (waveguide separation D, nominal accelerating voltage V_{HV}, and electric field amplitude E_0^{rf}). The last column is the fractional difference between the slopes using the definition $\Delta S = S - S_{\mathrm{sim}}$.

D (cm)	V_{HV} (kV)	E_0^{rf} (V/cm)	S (mrad/kHz)	S_{sim} (mrad/kHz)	$\Delta S/S_{\mathrm{sim}}$
4	16.27	14	0.1053(7)	0.110(6)	−0.05(5)
4	22.17	14	0.106 11(34)	0.109(5)	−0.03(5)
4	49.86	5	0.091 61(27)	0.091(5)	0.01(5)
4	49.86	8	0.091 94(15)	0.091(5)	0.01(5)
4	49.86	14	0.095 44(8)	0.094(5)	0.01(5)
4	49.86	18	0.098 12(7)	0.098(5)	0.00(5)
4	49.86	24	0.110 10(11)	0.107(5)	0.03(5)
5	49.86	8	0.1102(4)	0.111(6)	−0.01(5)
5	49.86	14	0.113 17(30)	0.114(6)	−0.01(5)
5	49.86	18	0.117 37(24)	0.117(6)	−0.00(5)
5	49.86	24	0.127 63(24)	0.127(6)	0.01(5)
6	49.86	8	0.1301(9)	0.130(7)	−0.00(5)
6	49.86	14	0.1342(5)	0.133(7)	0.01(5)
6	49.86	18	0.1362(4)	0.137(7)	−0.01(5)
6	49.86	24	0.1485(6)	0.146(7)	0.01(5)
7	49.86	14	0.1517(7)	0.153(8)	−0.01(5)
7	49.86	18	0.1566(7)	0.156(8)	0.00(5)
7	49.86	24	0.1654(7)	0.166(8)	−0.00(5)

Table 3.4: Second-order Doppler-effect corrections. The uncertainties in the beam speeds include a 1% uncertainty associated with how well the beam speed measurements are confirmed by the low-rf-power FOSOF slopes (Table 3.3).

V_{HV} (kV)	v(cm/ns)	Δ_{SOD}(kHz)
16.27	0.199(2)	20.0(4)
22.17	0.225(2)	25.7(5)
49.86	0.322(3)	52.6(10)

initial population in the $3S_{1/2}$ state can cause a shift in an SOF $n = 2$ Lamb-shift measurement.

The proton deflector (discussed in Sec. 2.4) already quenches a significant fraction of the atoms in $2 < n < 5$ states produced in the charge-exchange cell, but it does not have a significant effect on the states with higher principal quantum number n. Therefore, even with the proton deflector, we cannot disregard the possibility of states with higher-n introducing a systematic shift to the linecenter measurement discussed in this work.

We perform several experiments to test if other states have an effect on our measurement of the transition frequency between the $2S_{1/2}, f = 0$ and $2P_{1/2}, f = 1$ states.

3.2.1 Controlled quench of the $2S_{1/2}, f = 0$ population

For the first test, the pre-quench cavity resonant at 910 MHz is set to a power that reduces the population in the $2S_{1/2}, f = 0$ state by a factor α (see Table 3.5) of between 2.0 and 13.5, thus reducing the size of the $2S_{1/2}, f = 0 \rightarrow 2P_{1/2}, f = 1$

Table 3.5: Estimated frequency shifts from states other than the $2S_{1/2}, f = 0$ state by toggling the rf power in the 910-MHz pre-quench cavity. All of the data sets are acquired at the same nominal accelerating voltage of 49.86 kV. The first column is the waveguide separation, the second column is the amplitude of the rf electric field in the FOSOF regions, the third column is the pressure in the vicinity of the charge-exchange cell, and the fourth column is the factor α by which the population in the $2S_{1/2}, f = 0$ state is reduced when the 910-MHz pre-quench cavity is enabled. $\langle\Delta\phi\rangle$ is the average observed FOSOF phase difference (the difference between the cases of the 910 quench off and on), and $\Delta_{n>2}^{(910)(\mathrm{exp})}$ is the estimated frequency shift of the $2S_{1/2}, f = 0 \rightarrow 2P_{1/2}, f = 1$ transition due to possible presence of other states using Eq. 3.3 (the FOSOF slopes are listed in Table 3.3). Each row represents the weighted average of N data sets acquired with the same experimental parameters. The reduced chi-squared of the weighted averages is denoted by χ^2_ν. The uncertainties in the shifts are expanded by $\sqrt{\chi^2_\nu}$ whenever $\chi^2_\nu > 1$.

D (cm)	E_0^{rf} (V/cm)	P_{CGX} (μTorr)	α	$\langle\Delta\phi\rangle$(mrad)	$\Delta_{n>2}^{(910)(\mathrm{exp})}$(kHz)	χ^2_ν	N
4	8	1.6	13.5	0.8(8)	0.7(7)		1
4	18	0.2	13.3	−0.3(5)	−0.2(4)	0.0	2
4	18	1.6	13.2	0.44(23)	0.37(19)	2.1	3
4	18	3.3	13.3	0.1(4)	0.1(4)	0.1	2
4	18	6.2	13.3	−0.6(4)	−0.51(35)	1.0	2
5	18	1.6	3.8	−0.3(5)	−1.0(16)	1.4	5
6	18	0.2	3.8	0.2(14)	0(4)		1
6	18	1.6	3.8	3.3(27)	9(7)	2.2	2
6	18	3.3	3.8	1.9(13)	5.0(35)		1
6	18	6.2	3.8	−0.2(13)	−0.6(35)		1
7	24	1.6	2.0	0.5(12)	3(8)	1.7	4

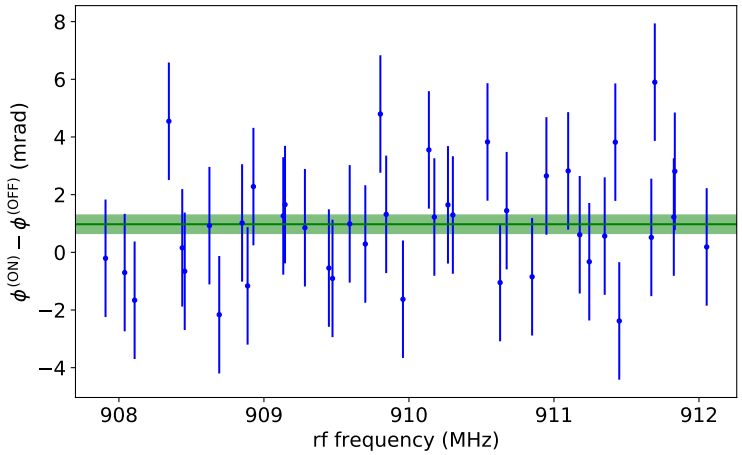

Figure 3.3: Example of the measured FOSOF phase differences from toggling the power in the 910-MHz pre-quench cavity. For this case, the waveguides are separated by $D = 4\,\text{cm}$, and the FOSOF driving field amplitude is set to $E_0^{\text{rf}} = 18\,\text{V/cm}$. The power in the 910-MHz quench cavity is set to remove 92.4% of the $2S_{1/2}, f = 0$ population (reducing it by a factor of 13.2). The weighted average of the phase differences is the thin green line, with the semi-transparent band representing one-standard-deviation uncertainty in this weighted average. For this data set, the average phase difference (Eq. 3.3) is equal to $\langle \Delta\phi \rangle = 0.95(30)\,\text{mrad}$ with the reduced chi squared of 0.95 for 40 degrees of freedom.

transition that is being driven in the FOSOF regions[29]. Because of this suppression of the intended transition, the relative effect caused by all other states is increased by a factor of 2.0 to 13.5, and the possible frequency shift due to these states is amplified by approximately the same factor. An example of data taken in this manner is shown in Fig. 3.3, where the difference in the measured FOSOF phases (the difference between having the 910 quench cavity off and on) is determined for each rf frequency in the FOSOF regions. The shift due to the higher-n states,

[29]In practice, for this test we acquire FOSOF data for the two cases: when the power is sent into the pre-quench 910-MHz-resonant cavity and when the power input for the cavity is disabled. By switching between these two states often enough, phase offsets (that might drift over time) in the FOSOF rf system cancel on average. Therefore, this experiment does not require the waveguide reversal, and it can be performed overnight in either the 0 or π configurations.

$\Delta_{n>2}^{(910)}$, can be inferred from this phase shift:

$$\Delta_{n>2}^{(910)} \approx -\frac{1}{(\alpha-1)S}\langle\Delta\phi\rangle, \tag{3.3}$$

where S is the slope of the FOSOF lineshape (see Table 3.3), $\langle\Delta\phi\rangle$ is the average phase difference observed in the measurement (see, for example, Fig. 3.3), and α is the factor by which the population of the atoms in the $2S_{1/2}, f = 0$ state is reduced. These frequency shifts are determined for different waveguide separations and rf powers.

It is also expected that the distribution of hydrogen states after the charge-exchange region is a function of the pressure of the target gas (H_2) inside the charge-exchange cell. Therefore, as the second test, the same experiment of quenching a controlled fraction of the $2S_{1/2}, f = 0$ population is performed for three additional charge-exchange pressures of 0.2, 3.3, and 6.2 μTorr (in addition to our usual charge-exchange pressure of 1.6 μTorr).

The estimated frequency shifts for the four different charge-exchange pressures are listed in Table 3.5. The inferred shifts in the table shows that no significant shifts are observed, even after the pressure of the molecular hydrogen gas inside the charge-exchange cell is varied by a factor of 30. It can be concluded that any shift due to the presence of other states is limited to less than 1 kHz.

3.2.2 Higher-n states and the proton deflector

A third test for possible effects of higher-n states is a comparison of FOSOF data acquired with and without the proton deflector enabled. This data is acquired for an rf electric field amplitude of 18 V/cm and a waveguide separation of 7 cm. At this separation, the possible frequency shift is maximized, since the FOSOF amplitude is small for $D = 7$ cm (the amplitude decreases by approximately a factor of e for every

centimeter added to the separation between the FOSOF regions), while the possible contribution to the FOSOF amplitude due to the higher-n states does not depend as strongly on the separation between the FOSOF regions and the rf electric field amplitude (since lifetimes between higher-n states are long, and transition electric dipole moments for transitions between these states are large). The difference between the zero-crossing frequencies with the proton deflector disabled ($f^{PD}_{zc(\mathrm{off})}$) and enabled ($f^{PD}_{zc(\mathrm{on})}$) is measured to be equal to

$$f^{PD}_{zc(\mathrm{off})} - f^{PD}_{zc(\mathrm{on})} = 0(7)\,\mathrm{kHz}, \tag{3.4}$$

consistent with no shift.

With the proton deflector enabled, the population in the $3S_{1/2}$ state is reduced by a factor of 24, while the $2S_{1/2}$ population is reduced by a factor of 1.3 (Sec. 2.4). Therefore, the relative population of the $3S_{1/2}$ atoms is reduced by a factor of 18 and the possible shift due to these $n = 3$ states is (similar to Eq. 3.3)

$$\Delta^{(PD)}_{n=3} = \frac{0(7)\,\mathrm{kHz}}{18-1} = 0.0(4)\,\mathrm{kHz}. \tag{3.5}$$

This shift is listed in Table 3.6.

It is also verified experimentally that the fractional offset in the quench curves of the pre-quench and post-quench cavities is almost independent of whether protons are deflected or not deflected: the fractional offset with and without the proton deflector enabled is measured to be 0.37(2)% and 0.41(1)%, respectively. Therefore, the charge exchange does not produce significant populations of the atoms in $2 < n \leq 5$ states; otherwise we would expect most of these states to get quenched in the proton deflector, giving us a smaller fractional offset and, possibly, resulting in a different resonant frequency.

3.2.3 Pressure shift

If the charge-exchange cell does not produce appreciable populations in the $2 < n \leq 5$ states, we assume that the fractional offset (shown in Fig. 2.8) is mostly due to collisional repopulation of the higher-n states in the region between the pre-quench cavities and the end of the Lyman-α detector from background gas in the vacuum chamber[30]. This conclusion leads us to a fourth test for possible shifts due to higher-n states. For the fourth test, the background pressure (P_0) is increased by a factor of 10 in the experimental region, where the proton deflector, the quench cavities, the waveguides, and the Lyman-α detector are located[31]. FOSOF data are acquired for $D = 7\,\mathrm{cm}$, $V_{\mathrm{HV}} = 49.86\,\mathrm{kV}$, and $E_0^{\mathrm{rf}} = 24\,\mathrm{V/cm}$. The difference between the zero-phase-crossing frequency determined with the system at the high pressure ($f_{n>2}^{(10P_0)}$), and at a typical pressure ($f_{n>2}^{(P_0)}$) of $P_0 = 0.2, \mu\mathrm{Torr}$ is measured to be equal to

$$f_{n>2}^{(10P_0)} - f_{n>2}^{(P_0)} = 7(8)\,\mathrm{kHz}. \tag{3.6}$$

Using this frequency difference, the estimated shift in the resonant frequency of the $2S_{1/2}, f = 0 \rightarrow 2P_{1/2}, f = 1$ transition due to the pressure in the system is equal to[32]:

$$\Delta_{n>2}^{(P)} = 0.8(9)\,\mathrm{kHz}, \tag{3.7}$$

which is consistent with no shift. This shift is listed in Table 3.6.

[30]The fractional offset is measured to be larger for higher background pressure in the volume encompassing the quench cavities and the waveguides.

[31]The increase in the pressure is achieved by periodically turning on and off one of the Turbo pumps installed in the experiment.

[32]The assumption is that if the pressure is increased by a factor of α_P, this leads to proportional fractional increase in the population of the higher-n states; that is, the population of each state with $n > 2$ increases by the same factor α_P.

Table 3.6: Estimated pressure shift and the shift due to possible presence of higher-n states in the atomic beam. These shifts are shown in the last column, and they are estimated from the frequency differences listed in the second column, as explained in Sections 3.2.2 and 3.2.3. For both of these shifts, the data are acquired with the FOSOF regions separated by 7 cm and with the nominal accelerating voltage set to 49.86 kV.

	E_0^{rf} (V/cm)	Measured difference (kHz)	Estimated shift (kHz)
Disabled proton deflector ($V_{\mathrm{PD}} = 0\,\mathrm{V}$)	18	0(7)	0.0(4)
High pressure ($10P_0$)	24	7(8)	0.8(9)

3.2.4 Overall shift due to higher-n states

The four tests discussed above, results of which are shown in Tables 3.5 (shifts determined by quenching a controlled fraction of the $2S_{1/2}, f = 0$ population) and 3.6 (shifts related to the background pressure in the experimental region and the possible presence of $n = 3$, 4 and 5 states), indicate that there are no significant shifts due to possible presence of the higher-n states in the atomic beam. We can estimate the limit that can be set on an overall shift for our present measurement due to the higher-n states. We perform such an estimation in the following way.

It is expected that the effect of higher-n states on the resonant frequency is approximately inversely proportional to the amplitude of the FOSOF interference signal A (Eqs. 1.26 and 1.21) and the FOSOF slope. Thus, we can estimate the frequency shift for a particular set of experimental parameters, by scaling the measured shifts, listed in Table 3.5, by the appropriate ratio of the interference amplitudes and FOSOF slopes, and calculating a weighted average of these scaled shifts. Numerical values of the interference amplitudes are determined from simulations, which are discussed in Sec. 3.3.1. By following this procedure, the sixth column of Table 3.7 shows the shifts calculated for all of the sets of

Table 3.7: Estimated shifts due to other states than the $2S_{1/2}, f = 0$ state. The first three columns are experimental parameters. Normalized amplitudes (A) are obtained from numerical simulations. Normalized slopes (S) are obtained from linear fits to FOSOF data. The calculated shift from toggling the rf power in the 910-MHz pre-quench cavity is denoted by $\Delta_{n>2}^{(910)}$. $\Delta_{n>2}^{(P)}$ is the estimated frequency shift due to pressure in the experimental region. The last column ($\Delta_{n=3}^{(PD)}$) is the estimated shift due to $n = 3$ states obtained by the turning off the proton deflector. Note that for a given column the uncertainties are correlated, since they are derived from the same data. The last row lists the weighted average of the shifts, which are calculated by following the same procedure as in Sec. 4.3, using the same weights as in Sec. 4.1.

D (cm)	V_{HV} (kV)	E_0^{rf} (V/cm)	A	S	$\Delta_{n>2}^{(910)}$(kHz)	$\Delta_{n>2}^{(P)}$(kHz)	$\Delta_{n=3}^{(PD)}$(kHz)
4	16.27	14	4.8	0.64	0.8(7)	0.3(3)	0.0(2)
4	22.17	14	7.5	0.64	0.5(4)	0.2(2)	0.0(1)
4	49.86	5	6.5	0.55	0.7(6)	0.2(3)	0.0(2)
4	49.86	8	14.5	0.56	0.3(2)	0.1(1)	0.0(1)
4	49.86	14	27.8	0.58	0.2(1)	0.1(1)	0.0(0)
4	49.86	18	28.6	0.59	0.1(1)	0.0(1)	0.0(0)
4	49.86	24	18.4	0.67	0.2(2)	0.1(1)	0.0(0)
5	49.86	8	5.5	0.67	0.7(5)	0.2(3)	0.0(2)
5	49.86	14	10.6	0.68	0.4(3)	0.1(1)	0.0(1)
5	49.86	18	10.8	0.71	0.3(3)	0.1(1)	0.0(1)
5	49.86	24	7.0	0.77	0.5(4)	0.2(2)	0.0(1)
6	49.86	8	2.1	0.79	1.5(12)	0.5(6)	0.0(4)
6	49.86	14	4.0	0.81	0.8(6)	0.3(3)	0.0(2)
6	49.86	18	4.1	0.82	0.7(6)	0.2(3)	0.0(2)
6	49.86	24	2.6	0.90	1.1(8)	0.3(4)	0.0(2)
7	49.86	14	1.5	0.92	1.8(14)	0.6(7)	0.0(4)
7	49.86	18	1.6	0.95	1.7(14)	0.6(6)	0.0(4)
7	49.86	24	1.0	1.00	2.5(20)	0.8(9)	0.0(6)
			Weighted average:		0.9(7)	0.30(34)	0.00(21)

experimental parameters for which the spectroscopic data is acquired. Similar steps are taken for estimating the shifts for all of the experimental parameters using the data in Table 3.6, which are related to the pressure shift and the shift due to $n = 3$ states estimated from the test in which the proton deflector is turned off (shown in the two last columns of Table 3.7).

By including these estimated shifts into the final statistical analysis that is discussed in Sec. 4.3, the weighted averages of the shifts due to the possible presence of the higher-n states can be calculated (using the same weights as in Table 4.1). These weighted averages are shown in the last row of Table 3.7. Each of these three shifts is an independent determination of the shift from the higher-n states. Therefore, the overall shift due to the higher-n states can be defined as the weighted average of these three shifts. This weighted average is equal to

$$\Delta_{n>2}^{\text{tot}} = 0.13(17)\,\text{kHz}. \tag{3.8}$$

This weighted average is very small and consistent with no shift, and, as a result, we do not apply any corrections due to possible presence of states other than the $2S_{1/2}, f = 0$ state to our measurement. If one were to apply the shift in Eq. 3.8 to the resonant frequency of the $2S_{1/2}, f = 0 \rightarrow 2P_{1/2}, f = 1$ transition quoted in this work, it would need to be to be subtracted from the resonant frequency.

With respect to the total uncertainty of $\sigma = 3.2\,\text{kHz}$ for our measurement, if we include the correction in Eq. 3.8, then it does not have a significant effect on the final quoted result: the resonant frequency would change by 0.04σ. Also, the uncertainty of our measurement would increase by only $0.005\,\text{kHz}$ (0.001σ), which is insignificant.

3.2.5 Conclusion

We have shown that the four tests described in Sec. 3.2 indicate that, at the level of precision of our measurement, there are no shifts associated with the possible presence of the states other than the $2S_{1/2}, f = 0$ state. If we include this correction, the result quoted in this work changes by only 0.04σ, with the uncertainty remaining essentially unchanged. We choose not to include this correction into our list of systematic corrections, shown in Table 4.2.

3.3 AC Stark shift

Since fields that drive the $2S_{1/2}, f = 0 \rightarrow 2P_{1/2}, f = 1$ transition have an anti-rotating term (the $e^{-i2\pi ft}$ term in addition to the $e^{+i2\pi ft}$ term that drives the transition), and because of the weak coupling between the $2S_{1/2}$ and $2P_{3/2}$ states, there is a rf-power-dependent shift (an AC Stark shift) in the observed resonant frequency of the transition.

3.3.1 FOSOF simulations

To accurately calculate the rf-power-dependent shift of the resonant frequency, the density-matrix formalism is used for the $n = 1$ and 2 manifolds (including all 20 states). The time evolution of the density matrix is calculated numerically for the entire experimental process, starting from just after the charge-exchange cell, and ending with the Lyman-α detector. The simulation incorporates the three spacial components of the electric field of the proton deflector, of the rf electric fields in all of the quench cavities and the waveguides, of the electric field inside the Lyman-α detector, and, finally, of the residual background magnetic field in the experiment.

Table 3.8: AC Stark shifts calculated from the simulations. The first three columns are experimental parameters. The fourth column is the AC Stark shift for the atoms collinear with the experiment axis. The change in the AC Stark shift shift due to the nonzero beam diameter (assuming an rms radius of 1.70 mm from the experiment axis) $\Delta_{\mathrm{AC}}^{(r)}$ is shown in the fifth column. The sixth column lists the change in the AC Stark shifts due to including the fractional offset observed at π pulses of the quench curves for the pre-quench and post-quench cavities. The last column is the total AC Stark shift. It includes a 5% fractional uncertainty associated with how well the simulations model the actual experiment, as well as an uncertainty in the rms distance of the atoms from the experiment axis and an uncertainty due to the offset effect of column 6.

D (cm)	V_{HV} (kV)	E_0^{rf} (V/cm)	$\Delta_{\mathrm{AC}}^{(E_0^{\mathrm{rf}})}$ (kHz)	$\Delta_{\mathrm{AC}}^{(r)}$ (kHz)	$\Delta_{\mathrm{AC}}^{(\mathrm{offset})}$ (kHz)	Δ_{AC} (kHz)
4	16.27	14	23.4(12)	2.7(14)	2.5(12)	28.6(23)
4	22.17	14	28.6(14)	1.2(6)	2.6(13)	32.4(22)
4	49.86	5	3.5(2)	0.8(4)	1.2(6)	5.5(8)
4	49.86	8	10.3(5)	1.5(7)	1.8(9)	13.5(13)
4	49.86	14	35.6(18)	3.4(17)	3.9(19)	42.9(33)
4	49.86	18	64.1(32)	5.1(26)	5.8(29)	75.1(54)
4	49.86	24	132.8(66)	10.9(54)	9.2(46)	152.9(105)
5	49.86	8	7.0(4)	2.6(13)	0.3(2)	10.0(14)
5	49.86	14	28.2(14)	4.1(20)	2.1(11)	34.4(29)
5	49.86	18	52.2(26)	5.5(27)	3.9(19)	61.6(46)
5	49.86	24	111.1(56)	10.3(52)	7.3(37)	128.8(90)
6	49.86	8	6.2(3)	2.0(10)	0.1(1)	8.3(11)
6	49.86	14	24.1(12)	3.4(17)	1.6(8)	29.1(24)
6	49.86	18	44.7(22)	4.6(23)	3.1(15)	52.4(38)
6	49.86	24	96.3(48)	8.8(44)	5.8(29)	110.9(77)
7	49.86	14	22.2(11)	1.7(8)	2.3(12)	26.3(20)
7	49.86	18	40.7(20)	2.5(12)	3.6(18)	46.8(32)
7	49.86	24	85.6(43)	7.0(35)	6.0(30)	98.6(68)

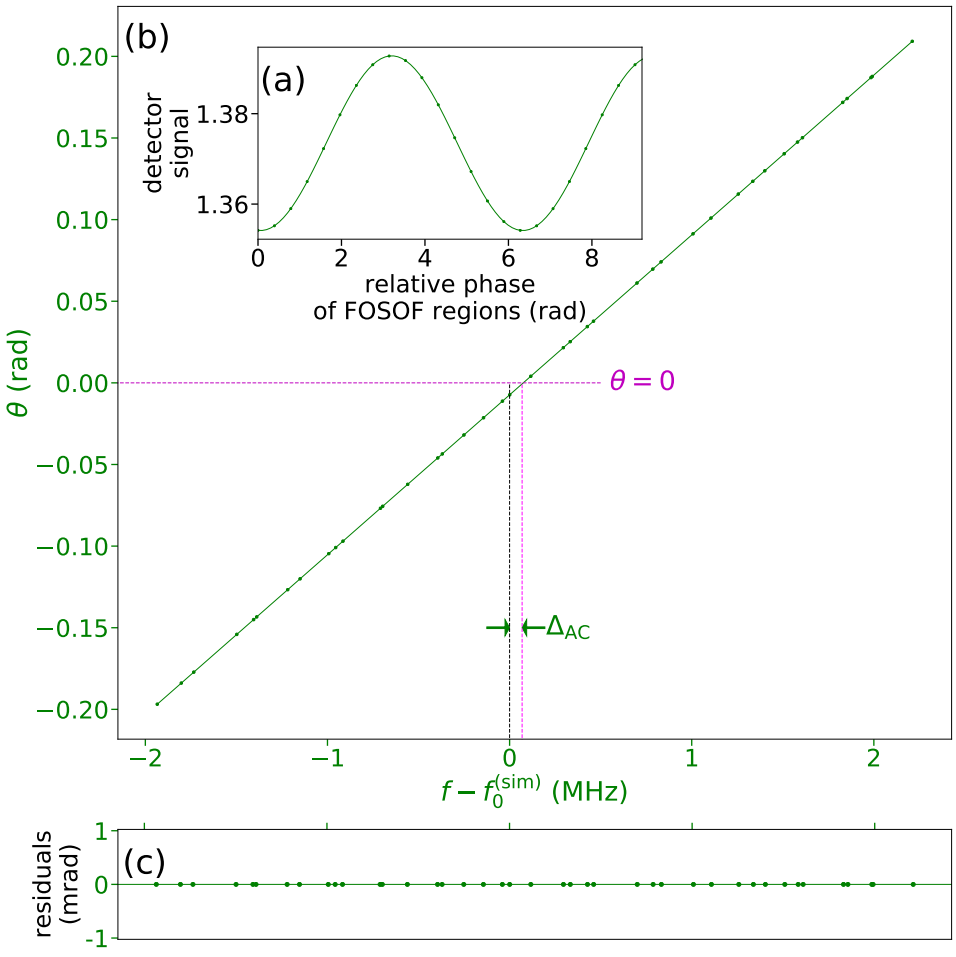

Figure 3.4: An example of the determination of the AC Stark shift from a simulated FOSOF lineshape. The simulations described in Sec. 3.3.1 determine the signal size as a function of the relative phase of the rf fields in the two FOSOF regions (a). The phase of the sinusoidal variation of this signal, θ (the FOSOF phase), is plotted in (b) as a function of the frequency detuning of the rf fields in the FOSOF regions from the resonant frequency $f_0^{(\mathrm{sim})}$ of the $2S_{1/2}, f = 0 \rightarrow 2P_{1/2}, f = 1$ transition used in the simulations. The resulting FOSOF lineshape is fit to a straight line. The AC Stark shift Δ_{AC} is the frequency detuning at which the FOSOF phase is zero. The residuals in (c) have a smaller than 0.02-mrad deviation of the FOSOF phases from the line fit.

These simulations are performed by A. Marsman[33]. Similar simulations were used in Refs. [9, 34] and are described there.

It is important to mention that the simulations employ the same procedure as described in Sec. 2.5 to determine the required rf power for the quench cavities for quenching the atoms in the $2S_{1/2}, f = 1$ state. In addition, power calibrations for the waveguides (see Sec. 2.9) are performed by using the quench curves calculated with the same simulation model. The simulated FOSOF lineshapes are calculated for the same frequencies as were used in the experiment. Zero-crossing frequencies are determined in the same way as for the acquired FOSOF data.

An example of determination of the AC Stark shift from the simulations is shown in Fig. 3.4. For the experimental parameters used in our experiment, the determined AC Stark shifts (using the same method as described in Fig. 3.4) are shown in the fourth column of Table 3.8. The shifts are found to be approximately linear in $(E_0^{\rm rf})^2$ for smaller values of $E_0^{\rm rf}$, but for larger values of $E_0^{\rm rf}$, where the shifts are quite large, an additional $(E_0^{\rm rf})^4$ term becomes significant. We assign a 5% uncertainty to all of the calculated shifts (the justification of this 5% uncertainty is given in Sec. 3.3.4). The price we pay for this 5% uncertainty is that most of the data acquired at high signal-to-noise ratios (for rf electric field amplitudes of $E_0^{\rm rf} = 18$ and $24\,{\rm V/cm}$), has large uncertainty and therefore almost no weight in determining the resonant frequency (as will be seen in Sec. 4.3 and Table 4.1).

3.3.2 Off-axis contribution to AC Stark shift

A complication arises from the fact that not all atoms travel collinearly with the experiment axis (the axis that passes through the centre of the tubes at the entrance and exit of each of the microwave regions). The off-axis atoms (1)

[33]York University, e-mail: amarsman@yorku.ca

experience different driving-field amplitude in the quench cavities, which results in incomplete quenching of the atoms in the $2S_{1/2}, f = 1$ state (although this effect is small); (2) experience a different profile of rf field amplitude in the FOSOF regions, which leads to slightly different AC Stark shifts; and (3) experience different (off-axis) components of rf electric field close to and inside the cylindrical tubes located before, in between, and after the waveguides, introducing a probability amplitude for driving $\Delta m_f = \pm 1$ transitions in the waveguides. The combined effect is complicated, since one has to consider not only the fields inside the waveguides, but also the rf fields in the quench cavities.

The simulations show that the change in the AC Stark shift for atoms away from the beam axis is proportional to r^2, where r is the distance that the atom is away from the experiment axis. For a beam of atoms, this shift ($\Delta_{\mathrm{AC}}^{(\mathrm{r})}$) can be written as

$$\Delta_{\mathrm{AC}}^{(\mathrm{r})} \propto r_{\mathrm{rms}}^2, \tag{3.9}$$

with

$$r_{\mathrm{rms}}^2 = R^2 + 2\pi \int_0^\infty (r')^3 \sigma(r')\, \mathrm{d}r', \tag{3.10}$$

and

$$\int \sigma(\vec{r'})\, \mathrm{d}A = 1, \tag{3.11}$$

where r_{rms} is the root-mean-squared distance of the atoms from the experiment axis, R is the overall radial shift of the centre of the beam from the beam axis, $\sigma(r)$ is the normalized area density of the atoms, assuming cylindrical symmetry in the beam, and r' is the distance from the centre of the beam. The value of r_{rms} was determined from a Monte-Carlo simulation, based on the geometry of the beam collimators. Assuming $R = 0$, this simulation indicates that r_{rms} for the start, middle, and end of the FOSOF regions is 1.62 mm, 1.70 mm, and 1.79 mm,

respectively. We therefore take as out best estimate of $r_{\rm rms}$:

$$r_{\rm rms} = \sqrt{\frac{1}{3}(1.62^2 + 1.70^2 + 1.79^2)} = 1.70\,{\rm mm}. \tag{3.12}$$

The changes $\Delta_{\rm AC}^{(r)}$ in the AC Stark shift due to $r_{\rm rms} = 1.70\,{\rm mm}$ are listed in the fifth column of Table 3.8.

For this Monte-Carlo simulation, an initial location of the atoms over the area of the end of the charge exchange cell (Fig. 2.4), and two angles determining the direction of the velocity vector, were chosen from a uniform probability distribution. Atoms in the simulation are initially placed right after the end of the charge-exchange region to account for possibility of scatterings inside the charge-exchange cell.

Alignment of vacuum components in the experiment is performed with the aid of an optical telescope and a set of small apertures. Alignment of the FOSOF waveguides is a challenge, because their axis (defined by the apertures for the atoms to pass through) was required to be aligned with the experiment axis for both the 0 and π configurations. This was achieved to better than 0.5 mm, giving $R = 0.0(5)\,{\rm mm}$.

Equation 3.12 suggests that the spreading of the beam within the waveguides is larger than the stated uncertainty for the value of R, and therefore it is not correct to use the uncertainty in the value of R as the uncertainty for r_{rms}. The other uncertainties are the uncertainties in the exact locations of each collimator (charge exchange exit (Fig. 2.4) and the aperture after the proton deflector (Fig. 2.5)) and the uncertainty as to whether the beam fills the collimators. We choose to adopt a relatively large 50% fractional uncertainty for all of the calculated frequency shifts due to non-zero beam diameter. The fifth column of Table 3.8 shows this 50% uncertainty for the off-axis corrections to the AC Stark shift.

3.3.3 Shift from the fractional offset in the quench curves

Another complication in determining the AC Stark shift comes from the offset in the quench curves (Sec. 2.5); i.e., the fact that the measured quench curves do not go to zero. This offset affects the power calibration procedure for the FOSOF waveguides (described in Sec. 2.9) since the simulated quench curves are mapped to the experimentally determined quench curves acquired for the FOSOF waveguides.

The best estimate for the fractional offset is 0.3% of the total population in the $2S_{1/2}$ state. The respective AC Stark shift corrections caused by including these offsets in the calibrations are listed in column six of Table 3.8. Similarly to the shift due to nonzero root-mean-squared radius of the beam, we introduce a 50-% fractional uncertainty to the corrections associated with the offset.

3.3.4 Uncertainty in the calculated AC Stark shifts

The 5% uncertainty assigned to the AC Stark shift corrections is estimated in the following way. Figure 4.2 shows a set of corrected linecenters determined for 18 sets of experimental parameters. These 18 linecenters exhibit excellent consistency. Each of the plotted linecenters includes statistical and systematic uncertainties added in quadrature. These uncertainties are shown in Table 4.1. If we include only the statistical uncertainty, σ_{stat}, then the weighted average of the linecenters has an unacceptably large reduced chi-squared of 3.4 with the probability of obtaining a larger value of chi-squared of only 0.0003%, as shown in Table 3.9. With the inclusion of the 50% fractional uncertainties in the corrections to the AC Stark shift due to the nonzero beam diameter, $\sigma_{\mathrm{AC}}^{(r)}$, and the fractional offset, $\sigma_{\mathrm{AC}}^{(\mathrm{offset})}$, in the quench curves, the reduced chi-squared is equal to 0.93, and the linecenters become consistent. Based on this, one can already state that, from the statistical point of

Table 3.9: Determination of the uncertainty in calculated AC Stark shifts. The first three columns are the experimental parameters. f_0 is the average resonant frequency (corrected for systematic shifts), and $\sigma_{\rm stat}$ is the statistical uncertainty in f_0 (these two columns are extracted from Table 4.1). $\sigma_{\rm AC}^{(r)}$ and $\sigma_{\rm AC}^{(\rm offset)}$ are the uncertainties in the AC Stark shifts corrections due to the non-zero $2S_{1/2}, f = 0$ atomic beam diameter and the fractional offset in the quench curves for the quench cavities (Table 3.8). $\sigma_{\rm AC}^{(5\%)}$ is the 5% fractional uncertainty assigned to all of the calculated AC Stark shifts ($\Delta_{\rm AC}$ in Table 3.8). $\sigma_{\rm stat+}r{\rm +offset} = \sqrt{\sigma_{\rm stat}^2 + (\sigma_{\rm AC}^{(r)})^2 + (\sigma_{\rm AC}^{(\rm offset)})^2}$, and $\sigma_{\rm stat+5\%} = \sqrt{\sigma_{\rm stat}^2 + (\sigma_{\rm AC}^{(5\%)})^2}$. We separately assign the uncertainties listed in the last three columns as the uncertainty in f_0 and calculate the weighted average of the linecenters for the three cases. The reduced chi-squared (χ_r^2) values for the weighted averages are shown in the last row.

D (cm)	$V_{\rm HV}$ (kV)	$E_0^{\rm rf}$ (V/cm)	f_0 (kHz)	$\sigma_{\rm AC}^{(r)}$ (kHz)	$\sigma_{\rm AC}^{(\rm offset)}$ (kHz)	$\sigma_{\rm AC}^{(5\%)}$ (kHz)	$\sigma_{\rm stat}$ (kHz)	$\sigma_{\rm stat+}r{\rm +offset}$ (kHz)	$\sigma_{\rm stat+5\%}$ (kHz)
4	16.27	14	909862.7	1.4	1.2	1.4	8.6	8.8	8.7
4	22.17	14	909870.2	0.6	1.3	1.6	3.9	4.1	4.2
4	49.86	5	909872.5	0.4	0.6	0.3	3.5	3.6	3.5
4	49.86	8	909875.8	0.7	0.9	0.7	2.0	2.3	2.1
4	49.86	14	909876.4	1.7	1.9	2.1	1.1	2.8	2.4
4	49.86	18	909870.4	2.6	2.9	3.8	0.8	4.0	3.8
4	49.86	24	909874.7	5.4	4.6	7.6	1.2	7.2	7.7
5	49.86	8	909872.4	1.3	0.2	0.5	4.6	4.8	4.7
5	49.86	14	909865.6	2.0	1.1	1.7	3.3	4.0	3.7
5	49.86	18	909865.0	2.7	1.9	3.1	2.5	4.2	4.0
5	49.86	24	909863.9	5.2	3.7	6.4	2.2	6.7	6.8
6	49.86	8	909868.6	1.0	0.1	0.4	8.7	8.7	8.7
6	49.86	14	909876.4	1.7	0.8	1.5	4.3	4.7	4.5
6	49.86	18	909871.6	2.3	1.5	2.6	3.7	4.6	4.5
6	49.86	24	909871.6	4.4	2.9	5.5	4.5	7.0	7.2
7	49.86	14	909874.9	0.8	1.2	1.3	5.9	6.1	6.1
7	49.86	18	909867.5	1.2	1.8	2.3	5.3	5.8	5.8
7	49.86	24	909869.1	3.5	3.0	4.9	4.8	6.7	6.9
					χ_r^2 of weighted average:		3.4	0.93	1.0

view, no additional uncertainty for the AC Stark shifts is needed. Nevertheless, if we assume that the calculated AC shifts had a 5% error, then including this error in quadrature with the statistical uncertainty (without including the uncertainties in the corrections to the AC Stark shift due to the nonzero beam diameter and the fractional offset in the quench curves) (listed in the last column of Table 3.9), changes the reduced chi-squared to 1.0, as desired.

To be conservative and to be independent of the accuracy of the simulations, we choose to include the 5% uncertainty for the calculated AC shifts.

3.4 Magnetic-field-induced shifts

A magnetic field component perpendicular to the velocity of an atom transforms into an electric field in the atom's reference frame, leading to a DC Stark shift of about $90\,\mathrm{kHz/G^2}$ for a 50-keV beam. The experiment is surrounded by two large mutually-perpendicular rectangular coils to cancel the transverse components of the stray magnetic fields to better than 30 mG in the FOSOF regions, yielding a shift of less than 0.1 kHz.

The component of the magnetic field parallel to the velocity of the atoms is not canceled out; it has a magnitude of less than 0.15 G. To first order, this axial component induces no Zeeman shift for the $2S_{1/2}f = 0$ and $2P_{1/2}f = 1, m_f = 0$ states; and the second-order correction is small enough to be ignored [35].

We conclude that the magnetic field has negligible effect on the resonant frequency, and this conclusion is supported by full density-matrix simulations of the experiment, including the magnetic field.

3.5 Shift due to stray electric fields

As was mentioned in Sec. 2.4, a DC electric field E would cause a shift of about $9.9\,\mathrm{kHz/(V/cm)^2}E^2$ (see Eq. 2.3 and footnote 11). In our experiment, stray DC electric field could be created by the accumulation of charge on insulating surfaces in the experiment region, containing the quench cavities and the FOSOF regions. The possibility for the presence of these fields was minimal, because the beam did not have a direct path to collide with the surfaces of the quench cavities or the FOSOF waveguides, due to a 4-mm circular aperture (shown in Fig. 2.5) placed before the pre-quench cavities. Also, the surfaces of the waveguides were periodically cleaned, and the experiment operated with oil-free pumps to minimize the presence of unintentional insulating surfaces in the experiment. Lastly, as was described in Sec. 3.2.2, linecenters measured with the proton deflector diverting protons and without the proton deflection were consistent: the difference between the two linecenters was equal to $0(7)\,\mathrm{kHz}$.

We conclude that the DC Stark shift associated with the stray electric fields in the FOSOF regions is insignificant at the level of the precision of the current measurement.

3.6 Residual population in the $2S_{1/2}f = 1$ states

So far we have assumed that the pre- and post-quench cavities removed all of the atomic population in the $2S_{1/2}f = 1$ state. In this section, frequency shifts associated with an incomplete removal of the $f = 1$ states are estimated.

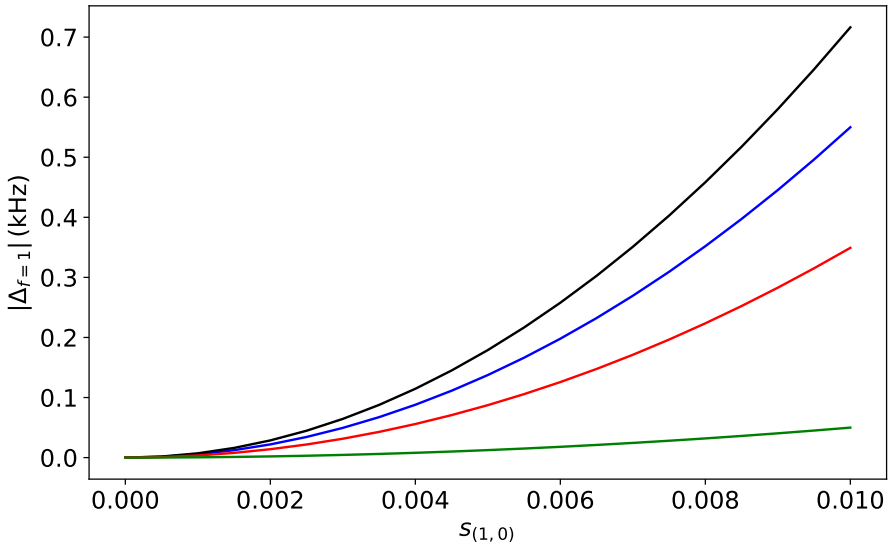

Figure 3.5: Estimated shifts from the residual population in the $2S_{1/2}f = 1$ state. The frequency shifts are calculated assuming square-field regions (i.e., the fields that turn on and off suddenly), with atoms moving at $0.01c$. The absolute values of the shifts are shown. Parameter $s_{(1,0)}$ is the probability of each of the $2S_{1/2}, f = 1, m_f$ sublevels to remain in its state after passing through the two sets of the quench cavities. The FOSOF driving-field amplitude is $E_0^{\mathrm{rf}} = 18\,\mathrm{V/cm}$. Each of the curves represents different separations between the fields D: the curves in blue, black, red, and green correspond to the waveguide separations of 4, 5, 6, and 7 cm, respectively.

3.6.1 Estimate of the frequency shift

The frequency shift due to imperfect quenching can be estimated with the following argument. The atomic current right after the proton deflector I is equal to

$$I = I^{2S}_{0,0} + I^{2S}_{1,1} + I^{2S}_{1,0} + I^{2S}_{1,-1}, \tag{3.13}$$

where I^{2S}_{f,m_f} stands for the current of the atoms in the hyperfine state with the f and m_f quantum numbers. After the set of the pre-quench cavities (Fig. 2.1), the atomic current, I', can be expressed as

$$I' = s_{(0,0)}I^{2S}_{0,0} + s_{(1,\pm1)}(I^{2S}_{1,1} + I^{2S}_{1,-1}) + s_{(1,0)}I^{2S}_{1,0}, \tag{3.14}$$

where $s_{(0,0)}$, $s_{(1,\pm1)}$, and $s_{(1,0)}$ are the fractional quenching-survival factors for the atoms in the $2S_{1/2}$ states with $f = 0, m_f = 0$, $f = 1, m_f = \pm1$, and $f = 1, m_f = 0$, respectively. Ideally, $s_{(1,\pm1)} = s_{(1,0)} = 0$. With the assumption that after the charge exchange the total atomic population is equally distributed among the four states, we can express the surviving population as

$$I' = \frac{1}{4} I s_{(0,0)} (1 + 2\frac{s_{(1,\pm1)}}{s_{(0,0)}} + \frac{s_{(1,0)}}{s_{(0,0)}}), \tag{3.15}$$

which means that fractionally, with respect to the surviving population in the $2S_{1/2} f = 0$ state, there are $2s_{(1,\pm1)}/s_{(0,0)}$ and $s_{(1,0)}/s_{(0,0)}$ atoms in the $f = 1, m_f = \pm1$ and $f = 1, m_f = 0$ states, respectively. The action of the post-quench cavity set is taken into account by simply squaring the respective surviving fraction factors. Setting, for simplicity, $s_{(1,0)}$=$s_{(1,\pm1)}$[34], and using $s_{(0,0)} = 0.26$ (see Sec. 2.5 and footnote 14), the frequency shifts for a square rf electric field profile in the FOSOF regions are plotted as the function of the quenching efficiency factor $s_{(1,0)}$ (which takes into account both sets of the quench cavities) in Fig. 3.5. These shifts are calculated by using Eq. 1.26, which is the expression for the probability, $P^{\mathrm{FOSOF}}_{\Delta\omega t}$, of an atom starting in some state to remain in the same state after passing through two FOSOF regions. In particular, if we have an atom which is in a mixture of the $2S_{1/2}, f = 0$ and $2S_{1/2}, f = 1$ states, and the probability for the atom to be in the $2S_{1/2}, f = 1, m_f = 0$ state or the $2S_{1/2}.f = 1, m_f = \pm1$ state is $s_{(0,0)}/s_{(1,0)}$ times smaller than for the atom to be found in the $2S_{1/2}, f = 0$ state, then the total probability, $P^{\mathrm{FOSOF}}_{\Delta\omega t}[\mathrm{tot}]$, to detect the atom in the $2S_{1/2}$ state after the two FOSOF regions with a square

[34]The assumption is that all of the cavities are equally efficient at quenching atoms in respective m_f sublevels.

profile of the electric fields is

$$
\begin{aligned}
P_{\Delta\omega t}^{\mathrm{FOSOF}}[\mathrm{tot}] = {} & P_{\Delta\omega t}^{\mathrm{FOSOF}}[2S_{1/2}, f=0 \rightarrow 2P_{1/2}, f=1, m_f=0] \\
& + 2\frac{s_{(1,\pm 1)}}{s_{(0,0)}} P_{\Delta\omega t}^{\mathrm{FOSOF}}[2S_{1/2}, f=1, m_f=\pm 1 \rightarrow 2P_{1/2}, f=1, m_f=\pm=1] \\
& + \frac{s_{(1,0)}}{s_{(0,0)}} P_{\Delta\omega t}^{\mathrm{FOSOF}}[2S_{1/2}, f=1, m_f=0 \rightarrow 2P_{1/2}, f=0].
\end{aligned} \tag{3.16}
$$

According to Eq. 1.26, the expression for the total probability in Eq. 3.16 can be written as

$$
P_{\Delta\omega t}^{\mathrm{FOSOF}}[\mathrm{tot}] = P_{\mathrm{tot}}^{(0)} + A_{\mathrm{tot}} \cos(\theta_{\mathrm{tot}} + \Delta\omega t + \phi_2 - \phi_1), \tag{3.17}
$$

where A_{tot} is the FOSOF amplitude, $\Delta\omega$ is the frequency offset between the frequencies of the rf fields in the FOSOF regions, $\phi_2 - \phi_1$ is the phase difference between the rf fields, $P_{\mathrm{tot}}^{(0)}$ is a term independent of ϕ_1 and ϕ_2, and θ_{tot} is the FOSOF phase. For a given value of $s_{(1,0)}$, the simulated FOSOF lineshape (the FOSOF phase as a function of the frequency of the rf fields in the FOSOF regions) is fit to a straight line, and the zero-phase-crossing frequency, $f_{zc}(s_{(1,0)})$, is determined. The frequency shift (plotted in Fig. 3.5) is equal to $f_{zc}(s_{(1,0)}) - f_{zc}(0)$, where $f_{zc}(0)$ is the zero-phase-crossing frequency determined when all of the $2S_{1/2}, f=1$ population is quenched by the quench cavities (i.e., $s_{(1,0)} = 0$).

There are several effects that influence the efficiency of the removal of the population in the $2S_{1/2}, f = 1$ state, represented by the factor $s_{(1,0)}$, which are described below.

3.6.2 Uncertainty in determination of the rf powers required to drive π pulses in the quench cavities

For a particular quench cavity, the power required to drive a π pulse is determined by locating the rf power for which the surviving fraction is minimum. Therefore, the rf power corresponding to the π pulse is subject to a statistical noise in the

data, and a particular method for extracting the minimum. From quench curves, it is calculated that in order to produce a 0.005 change in the quenching efficiency, the voltage applied to voltage-controlled attenuators[35] needs to be changed by at least 0.1 V, which is much larger than the statistical uncertainty in the location of the π pulse[36]; the exact method used to determine its location is irrelevant at this level. For $s_{(1,0)} = 0.005$ the shift is at most 0.4 kHz (see Fig. 3.5), and it can be ignored.

3.6.3 Variation in the beam speed

The speed of the atoms is not constant for the same nominal accelerating voltage V_{HV}, since it depends on the exact value of the probe voltage in the proton source (see Sec. 2.2). This voltage is periodically tuned to optimize the quality of the FOSOF signal measured in the Lyman-α detector, thus causing π pulses to shift slightly. The change in surviving fraction $s_{(1,0)}$ for a small change in accelerating voltage ΔV is estimated by considering Rabi oscillations in a constant-amplitude field, omitting spontaneous decay for simplicity:

$$\Delta V^2 \approx V^2 \frac{4}{\pi^2} s_{(1,0)}, \tag{3.18}$$

where V is the accelerating voltage for which the π pulse is determined. If at a typical accelerating voltage of about $V = 52\,\mathrm{kV}$ all of the $2S_{1/2}, f = 1$ population was quenched by the two sets of the quench cavities ($s_{(1,0)} = 0$), then a change in the accelerating voltage of 2 kV will change the surviving fraction of the $2S_{1/2}, f = 1$ population to about $s_{(1,0)} = 0.005$, leading to a frequency shift of about 0.4 kHz for an rf field amplitude in the FOSOF regions of $E_0^{\mathrm{rf}} = 18\,\mathrm{V/cm}$. Typically, the

[35] This is how the input power for the quench cavities is controlled; see Fig. 2.7.

[36] The statistical uncertainty is calculated by acquiring several quench curves for the same quench cavity, and calculating the spread in the extracted π pulses.

probe voltage is varied by a fraction of a kilovolt. For the nominal accelerating voltages of 16.27 and 22.17 kV and for $s_{(1,0)} = 0.005$, the shifts are 0.17 and 0.2 kHz respectively for $E_0^{\rm rf} = 14\,{\rm V/cm}$. This corresponds to a change in the probe voltage of 0.9 kV for $V_{\rm HV} = 16.27\,{\rm kV}$ and 1.0 kV for $V_{\rm HV} = 22.17\,{\rm kV}$. For the FOSOF data acquired at these two accelerating voltages, the probe voltage was changed by much less than 0.9 kV. Therefore, the variation in the beam speed has negligible effect on the resonant frequency.

3.6.4 Hyperfine-state selection and the beam radius

As mentioned in Sec. 3.3.2, the rf powers to drive π pulses in the quench cavities depend on the metastable-beam diameter. This effect is already incorporated into the simulations, as discussed in Sec. 3.3.2, and therefore it is a part of correction $\Delta_{\rm AC}^{(r)}$ in Table 3.8.

3.6.5 Shift due to the $f = 1$ state from experimental data

So far we have shown that according to our estimates, residual population in the $2S_{1/2}, f = 1$ state after the two sets of the quench cavities has insignificant effect on the resonant frequency that we determine from FOSOF lineshapes. We can also estimate the shift due to the $2S_{1/2}, f = 1$ state from the data acquired with the 910-MHz pre-quench cavity quenching a fraction of the $2S_{1/2}, f = 0$ state. Such an experiment was discussed in Sec. 3.2.1. The expression to estimate the shift, $\Delta_{f=1}$, due to $2S_{1/2}, f = 1$ state has the same functional form as in Eq. 3.3:

$$\Delta_{f=1} \approx -\frac{1}{(\alpha_{f=1} - 1)S}\langle\Delta\phi\rangle, \tag{3.19}$$

however, the factor by which the population in the $2S_{1/2}, f = 0$ state is reduced, α, in Eq. 3.3 is replaced by $\alpha_{f=1}$, which takes into account that, unlike the high-n

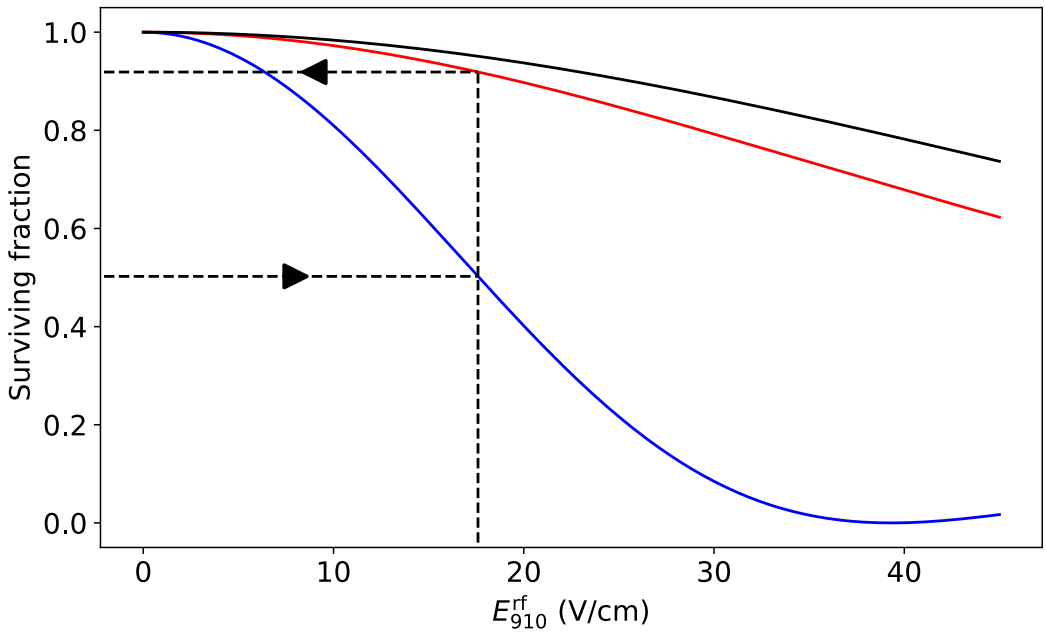

Figure 3.6: Residual population in the $2S_{1/2}$ state after passing through the 910-MHz pre-quench cavity as a function of the rf field amplitude E_{910}^{rf} in the cavity. The transitions driven in the pre-quench cavity are indicated in Fig. 2.2. Surviving fractions for the atoms in the $2S_{1/2}, f = 0$, $2S_{1/2}, f = 1, m_f = \pm 1$, and $2S_{1/2}, f = 1, m_f = 0$ states are shown in blue, red, and black, respectively. The surviving fractions are calculated assuming square profile of the rf field in the cavity, and the speed of the atoms is set to $0.01c$. The atoms in the $2S_{1/2}, f = 1, m_f = \pm 1$ have a smaller surviving fraction as a function of the rf field amplitude, compared to the atoms in the $2S_{1/2}, f = 1, m_f = 0$ state. Dashed lines and arrows show the procedure for determining the surviving fraction of the $2S_{1/2}, f = 1, m_f = \pm 1$ population, $P_{f=1}$. Given the surviving fraction of the $2S_{1/2}, f = 0$ state, the corresponding rf field amplitude is first determined. This amplitude is then used to calculate $P_{f=1}$.

Table 3.10: Estimated frequency shifts due to the residual population in the $2S_{1/2}, f = 1$ state. The shifts are determined from the data (Table 3.5) that was used to estimate frequency shifts due to possible presence of $n > 2$ states by toggling the rf power in the 910-MHz pre-quench cavity (Sec. 3.2.1). The first five columns are taken from Table 3.5. The first three columns are experimental parameters: the separation between the FOSOF regions D, the rf field amplitude in the FOSOF regions E_0^{rf}, and the pressure in the charge-exchange region P_{CGX}. α is the factor by which the $2S_{1/2}, f = 0$ population is reduced due the rf power in the 910-MHz pre-quench cavity. $\langle\Delta\phi\rangle$ is the average FOSOF phase difference between the cases of the 910 quench on and off. The procedure to determine the surviving fractions of the $2S_{1/2}, f = 1$ state, $P_{f=1}$, is described in Sec. 3.6.5. Values of $\alpha_{f=1}$ are calculated using Eq. 3.20. Estimated frequency shifts $\Delta_{f=1}^{(\mathrm{exp})}$ are determined using Eq. 3.19.

D (cm)	E_0^{rf} (V/cm)	P_{CGX} (μTorr)	α	$\langle\Delta\phi\rangle$(mrad)	$P_{f=1}$	$\alpha_{f=1}$	$\Delta_{f=1}^{(\mathrm{exp})}$(kHz)
4	8	1.6	13.5	0.8(8)	0.79	10.6	−0.9(9)
4	18	0.2	13.3	−0.3(5)	0.79	10.5	0.3(5)
4	18	1.6	13.2	0.44(23)	0.79	10.4	−0.48(25)
4	18	3.3	13.3	0.1(4)	0.79	10.5	−0.1(5)
4	18	6.2	13.3	−0.6(4)	0.79	10.5	0.7(5)
5	18	1.6	3.8	−0.3(5)	0.86	3.3	1.3(20)
6	18	0.2	3.8	0.2(14)	0.86	3.3	−1(4)
6	18	1.6	3.8	3.3(27)	0.86	3.3	−11(9)
6	18	3.3	3.8	1.9(13)	0.86	3.3	−6(4)
6	18	6.2	3.8	−0.2(13)	0.86	3.3	1(4)
7	24	1.6	2.0	0.5(12)	0.92	1.8	−4(9)

Table 3.11: Estimated shifts due to the $2S_{1/2}, f = 1$ state. The first three columns are experimental parameters. Normalized slopes (S) are obtained from linear fits to FOSOF data. Normalized ratios of FOSOF amplitudes of the $2S_{1/2}, f = 0$ and $2S_{1/2}, f = 1$ states ($A_{f=1}$) are calculated assuming square profile of the rf fields in the FOSOF regions. The shifts due to the residual population in the $2S_{1/2}, f = 1$ state ($\Delta_{f=1}$) are listed in the last column. For these shifts, the uncertainties are correlated, since they are derived from the same data. The last row lists the weighted average of the shifts, which is calculated by following the same procedure as in Sec. 4.3, using the same weights as in Sec. 4.1.

D (cm)	V_{HV} (kV)	E_0^{rf} (V/cm)	S	$A_{f=1}$	$\Delta_{f=1}$(kHz)
4	16.27	14	0.64	1.2	−0.1(1)
4	22.17	14	0.64	1.1	−0.1(1)
4	49.86	5	0.55	1.0	−0.2(2)
4	49.86	8	0.56	1.0	−0.2(2)
4	49.86	14	0.58	1.0	−0.2(2)
4	49.86	18	0.59	1.0	−0.2(2)
4	49.86	24	0.67	1.0	−0.1(2)
5	49.86	8	0.67	1.0	−0.1(2)
5	49.86	14	0.68	1.0	−0.1(2)
5	49.86	18	0.71	1.0	−0.1(2)
5	49.86	24	0.77	1.0	−0.1(1)
6	49.86	8	0.79	1.0	−0.1(1)
6	49.86	14	0.81	1.0	−0.1(1)
6	49.86	18	0.82	1.0	−0.1(1)
6	49.86	24	0.90	1.0	−0.1(1)
7	49.86	14	0.92	1.0	−0.1(1)
7	49.86	18	0.95	1.0	−0.1(1)
7	49.86	24	1.00	1.0	−0.1(1)
			Weighted average:		−0.13(15)

states, the $2S_{1/2}, f = 1$ population is reduced by the rf fields in the 910-MHz pre-quench cavity. Therefore,

$$\alpha_{f=1} = \alpha P_{f=1}, \tag{3.20}$$

where $P_{f=1}$ is the probability for the atom in the $2S_{1/2}, f = 1$ state to remain in this state after passing through the 910-MHz pre-quench cavity with an rf field amplitude of $E^{\rm rf}_{910}$. Calculated values of $P_{f=1}$ as a function of $E^{\rm rf}_{910}$ are plotted in Fig. 3.6, where we make the simplifying assumption that the 910-MHz pre-quench cavity has a square profile of the rf fields. The $\Delta m_f = 0$ transitions driven in the cavity are labeled in Fig. 2.2. As indicated in Fig 3.6, out of the atoms in the $2S_{1/2}, f = 1$ state, the rf field of the cavity quenches more of the atoms in states with $m_f = \pm 1$, which we take as our estimate of $P_{f=1}$. Column 7 of Table 3.10 lists values for $\alpha_{f=1}$ calculated using values for α (column 4) and $P_{f=1}$ (column 6), and shifts due to atoms in the $2S_{1/2}$ state are listed in the last column.

Similarly to the discussion in Sec. 3.2.4, it is expected that the shift due to the $2S_{1/2}, f = 1$ state is proportional to the inverse of the FOSOF slope S and the ratio of the FOSOF amplitude due to the atoms in the $2S_{1/2}, f = 1$ state to the FOSOF amplitude due to the atoms in the $2S1/2, f = 0$ state. This ratio is denoted by $A_{f=1}$. Therefore, assuming a square profile of the rf fields in the FOSOF regions, we can scale the shifts $\Delta^{(\rm exp)}_{f=1}$ listed in the last column of Table 3.10 to the same set of experimental parameters. We choose to scale the shifts to a waveguide separation of $D = 7\,\text{cm}$, a nominal accelerating voltage of $V_{\rm HV} = 49.86\,\text{kV}$, and an rf field amplitude of $E^{\rm rf}_0 = 24\,\text{V/cm}$. We use the weighted average of these scaled shifts to calculate the expected shift for other 17 sets of experimental parameters. The shifts are listed in the last column of Table 3.11. Finally, these 18 shifts are included into the final statistical analysis that is described in Sec. 4.3. Using the same weights as in Table 4.1, the estimated shifts due to the $2S_{1/2}, f = 1$ state are averaged, and

the weighted average is shown in the last row of Table 3.11. The overall shift due to the residual $2S_{1/2}, f = 1$ population is estimated to be

$$\Delta_{f=1} = -0.13(15)\,\text{kHz}. \tag{3.21}$$

The shift in Eq. 3.21 is consistent with zero. Compared to the final uncertainty for our measurement of 3.2 kHz, this shift is small. We choose to omit this correction because it is negligible and consistent with zero.

3.7 First-order Doppler shift

The first-order Doppler shift is zero under the assumption that the losses in the waveguides are negligible, and therefore there is no traveling-wave component inside the FOSOF regions. That is, if there are no losses, then an equal intensity wave is traveling in the upward direction as in the downward direction, and these together form a standing wave. In this section, we estimate the frequency shift due to finite conductivity of aluminum – the metal out of which the FOSOF waveguides are machined.

3.7.1 Calculation of the field attenuation

For a rectangular waveguide of dimension a time b and of infinite length with a single propagating TE_{10} mode, the resistivity of the conductor causes ohmic losses. The amplitude of the electric field along the direction of propagation, defined by z axis, is [36]

$$E(z) = E_0 e^{-\alpha_c z}, \tag{3.22}$$

where the attenuation constant, α_c is

$$\alpha_c = \frac{R_s}{\eta b} \frac{1 + \frac{2b}{a}\frac{\omega_c^2}{\omega^2}}{\sqrt{1 - \frac{\omega_c^2}{\omega^2}}}, \tag{3.23}$$

where η is the impedance of free space, $\omega_c = c\dfrac{\pi}{a}$ is the cut-off frequency of the waveguide, c is the speed of light in vacuum, $\omega = 2\pi f = 2\pi \times 910\,\mathrm{MHz}$ is the angular frequency of the propagating wave. The expression for the surface resistance R_s is

$$R_s = \frac{1}{\sigma_c \delta}, \tag{3.24}$$

and the skin depth is

$$\delta = \frac{1}{\sqrt{\pi f \mu_0 \sigma_c}}, \tag{3.25}$$

where, $\sigma_c \approx 2 \times 10^{-7}/\Omega\,\mathrm{m}$ is the conductivity of the material, and μ_0 is the permeability of free space. In our case, the wave travels through the waveguide twice (on the way up and then again on the way down). Referring to Fig. 2.9, we have $a = 23\,\mathrm{cm}$, $b = 3\,\mathrm{cm}$, and $z \approx 1\,\mathrm{m}$. Using the equations above, the attenuation constant is approximately $\alpha_c = 2 \times 10^{-3}/\mathrm{m}$.

This calculation does not take into account currents on the surface of the waveguide short (labeled in Fig. 2.9), and also it omits the apertures in the waveguide through which the atoms pass through – locations where the current density is larger. For a standing wave, there are also localizations of maxima and minima of current density along the surfaces of the conductor, where the power losses are at their local maximum and minimum, respectively. To include these effects, we simply assume that the power losses could be as much as a factor of 10 larger. Using Eq. 3.22, the electric-field amplitude of the wave, reflected off the short in the waveguide, could be up to 1.9% smaller than the amplitude of the incident wave. The electric field along the experimental axis is then the sum of

the standing wave and the traveling wave with the amplitude of E_0 and κE_0, respectively, where $\kappa < 1.9 \times 10^{-2}$.

3.7.2 First-order Doppler effect. Calculation of the frequency shift

The first-order Doppler shift arises when the wave vector of the traveling wave in the waveguides is not normal to the velocity of the atoms. As shown in Fig. 3.7, there are two ways for this to happen: when the rotation axis of the rotary stage (blue line on the figure), on which the waveguides rest, is not normal to the experiment axis (this angular deviation is indicated by $\Delta\phi_{\text{tilt}}$ on the figure) or when the velocity of the atoms is not parallel to the experiment axis (indicated by $\Delta\phi_{\text{dev}}$ on the figure). From the experiment geometry, the maximum angular deviation of atoms' velocity $\vec{v}$ from the experiment axis is $\Delta\phi_{\text{dev}} = 4.4\,\text{mrad}$ (determined by the 4.8-mm exit aperture of the charge-exchange cell and the 4.0-mm aperture of the cylindrical Faraday cup after the proton deflector for collecting the deflected protons, separated by 99.1 cm). This estimate is extremely conservative, as it would assume that all atoms start at the bottom of the charge-exchange-cell exit and pass through the top of the 4-mm collimator (or vice versa). Perpendicularity of the rotation axis of the rotary stage to the experiment axis is determined using a surveyor's telescope; the maximum tilt angle is less than $\Delta\phi_{\text{tilt}} = 1.5\,\text{mrad}$. The deviation of the angle between the velocity of the atoms and the wave vector of the traveling wave in the waveguides is $\sigma_{\phi_{\text{tot}}} = \sqrt{4.4^2 + 1.5^2} = 4.6\,\text{mrad}$. In the atoms' reference frame, the frequency of the small-amplitude traveling wave experiences a first-order Doppler shift of[37]

$$\Delta f_\kappa = \sin(\sigma_{\phi_{\text{tot}}})\frac{v}{c} f = \pm 42\,\text{kHz}, \tag{3.26}$$

[37]The second-order Doppler shift is the same for both the traveling and standing waves.

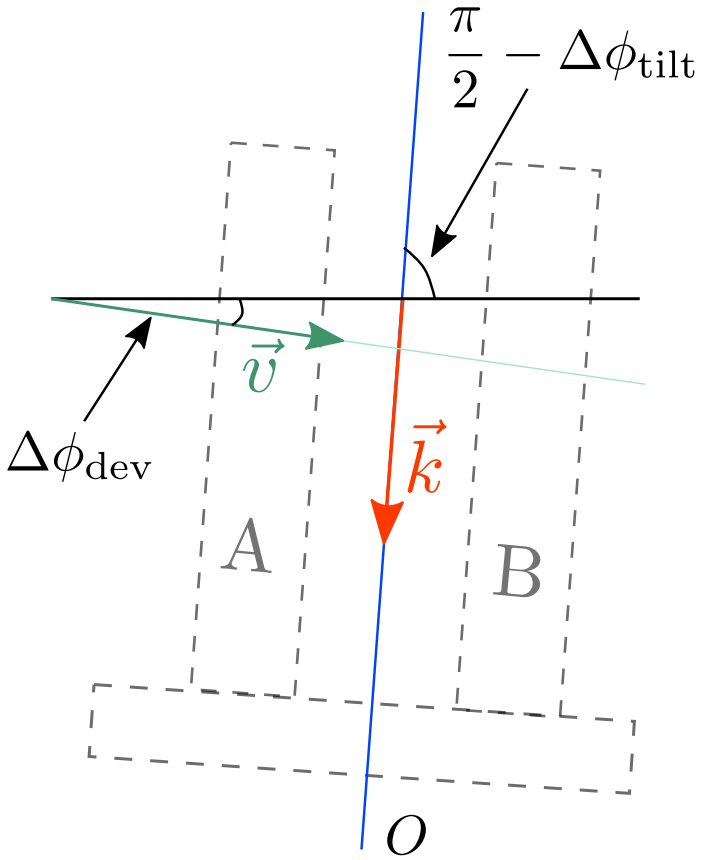

Figure 3.7: Origin of the first-order Doppler shift. The axis of rotation of the waveguides O is not normal to the experiment axis (shown as a solid line in black), but is tilted at angle $\frac{\pi}{2} - \sigma_{\phi_{\text{tilt}}}$. The wave vector $\vec{k}$ of the traveling wave is parallel to axis O. Waveguides A and B, and the rotary stage on which the waveguides are resting are schematically shown with dashed lines. The angle between velocity of the atoms $\vec{v}$ and the experiment axis is $\sigma_{\phi_{\text{dev}}}$. Depending on the relative orientation of $\vec{v}$ and $\vec{k}$, the angle between these two vectors, ϕ_{tot}, varies from $\frac{\pi}{2} - |\sigma_{\phi_{\text{tilt}}} + \sigma_{\phi_{\text{dev}}}|$ to $\frac{\pi}{2} - |\sigma_{\phi_{\text{tilt}}} - \sigma_{\phi_{\text{dev}}}|$ with a mean of $\langle\phi_{\text{tot}}\rangle = \pi/2$ and a standard deviation of $\sigma_{\phi_{\text{tot}}} = \sqrt{\sigma^2_{\phi_{\text{tilt}}} + \sigma^2_{\phi_{\text{dev}}}}$.

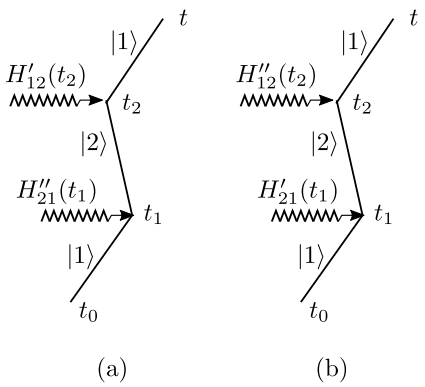

Figure 3.8: Probability amplitudes for the Doppler-shifted traveling wave. Fig. A.1 shows the probability amplitudes from the interaction with the standing wave of amplitude E_0, $1/\kappa$ times larger than that of the traveling wave. $H''(t)$ is equal to $W^{(\mathrm{RWA})'}(t)$ (Eq. 3.27). An atom can interact with the traveling wave in the first FOSOF region (H''_{21}), and then with the standing wave (H'_{12}) in the second region (a). Another possibility (b) is for the particle to first interact with the standing wave (H'_{21}), and then to transition back to the state $|2\rangle$ via interaction with the traveling wave (H''_{12}). The diagrams follow the style of [37].

where $\frac{v}{c} \approx 0.01$ is the ratio of the speed of the atoms to the speed of light, and $f \approx 910\,\mathrm{MHz}$ is the rf frequency of the traveling wave.

The Hamiltonian in the rotating-wave approximation for the combined standing wave and traveling wave is

$$H = H_0 + W^{(\mathrm{RWA})}(t) + W^{(\mathrm{RWA})'}(t), \tag{3.27}$$

with H_0 and $W^{(\mathrm{RWA})}(t)$ given by Eq. 1.4 and 1.10, respectively. $W^{(\mathrm{RWA})'}(t)$ is the Hamiltonian due to the traveling wave. It is identical to that of the standing wave, given by $W^{(\mathrm{RWA})}(t)$, except the frequency ω is changed to $\omega + \Delta\omega_\kappa$, where $\Delta\omega_\kappa = 2\pi\Delta f_\kappa$ is given in Eq. 3.26:

$$W^{(\mathrm{RWA})'}(t) = \kappa\frac{1}{2}E_0 p_z \begin{pmatrix} 0 & e^{-i((\omega+\Delta\omega_\kappa)t+\phi_i)} \\ e^{i((\omega+\Delta\omega_\kappa)t+\phi_i)} & 0 \end{pmatrix}, \tag{3.28}$$

In second-order time-dependent perturbation theory, in addition to the two

probability amplitudes – the first amplitude is for an atom to traverse the FOSOF regions while remaining in the $2S_{1/2}, f = 0$ state, and the second amplitude is for an atom to transition to the $2P_{1/2}, f = 1, m_f = 0$ state in the first FOSOF region and then transition back to the $2S_{1/2}, f = 0$ state in the second FOSOF region (described in Appendix A) – there are now two extra probability amplitudes visualized in Fig. 3.8. The probability term, $P^{(\mathrm{int})(\kappa)}_{|1\rangle\to|1\rangle}$, describing the interference between these two paths and the zeroth-order path is

$$P^{(\mathrm{int})(\kappa)}_{|1\rangle\to|1\rangle} = 2\kappa A_\kappa \cos((\Omega + \frac{\Delta\omega_\kappa}{2})(T+\tau) + \delta\phi), \tag{3.29}$$

with

$$A_\kappa = -2\frac{E_0^2|p_z|^2}{\hbar^2}\frac{\sin(\Omega\tau/2)}{\Omega}\frac{\sin(\Omega_\kappa\tau/2)}{\Omega_\kappa}\cos(\frac{\Delta\omega_\kappa(T+2\tau)}{2}); \tag{3.30}$$

$$\Omega_\kappa = \Omega + \Delta\omega_\kappa. \tag{3.31}$$

Comparison with Eq. A.1 reveals that the detuning Ω, is shifted by the amount $\Delta\omega_\kappa/2$. The contribution to the total probability from the interference of the probability amplitudes is

$$P^{(\mathrm{int})}_{|1\rangle\to|1\rangle} + P^{(\mathrm{int})(\kappa)}_{|1\rangle\to|1\rangle}, \tag{3.32}$$

where the form of $P^{(\mathrm{int})}_{|1\rangle\to|1\rangle}$ is given by Eq. A.1. By setting $A_\kappa \approx A$, the frequency difference Δ_κ between the frequency determined with the FOSOF technique and the true resonant frequency could be as large as

$$\Delta_\kappa = k\Delta f_\kappa = \pm 0.8\,\mathrm{kHz}, \tag{3.33}$$

where the sign of the shift depends on the sign of the first-order Doppler shift Δf_k. In other words, the frequency shift due to the first-order Doppler shift is estimated to be $0.0(8)\,\mathrm{kHz}$.

The FOSOF lineshapes acquired for both the 0 and π configurations have the first-order Doppler shifts of the same sign. Therefore, waveguide reversal does not

negate this effect. However, our estimate is very conservative. This calculation assumes that all of the atoms are perfectly focused and are maximally deviant from the experiment axis. Actually, by placing a glass plate at the end of the experiment beam line and detecting the fluorescence with a CCD camera, we confirm that the atomic beam is not focused, and has a diameter much larger than the circular aperture in the copper cup after the proton deflector for collecting protons (shown in Fig. 2.5). Hence, the angular deviation of atoms' velocity $\vec{v}$ from the experiment axis is at least a factor of four smaller: $\Delta\phi_{\rm dev} \approx 1\,{\rm mrad}$, leading to a more realistic frequency shift that could be as large as

$$\Delta_\kappa = k\Delta f_\kappa = \pm 0.3\,{\rm kHz}, \tag{3.34}$$

leading to the first-order Doppler shift of $0.0(3)\,{\rm kHz}$. This shift is consistent with zero and its uncertainty is one tenth of the total uncertainty ($3.2\,{\rm kHz}$) for the current measurement. Even the $0.3\,{\rm kHz}$ possible shift is very likely an overestimate since we have very conservatively multiplied the attenuation factor of the waveguides by 10 in order to account for the short and the tubes. We conclude that the first-order Doppler shift that arises due to finite electrical conductivity of the walls of the waveguides leads to a negligible effect on the resonant frequency.

3.8 Imperfect control of the radio-frequency system

As discussed in Sec. 2.8, the reversal of the waveguides eliminates the effects of phase shifts caused by rf propagation delays. This cancellation is based on the assumption that none of the rf components are disturbed in the process of the reversal.

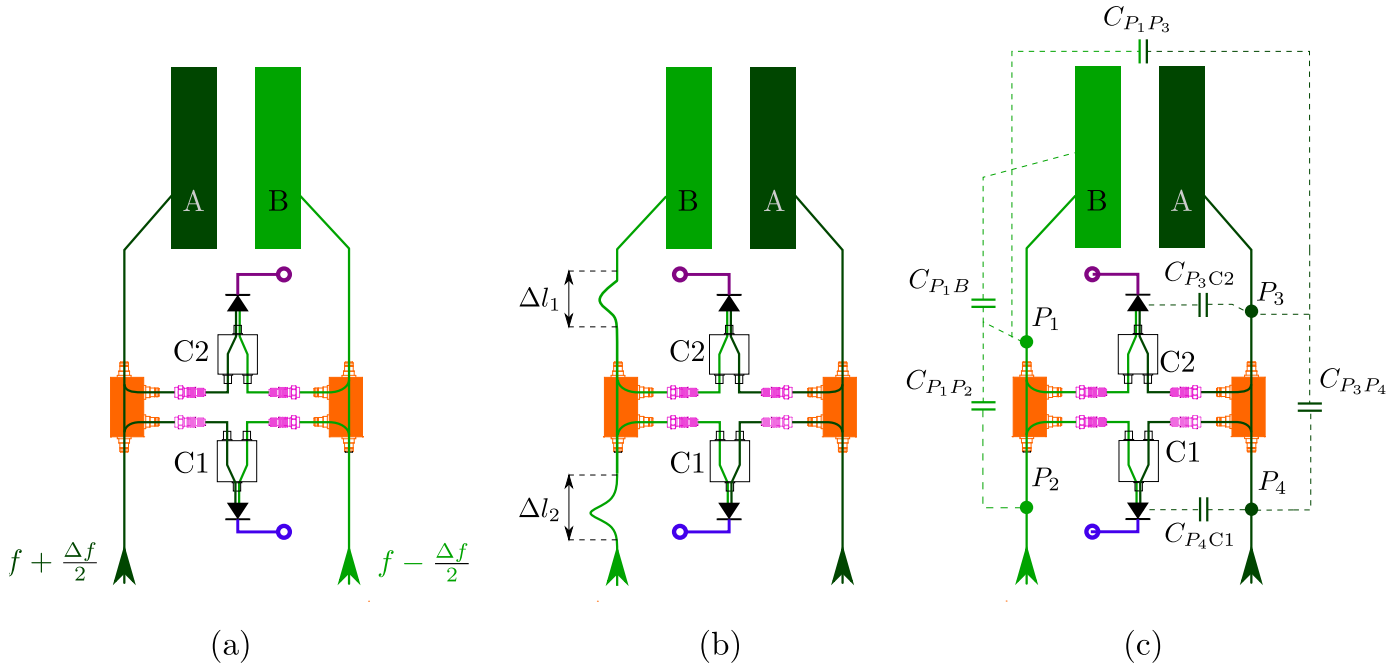

Figure 3.9: Hypothetical examples of changes in the rf system that one could imagine occurring as a result of the rotation of the rf system (i.e., changing between 0 and π configurations). Initially the waveguides are in the 0 configuration (a). The left and right arms of the rf system are driven at frequencies of $f + \frac{\Delta f}{2}$, and $f - \frac{\Delta f}{2}$, respectively. The phase difference between the beatnote signals from combiners C1 and C2 is monitored. In (b) and (c), the rf system is reversed (the waveguides are in the π configuration). In (b), the length of cables above and below the bi-directional coupler for the left rf arm is increased by Δl_1 and Δl_2, respectively. In (c), the physical length of the cables remains the same, however, it is assumed that the rf system is not completely isolated from the environment outside of the rf system. In particular, as an example, there is some leakage of the rf power from the points P_1 to P_4, and from the diodes connected to combiners C1 and C2. This capacitive coupling between various parts of the rf system is represented by C_{ij}, where i and j stand for the points/components between which there is the coupling.

3.8.1 Detection of the changes in the rf phase under the reversal

Examples of hypothetical situations for which the reversal of the rf system does not negate rf-related phase offsets are shown in Fig. 3.9. Part (b) of the figure illustrates a simple example in which the reversal of the system causes a mechanical effect: the cables before and after the bi-directional coupler for the left rf arm are stretched. Only the change in the length of the cable after the bi-directional coupler Δl_1 matters for FOSOF, since the phase of the fields in waveguide B and in the combiners will change by the same amount. Compared to part (a) of the figure, the phase difference between the beatnotes from combiners C1 and C2, $\phi^{C2}_{\rm beat} - \phi^{C1}_{\rm beat}$, is changed by

$$\begin{aligned}(\phi^{C2}_{\rm beat} - \phi^{C1}_{\rm beat})^{(\pi)} - (\phi^{C2}_{\rm beat} - \phi^{C1}_{\rm beat})^{(0)} &= 2\frac{2\pi}{\lambda}\Delta l_1 \qquad (3.35)\\ = -2((\phi_2 - \phi_1 - \phi^{C2}_{\rm beat})^{(\pi)} - (\phi_2 - \phi_1 - \phi^{C2}_{\rm beat})^{(0)})&\\ = 2((\phi_2 - \phi_1 - \phi^{C1}_{\rm beat})^{(\pi)} - (\phi_2 - \phi_1 - \phi^{C1}_{\rm beat})^{(0)}),&\end{aligned}$$

where λ is the wavelength of the radio-frequency, $\phi_2 - \phi_1$ is the phase difference between the rf fields in the two FOSOF regions. Therefore, the change in the path-length differences in the rf system can be detected by monitoring the phase difference between the combiners for both orientations of the waveguides.

Part (c) of Fig. 3.9 illustrates a more complicated example. The system is assumed to have some leakage of the rf power from one part of the rf system to another. This can happen if, for instance, braided shielding on some of the interconnecting coaxial cables is damaged, and their shielding factor is reduced. One could imagine that this coupling could potentially change when rotating between the 0 and π configurations if the mutual capacitances that lead to this coupling would depend on the orientations of the waveguides. If this is the case for the capacitances, for example, between P_1 and P_2, P_3 and P_4, P_1 and P_3, then the

change in the coupling can be detected in the same way as for the case of the physical path-length change – by monitoring the phase difference between the combiners for both orientations of the waveguides. The shift in the zero-phase crossing frequency due to such a coupling can be determined by looking at the difference of the zero-phase-crossing frequencies obtained from the beatnote signal from C1 and C2.

The average difference of the zero-phase-crossing frequencies for all of the data sets is calculated to be only 0.16 kHz. That is, the final result of our measurement changes by less than 0.2 kHz when C1 is used to determine the beatnote phase as compared to C2. Therefore, at the level of the precision of the experiment, there is no systematic change in the rf system under the reversal of the types described above.

3.8.2 Common shift in the phase difference between the combiners

Consider, however, a situation when there is a coupling between the diodes for the combiners, and the points P_3 and P_4, as indicated on part (c) of Fig. 3.9, by the capacitances $C_{P_3\mathrm{C2}}$ and $C_{P_4\mathrm{C1}}$. In this case, if we also make the unlikely assumption that $C_{P_3\mathrm{C2}}$ or $C_{P_4\mathrm{C1}}$ vary as we rotate the system between 0 and π, it could be possible to measure no significant phase difference change between the beatnotes from the combiners under the reversal, but to have changes in the phase difference between the fields in the waveguides and the combiners.

This type of coupling is a concern, because when we started monitoring the phase difference between combiners C1 and C2, we discovered that this phase difference could be changed by milliradians by simply positioning a metal foil near the rf system. We could also detect the leaking rf signal on a simple multiple-loop antenna, indicating that there was a leakage of the rf power from the system. Considerable effort was put into minimizing the coupling between the rf system

and the outside environment to the point when no abrupt change in the phase difference between the signals from the combiners could be detected when the waveguides were rotated, or the boundary conditions outside the rf system were changed. But, unfortunately, we were not successful at understanding the exact cause of the coupling.

3.8.3 Variation of the zero-phase-crossing frequency with the FOSOF slope

In the previous section, we presented an example of a coupling between the left and right arms of the rf system for the FOSOF regions. If this rf coupling is different between the 0 and π configurations, then it will not be detected in the phase difference between the beatnotes from combiners C1 and C2, but it will introduce a phase shift of $\phi_c^{(0)}$ and $\phi_c^{(\pi)}$ for the FOSOF data acquired for the 0 and π configurations, respectively. After subtracting the FOSOF data acquired for the two configurations of the FOSOF regions, the FOSOF lineshape will have an additional phase factor of

$$\Delta\phi_c = \frac{1}{2}(\phi_c^{(0)} - \phi_c^{(\pi)}). \tag{3.36}$$

This phase factor shifts the zero-phase-crossing frequency f_{zc} determined from the FOSOF lineshape from the resonant frequency f_0. The frequency shift is given by

$$f_{zc} - f_0 = \langle\Delta\phi_c\rangle/S, \tag{3.37}$$

where S is the slope of the lineshape and, to account for the fact that $\Delta\phi_c$ could be rf-frequency dependent, we use $\langle\Delta\phi_c\rangle$, which is the phase shift due to rf coupling averaged over the rf frequencies.

The FOSOF slope S depends on the separation between the waveguides, electric field amplitude, and the beam speed. It is reasonable to assume that the

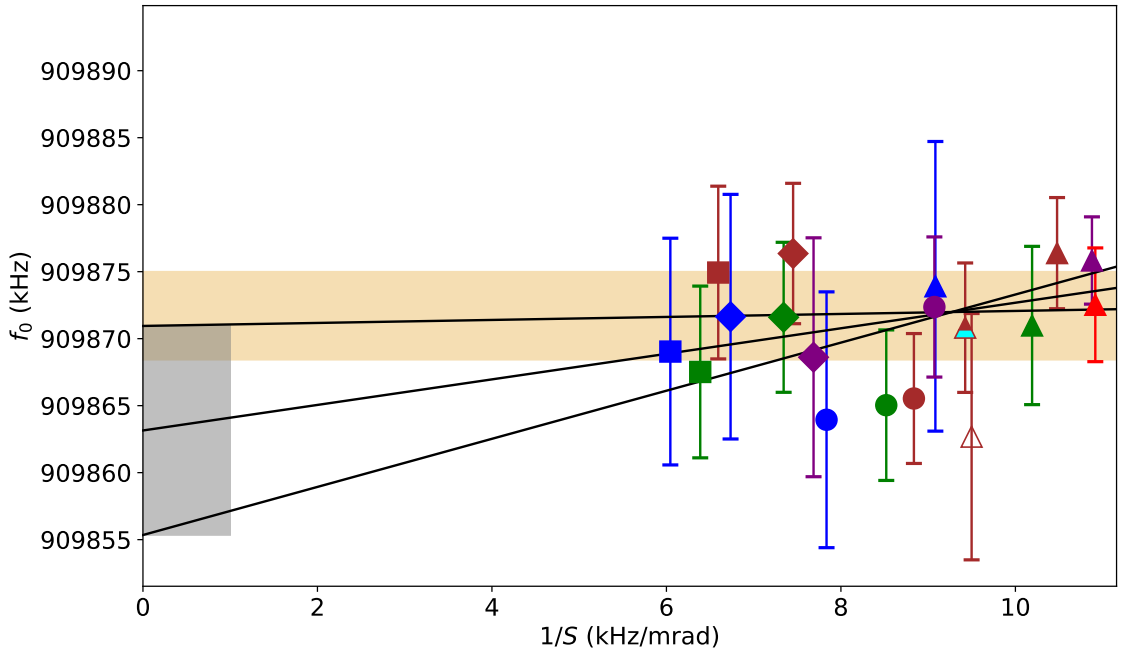

Figure 3.10: Frequency dependence on the inverse of the FOSOF slope. The linecenters (corrected for systematic effects) are listed in Table 4.1, and the slopes are listed in Table 3.3. Data in red, purple, brown, green, and blue corresponds to electric field strengths of 5, 8, 14, 18, and 24 V/cm, respectively. Triangles, circles, diamonds, and squares represent waveguide separations of 4, 5, 6, and 7 cm, respectively. The data acquired at nominal accelerating voltages of 16.27 and 22.17 kV are shown with a marker that is not filled, and with the bottom part of the marker filled in cyan, respectively. The data are fit to a line using the least-squares method. The gray band indicates one standard deviation of the extrapolated resonant frequency at very large separations between the waveguides. In pale yellow is the one standard deviation of the resonant frequency for the current measurement. The reduced chi-squared is 0.50 with 16 degrees of freedom.

possible coupling between the two arms of the rf system for the FOSOF regions is independent of the FOSOF slope. That is, the phase $\langle \Delta\phi_c \rangle$ is the same for different separations between the waveguides D, rf field amplitudes in the FOSOF regions E_0^{rf}, and beam speeds. With this assumption, we can use zero-crossing frequencies determined for different experimental parameters to determine the phase shift $\langle \Delta\phi_c \rangle$ due to rf coupling between the left and right arms of the rf system. The graph of the resonant frequencies obtained for different experimental parameters (and hence different FOSOF slopes) plotted versus the inverse of the FOSOF slope, $1/S$, is shown in Fig. 3.10. This data can be fit to Eq. 3.37 (as shown by the straight line in the plot), and the slope of the line gives

$$\langle \Delta\phi_c \rangle = 0.93(84)\,\mathrm{mrad}, \tag{3.38}$$

which is almost consistent with having no change in the phase between the waveguides and the combiners under the reversal. However, the extrapolated resonant frequency at $1/S = 0$ is

$$f_0(1/S = 0) = 909\,863(8)\,\mathrm{kHz}. \tag{3.39}$$

The large uncertainty for this extrapolation means that it cannot be used to rule out the effect of rf coupling on the scale of the 3.2-kHz uncertainty reported for this measurement. It is clear from Fig. 3.10 that the reason for large uncertainty is lack of data for small $1/S$ values. The uncertainty could be reduced by increasing the physical separation between the waveguides or by acquiring more data at the largest separation of $D = 7\,\mathrm{cm}$. Because the signal-to-noise ratio gets significantly worse for large D, these solutions would require many months of data acquisition. Because of these difficulties, we need a different method to determine the value of the change in the phase due to the waveguide reversal. This method is presented in the next section.

3.8.4 Direct measurement of $\Delta\phi_c$

Another method to determine the value of the change in the phase due to the waveguide reversal that does not involve atoms[38], is to directly measure the phase difference between the rf in the two waveguides relative to the phase difference measurements between combiners C1 and C2. This is achieved with the setup shown in Fig. 3.11. The coupled power from the waveguides is fed into a third rf combiner, and the phases of the beatnote signals from all of the three combiners are compared for the 0 and π configurations.

Measured values of $\Delta\phi_c$ (the phase difference measured in this third combiner minus the average of the phase differences measured in C1 and C2) as a function of the rf frequency for different waveguide separations and electric field amplitudes are shown in Fig. 3.12. Their average values (the average of ϕ_c for the different frequencies measured), $\langle\Delta\phi_c\rangle$, are listed in Table 3.12. This table suggest that larger electric field amplitudes lead to larger absolute values of $\langle\Delta\phi_c\rangle$. To be conservative, we choose the largest value in this table to assign a slope-dependent systematic uncertainty to the linecenters, determined for each set of the experimental parameters:

$$\langle\Delta\phi_c\rangle = 0.18\,\text{mrad}. \tag{3.40}$$

The calculated shifts in the resonant frequency due to the rf system not being identical for the two waveguide orientations are calculated using Eq. 3.37, and are listed in Table 3.13. By performing the final statistical analysis that is described in Sec. 4.3 and using the weights in Table 4.1, the correction to the resonant frequency of the $2S_{1/2}, f = 0 \rightarrow 2P_{1/2}, f = 1$ transition measured in this work due to an rf coupling between the left and rights arms of the rf system for the FOSOF regions

[38] And thus is not limited by the signal-to-noise ratio of the signal on the Lyman-α detector

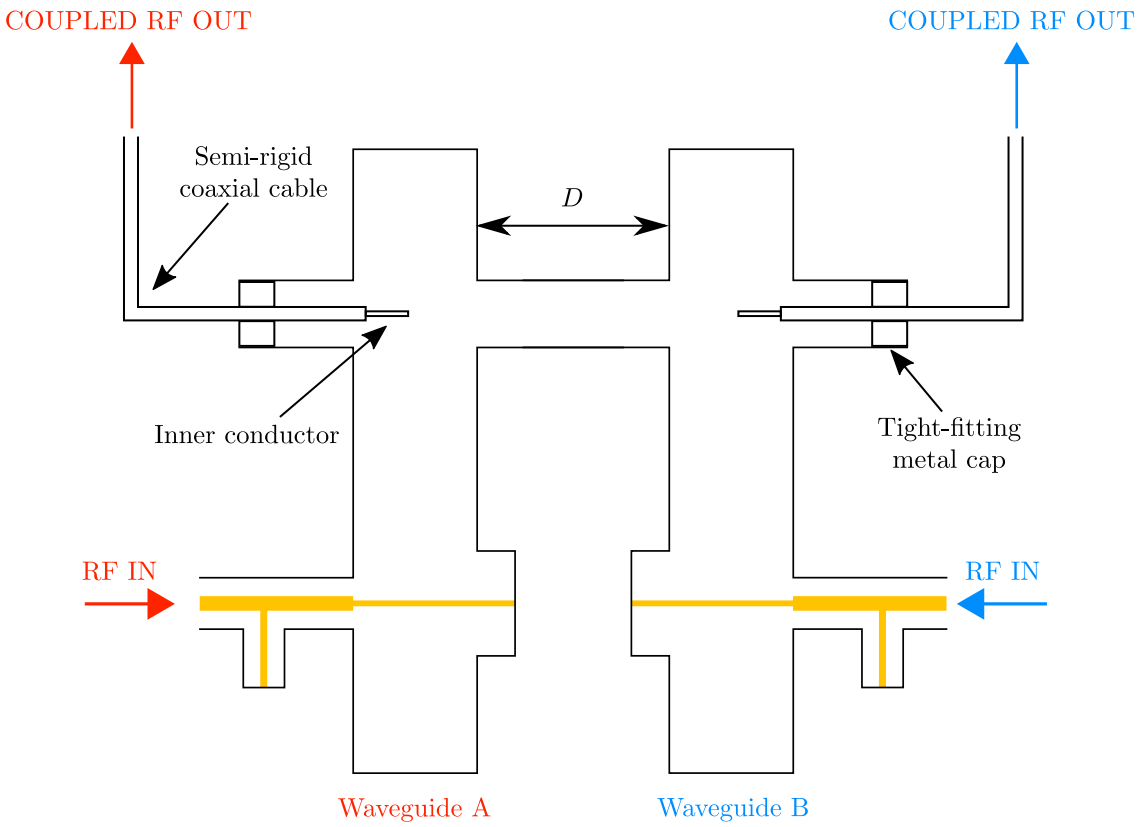

Figure 3.11: Measurement of the phase difference between the fields in the waveguides. For each of the waveguides, a semi-rigid coaxial cable is inserted concentrically into the tubes through which the atoms would otherwise travel. The other end of the coaxial cable is attached to the respective arm of the rf combiner, rigidly fixed to the waveguides (not shown). Since the rf choke tube and the outer shield of the coaxial cable now form a transmission line, the waveguides "see" the outer boundary conditions (walls of the vacuum chamber). To prevent this coupling, tight-fitting metal caps are inserted at the entrances of the rf choke tubes, simultaneously acting as a mechanical support for the coaxial cables.

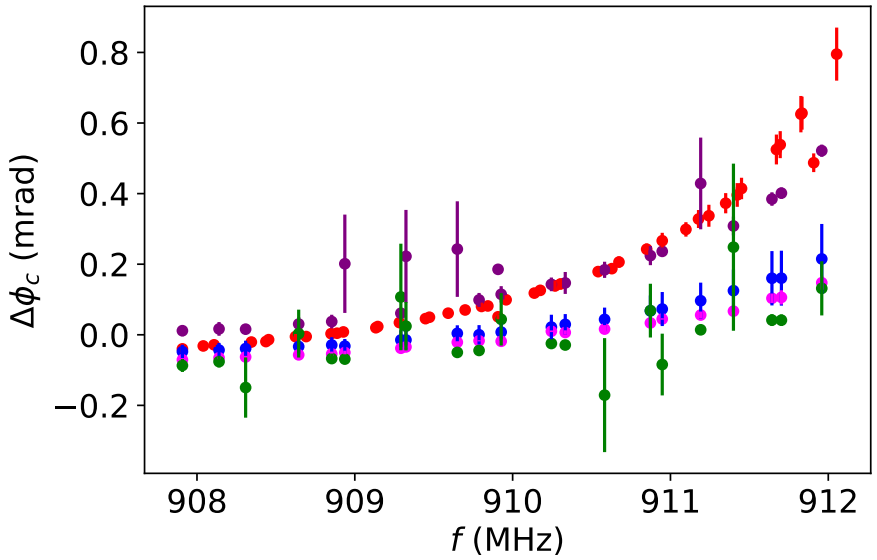

Figure 3.12: Plot of the change in the rf phase under waveguide reversal. The data were acquired for different waveguide separations D and electric field amplitudes E_0^{rf} for a range of rf frequencies. The data for $D = 7\,\mathrm{cm}$ and $E_0^{\mathrm{rf}} = 18\,\mathrm{V/cm}$ (in red) has the largest change in the rf phase $\Delta\phi_c$. The data in purple, acquired for $D = 4\,\mathrm{cm}$ and the same field amplitude, has very similar change in the phase. The data collected for the waveguide separation of $4\,\mathrm{cm}$ with $E_0^{\mathrm{rf}} = 8\,\mathrm{V\,cm}$ (in magenta), $E_0^{\mathrm{rf}} = 5\,\mathrm{V/cm}$ (in green), and for $D = 7\,\mathrm{cm}$ with $E_0^{\mathrm{rf}} = 8\,\mathrm{V/cm}$ (in blue) has smaller and almost identical effect on the phase difference between the combiners and the waveguides.

Table 3.12: Average measured phase shifts, $\langle \Delta\phi_c \rangle$, due to a possible rf coupling between the two arms of the rf system for the FOSOF regions. Experimental setup to measure these phases is shown in Fig. 3.11, and the measured phases are shown in Fig. 3.12. The first two columns are the separation between the waveguides D and the amplitude of the rf electric field in the FOSOF regions E_0^{rf}.

D (cm)	E_0^{rf} (V/cm)	$\langle \Delta\phi_c \rangle$ (mrad)
4	5	-0.03
4	8	-0.01
4	18	0.18
7	8	-0.01
7	18	-0.01

is determined to be

$$\Delta_c^{(\mathrm{rf})} = 0.0(15)\,\mathrm{kHz}. \tag{3.41}$$

An uncertainty of 1.5 kHz is therefore included in this work to account for possible mistakes in measuring relative rf phases.

Table 3.13: Shifts from imperfect determination of the relative phase of the rf fields in the two FOSOF regions. For each combination of the separation between the waveguides (D), the nominal accelerating voltage (V_{HV}), and the electric field amplitude (E_0^{rf}), the systematic uncertainty is calculated from Eq. 3.37 by using the corresponding value of the FOSOF slope (S) and the average value of the phase shift, $\langle \Delta\phi_c \rangle$, given in Eq. 3.40. The weighted average of these shifts is shown in the bottom row.

D (cm)	V_{HV} (kV)	E_0^{rf} (V/cm)	S (mrad/kHz)	$\Delta_c^{(\mathrm{rf})}$ (kHz)
4	16.27	14	0.1050(10)	0.0(17)
4	22.17	14	0.106 28(35)	0.0(17)
4	49.86	5	0.091 50(28)	0.0(20)
4	49.86	8	0.091 75(16)	0.0(20)
4	49.86	14	0.095 50(9)	0.0(19)
4	49.86	18	0.098 31(28)	0.0(18)
4	49.86	24	0.110 47(13)	0.0(16)
5	49.86	8	0.1103(5)	0.0(16)
5	49.86	14	0.113 36(26)	0.0(16)
5	49.86	18	0.1178(4)	0.0(15)
5	49.86	24	0.128 24(26)	0.0(14)
6	49.86	8	0.1299(10)	0.0(14)
6	49.86	14	0.1343(7)	0.0(13)
6	49.86	18	0.1370(4)	0.0(13)
6	49.86	24	0.1493(6)	0.0(12)
7	49.86	14	0.1519(8)	0.0(12)
7	49.86	18	0.1572(7)	0.0(11)
7	49.86	24	0.1672(7)	0.0(11)
			Weighted average:	0.0(15)

4 Data analysis

The main data for the current measurement consist of 116 data sets[39]. These 116 data sets include 18 combinations of experimental parameters (D, V_{HV}, E_0^{rf}), where, as was defined previously, D is the separation between the waveguides, V_{HV} is the nominal accelerating voltage, E_0^{rf} is the amplitude of the electric field in the waveguides.

In this chapter, the statistical analysis performed to determine the resonant frequency and its uncertainty is described. Consistency of the linecenters after correction for systematic effects is discussed.

4.1 Determination of f_{zc}

As was described in Sec. 2.8, to extract the FOSOF phase from the signals acquired from the Lyman-α detector and the combiners, two experiments need to be performed: one with the waveguides in the 0 configuration and one with them in the π configuration. After the data are acquired for one configuration, the waveguides are immediately reversed, and the data for the other configuration are collected[40]. The data for each configuration are acquired with a setup shown in panel (b) of Fig. 2.16 according to a scheme shown in Fig. 2.20. At the beginning

[39]Each consisting of the 0- and π-configuration pairs (cf. Sec. 2.10).

[40]Necessary preparations taken before starting to acquire these data are described in Sec. 2.10.

of the data acquisition, the rf frequency, f, output by the rf generator is randomly selected from a list of $N_f = 41$ values spanning a range of $\pm 2\,\mathrm{MHz}$ centered at approximately (this must be only approximate given hidden frequency offset and frequency jitters discussed in Sec. 2.10) 910 MHz. Next, it is randomly chosen whether half of the frequency offset $\frac{\Delta f}{2}$ is added to the frequency of the rf wave for waveguide A and subtracted from the frequency of the rf wave for waveguide B (such a case is shown in panel (b) of Fig. 2.16) or vice versa. (The subsequent data point is taken with the offset added to the other waveguide.) In the diagram shown in Fig. 2.20, $W^{(\Delta f)}$ denotes the waveguide (A or B), to which half of the offset frequency is added. For each data point, the traces of the Lyman-α-detector signal and of the beatnotes from the combiners C1 and C2 are recorded with two synchronized 2-channel digitizers, and these traces are repeated $N_t = 4$ times. This whole process is repeated for the whole set of the 41 rf frequencies N_r times.

For each trace (from the Lyman-α detector or the beatnote from one of the combiners), the phase (and the amplitude) of the component of the trace at the offset frequency is extracted using a fast Fourier transform. The phase difference between the extracted phases from the detector trace ($\phi^{\mathrm{W}^{(\Delta f)}}_{\mathrm{det(c)}}$) and a combiner trace ($\phi^{\mathrm{W}^{(\Delta f)}}_{\mathrm{beat(c)}}$) is calculated (the same notation is used to denote the phases as in Sec. 2.8, and the subscript c in the round brackets denotes the configuration of the waveguides (0 or π)):

$$\theta^{\mathrm{W}^{(\Delta f)}}_{(c)} = \phi^{\mathrm{W}^{(\Delta f)}}_{\mathrm{det(c)}} - \phi^{\mathrm{W}^{(\Delta f)}}_{\mathrm{beat(c)}}. \tag{4.1}$$

For the same rf frequency and $\mathrm{W}^{(\Delta f)}$ (the waveguide to which half of the offset frequency is added), the phase differences are averaged together to obtain $\langle\theta^A_{(c)}\rangle$ and $\langle\theta^B_{(c)}\rangle$. After averaging the phases for each rf frequency, the phase offset due to the limited bandwidth of the Lyman-α detector (and its associated electronics) is

canceled out by calculating (as was described in Sec. 2.8):

$$\theta_{(c)}^{AB} = \frac{1}{2}(\langle\theta_{(c)}^{B}\rangle - \langle\theta_{(c)}^{A}\rangle). \tag{4.2}$$

After, averaged phase differences for both waveguide configurations (as shown in (d) of Fig. 2.14) are subtracted from each other to obtain the FOSOF phase (Eq. 2.12):

$$\theta = \frac{1}{2}(\theta_{(0)}^{AB} - \theta_{(\pi)}^{AB}). \tag{4.3}$$

The FOSOF phase for the 41 rf frequencies is fit to a straight line:

$$\theta = S(f - f_{zc}), \tag{4.4}$$

where S is the FOSOF slope and f_{zc} is the zero-phase-crossing frequency. Best estimates of S and f_{zc} and their associated uncertainties are determined using the method of maximum likelihood.

From each data set we extract two zero-crossing frequencies. The first zero-crossing frequency, $f_{zc}^{(\mathrm{C1})}$, (with the uncertainty $\sigma_{f_{zc}}^{(\mathrm{C1})}$) is determined by using the beatnotes from combiner C1, related to the phase difference between the rf fields in the FOSOF regions. The second frequency, $f_{zc}^{(\mathrm{C2})}$, (with the uncertainty $\sigma_{f_{zc}}^{(\mathrm{C2})}$) is obtained by calculating the phase difference between the traces from the Lyman-α detector and combiner C2. It is natural to use the average of $f_{zc}^{(\mathrm{C1})}$ and $f_{zc}^{(\mathrm{C2})}$ as the best estimate for the zero-crossing frequency, f_{zc}[41]. The uncertainty in the zero-crossing frequency f_{zc} is

$$\sigma_{f_{zc}} = \frac{1}{\sqrt{2}}\sqrt{(\sigma_{f_{zc}}^{(\mathrm{C1})})^2 + (\sigma_{f_{zc}}^{(\mathrm{C2})})^2}. \tag{4.5}$$

One could argue that the if the beatnotes from the two combiners do not yield the same zero-crossing frequency, then it needs to be incorporated into the expression

[41]The motivation for this is that if the difference in the zero-crossing frequencies $f_{zc}^{(\mathrm{C1})}$ and $f_{zc}^{(\mathrm{C2})}$ is due to a situation described Sec. 3.8.1 and depicted in part (b) of Fig. 3.9, then the average of the two zero-crossing frequencies yields the correct resonant frequency.

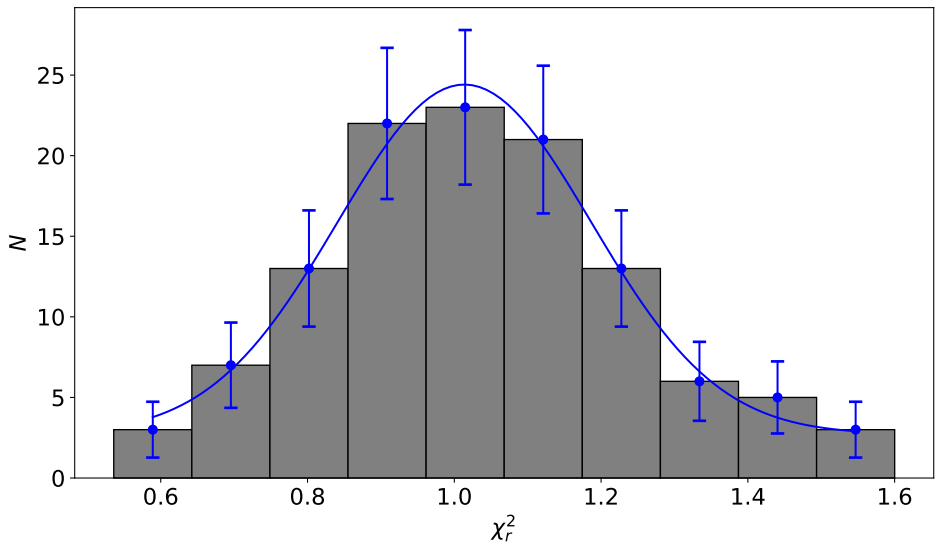

Figure 4.1: Distribution of the reduced chi-squared values, χ_r^2. The histogram has 10 bins. Uncertainty in the number of data sets (N), in a given bin is equal to $\sqrt{N}$. Fit to a Gaussian curve gives a mean of $\langle\chi_r^2\rangle = 1.01(2)$, and a standard deviation of $\sigma = 0.17(3)$.

for the uncertainty in Eq. 4.5. One possible choice is to add in quadrature to the $\sigma_{f_{zc}}$ of Eq. 4.5 an additional term $\sigma_{f_{zc}}^{\mathrm{C}} = |f_{zc}^{(\mathrm{C1})} - f_{zc}| = |f_{zc}^{(\mathrm{C2})} - f_{zc}|$, which is the absolute value of the deviation of zero-crossing frequencies, $f_{zc}^{(\mathrm{C1})}$ and $f_{zc}^{(\mathrm{C2})}$, from their average, f_{zc}. It was mentioned in Sec. 3.8.1 that on average the two zero-crossing frequencies, $f_{zc}^{(\mathrm{C1})}$ and $f_{zc}^{(\mathrm{C2})}$, differ by 0.16 kHz – much less than the uncertainty of the current measurement. Therefore, it is reasonable to treat the deviation $\sigma_{f_{zc}}^{\mathrm{C}}$ as a statistical uncertainty, justifying the addition of this term in quadrature with $\sigma_{f_{zc}}$. However, it is not necessary to include this additional statistical uncertainty, because such an analysis yields the same value of the resonant frequency and the same associated uncertainty (to 0.1 kHz), as reported in this work.

Zero-crossing frequencies and associated reduced chi-squared values χ_r^2 (with 39 degrees of freedom for each data set) for the straight-line fits of all of the 116

data sets are listed in Table B.1. A histogram of the chi-squared values, shown in Fig. 4.1, conforms to a normal distribution (which is a good approximation of a χ^2 distribution for 39 degrees of freedom) with a mean of $\langle \chi_r^2 \rangle = 1.01(2)$, consistent with the expected value of 1. Consequently, the uncertainties for the zero-crossing frequencies do not need to be expanded.

4.2 Systematic corrections

A weighted average of zero-crossing frequencies is calculated for each set of the experimental parameters. To convert a zero-crossing frequency f_{zc}, to the resonant frequency f_0, of the $2S_{1/2}, f = 0 \rightarrow 2P_{1/2}, f = 1$ transition, three corrections are applied: the first correction is due to the AC Stark shift (Table 3.8), the second correction arises from the second-order Doppler shift (Table 3.4), and the third correction is related to the imperfect determination of the relative phase of the rf fields in the two FOSOF regions (Table 3.13). The AC-shift correction is subtracted from, and the second-order-Doppler-shift correction is added to the zero-crossing frequencies. Resonant frequencies with associated statistical and systematic uncertainties determined for 18 experimental parameters are listed in Table 4.1.

4.3 Final statistical analysis: calculation of the resonant frequency, f_0

For this experiment, an uncertainty for each type of systematic correction cannot be treated as an independent uncertainty for different experimental parameters. For example, all of the data, acquired at a nominal accelerating voltage of 49.86 kV, has the same correction due to the second-order Doppler shift, and therefore the

Table 4.1: Systematic corrections, and corrected zero-crossing frequencies, f_0 (and associated statistical and systematic uncertainties) for the 18 sets of experimental parameters used for the measurement. The corrections are due to AC Stark shift (Δ_{AC}), second-order Doppler shift (Δ_{SOD}), and imperfect determination of the relative phase of the rf fields in the two FOSOF regions ($\Delta_c^{(\mathrm{rf})}$). The number of averaged datasets to calculate the linecenter for each set of experimental parameters, N, with the corresponding reduced chi-squared values, χ_r^2, are included. The sum of the weights for each separation between the waveguides, D, is set to 25%. The weights for a particular D are chosen to minimize the final uncertainty in the reported value for the resonant frequency, disregarding the uncertainty of the $\Delta_c^{(\mathrm{rf})}$ correction (see Sec. 4.3 for details).

D (cm)	V_{HV} (kV)	E_0^{rf} (V/cm)	Weight (%)	Δ_{AC} (kHz)	Δ_{SOD} (kHz)	$\Delta_c^{(\mathrm{rf})}$ (kHz)	χ_r^2	N	$f_0 \pm \sigma_{\mathrm{stat}} \pm \sigma_{\mathrm{sys}}$ (kHz)
4	16.27	14	0.5	28.6(23)	20.0(4)	0.0(17)	0.81	4	$909862.7 \pm 8.6 \pm 2.9$
4	22.17	14	3.0	32.4(22)	25.7(5)	0.0(17)	1.56	9	$909870.2 \pm 3.9 \pm 2.8$
4	49.86	5	6.3	5.5(8)	52.6(11)	0.0(20)	0.74	16	$909872.5 \pm 3.5 \pm 2.4$
4	49.86	8	15.3	13.5(13)	52.6(11)	0.0(20)	2.40	14	$909875.8 \pm 2.0 \pm 2.6$
4	49.86	14	0.0	42.9(33)	52.6(11)	0.0(19)	1.49	7	$909876.4 \pm 1.1 \pm 4.0$
4	49.86	18	0.0	75.1(54)	52.6(11)	0.0(18)	4.66	5	$909870.4 \pm 0.8 \pm 5.8$
4	49.86	24	0.0	152.9(105)	52.6(11)	0.0(16)	2.40	3	$909874.7 \pm 1.2 \pm 10.6$
5	49.86	8	10.5	10.0(14)	52.6(11)	0.0(16)	0.76	6	$909872.4 \pm 4.6 \pm 2.4$
5	49.86	14	11.1	34.4(29)	52.6(11)	0.0(16)	1.18	3	$909865.6 \pm 3.3 \pm 3.4$
5	49.86	18	3.4	61.6(46)	52.6(11)	0.0(15)	0.56	3	$909865.0 \pm 2.5 \pm 4.9$
5	49.86	24	0.0	128.8(90)	52.6(11)	0.0(14)	3.53	3	$909863.9 \pm 2.2 \pm 9.2$
6	49.86	8	4.2	8.3(11)	52.6(11)	0.0(14)	1.42	18	$909868.6 \pm 8.7 \pm 2.1$
6	49.86	14	11.7	29.1(24)	52.6(11)	0.0(13)	0.82	7	$909876.4 \pm 4.3 \pm 2.9$
6	49.86	18	9.1	52.4(38)	52.6(11)	0.0(13)	0.61	4	$909871.6 \pm 3.7 \pm 4.2$
6	49.86	24	0.0	110.9(77)	52.6(11)	0.0(12)	0.03	2	$909871.6 \pm 4.5 \pm 7.8$
7	49.86	14	11.6	26.3(20)	52.6(11)	0.0(12)	1.35	3	$909874.9 \pm 5.9 \pm 2.5$
7	49.86	18	11.1	46.8(32)	52.6(11)	0.0(11)	1.18	6	$909867.5 \pm 5.3 \pm 3.6$
7	49.86	24	2.4	98.6(68)	52.6(11)	0.0(11)	2.43	3	$909869.1 \pm 4.8 \pm 6.9$

uncertainties for this correction, applied to 16 sets of experimental parameters, are not independent. As a second example, the uncertainty of the correction due to the uncertainty in the determination of the relative phase of the rf fields in the two FOSOF regions is dominated by the uncertainty in the quantity $\langle \Delta\phi_c \rangle$, scaled by respective FOSOF slope for each set of experimental parameters (see Sec. 3.8, and Eq. 3.37), and therefore the uncertainties are correlated. Based on this discussion, the final uncertainty, σ_c, for each correction c, is equal to the weighted sum of respective uncertainties for each set of the experimental parameters:

$$\sigma_c = \sum_{j=1}^{18} w_j \sigma_{c_j}; \tag{4.6}$$

where j is a pointer to one of the 18 sets of the experimental parameters and w_j is the assigned weight for the jth experimental parameter set. The total sum of the weights is set to unity:

$$\sum_{j=1}^{18} w_j = 1. \tag{4.7}$$

The overall uncertainty for all systematic corrections is

$$\sigma_{\text{sys}} = \sqrt{\sum_c \sigma_c^2}. \tag{4.8}$$

And the final statistical uncertainty is calculated by adding the statistical uncertainties in quadrature with the same set of weights, $\{\omega_j\}$:

$$\sigma_{\text{stat}} = \sqrt{\sum_{j=1}^{18} w_j^2 \sigma_{\text{stat}_j}^2}. \tag{4.9}$$

The reported value for the resonant frequency is

$$\langle f_0 \rangle = \sum_{j=1}^{18} w_j f_{0_j}, \tag{4.10}$$

Table 4.2: Summary of systematic corrections.

	Weighted average (kHz)
AC shift, $\Delta_{\rm AC}$	29.5 ± 2.3
Second-order Doppler shift, $\Delta_{\rm SOD}$	51.6 ± 1.0
Phase error, $\Delta_c^{(\rm rf)}$	0.0 ± 1.5
$f(2S_{1/2},\, f=0 \rightarrow 2P_{1/2},\, f=1)$	$909871.7 \pm 1.4 \pm 2.9$

with the total uncertainty equal to

$$\sigma_{\langle f_0 \rangle} = \sqrt{\sigma_{\rm stat}^2 + \sigma_{\rm sys}^2}. \tag{4.11}$$

The weights are chosen to minimize the total uncertainty $\sigma_{\langle f_0 \rangle}$ subject to the condition that a total weight of 25% is applied to each separation between the waveguides. This condition reflects the fact that changing the separation between the FOSOF regions is the most important test for systematic effects in this experiment, because it simultaneously affects the FOSOF slope, the AC shift, and, if present, effect of high-n states on the lineshape. Therefore, the results obtained for each separation are equally important in determining the final answer for the linecenter.

The calculated weights are listed in Table 4.1[42]. Table 4.2 lists the frequency of the $2S_{1/2},\, f=0 \rightarrow 2P_{1/2},\, f=1$ interval (calculated from Eq. 4.10), with weighted averages of the corrections.

[42]It was mentioned in Sec. 2.10 that the analysis of the data is performed with a hidden offset applied to all of the rf frequencies. This offset was revealed to us before we devised the method to measure the phase between the fields in the FOSOF regions directly to estimate the correction due to insufficiently suppressed coupling between different parts of the rf system with the environment. As the result, the weights in Table 4.1 are calculated without including the uncertainty of the $\Delta_c^{(\rm rf)}$ correction. We believe that it is not fair to recalculate the weights after revealing the hidden offset. That is why the weights are kept unchanged. However, a new set of weights calculated with all of the uncertainties included changes the reported value for the linecenter by a mere 0.2 kHz, leaving the systematic and statistical uncertainties essentially unchanged.

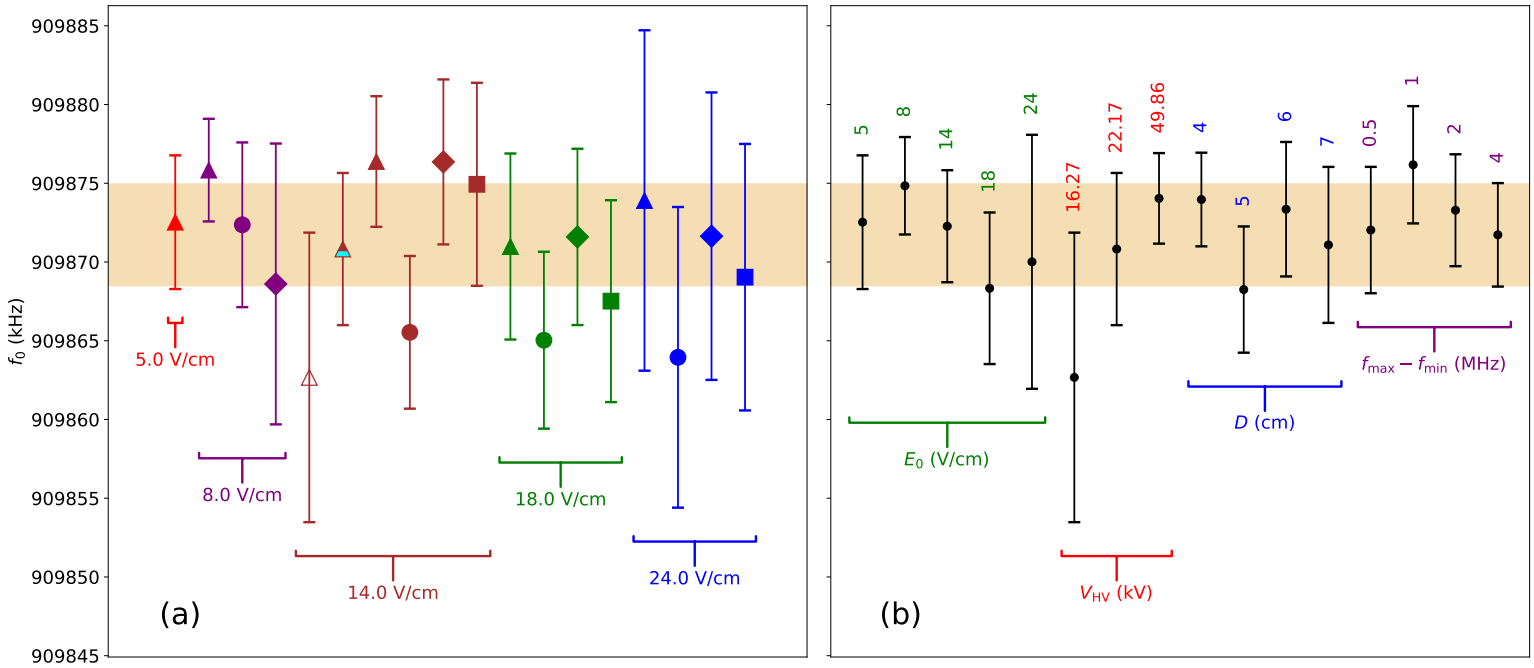

Figure 4.2: Linecenters for different combinations of D, V_{HV}, E_0^{rf}. Part (a) is the plot of the averaged linecenters for each set of the experimental parameters. Triangles, circles, diamonds, and squares represent a waveguide separation of 4, 5, 6, and 7 cm, respectively. The data, acquired at a nominal accelerating voltage of 16.27 and 22.17 kV, are shown with the marker that is not filled, and with the bottom part of the marker filled in cyan color, respectively. Part (b) is the plot of the averaged linecenters, calculated by separately averaging the linecenters corresponding to the same separation between the waveguides (D), the same nominal accelerating voltage (V_{HV}), and the same electric field amplitude (E_0^{rf}). The points shown in purple represent the linecenters determined by including only a limited range of frequencies, $f_{\mathrm{max}} - f_{\mathrm{min}}$ (are the difference between the maximum and minimum frequencies, respectively, centered about 910 MHz), used in the analysis of each of the 116 datasets. The shaded region is the one standard deviation in the resonant frequency for the current measurement.

4.4 Consistency of the linecenters

Panel (a) of Fig. 4.2 shows the plot of the resonant frequencies calculated for each set of experimental parameters. The uncertainty for each point is calculated by adding in quadrature the uncertainties of the individual corrections and the statistical uncertainty (listed in the last column of Table 4.1). The linecenters for different experimental parameters are consistent with the reported resonant frequency.

As another test for hidden systematic effects, in addition to visualizing the distribution of the linecenters corresponding to each set of experimental parameters, we also average the linecenters belonging separately to the same D, $V_{\rm HV}$, and $E_0^{\rm rf}$[43]. These averaged linecenters are shown in part (b) of Fig. 4.2. These linecenters also show consistency, and deviate from the reported resonant frequency by less than one standard deviation.

In this experiment, all of the data sets are acquired with a range of frequencies of 4 MHz (centered about approximately 910 MHz). To test for possible dependence of the resonant frequency on the range of frequencies, we separately include in the analysis outlined in Sec. 4.1 only the frequencies belonging to a frequency range of 2, 1, and 0.5 MHz. The same weights as in Table 4.1 are used to calculate average frequencies for each of the frequency ranges, which are plotted in panel (b) of Fig. 4.2. No dependence of the linecenters on the frequency range is observed.

Lastly, it is important to mention that the average chi-squared calculated from columns 8 and 9 of Table 4.1 is 130, 2.3 standard deviations away from the expected value of 98 (with a reduced chi-squared of 1.33). Examination of Table 4.1 reveals that such a large chi-squared value is due to a single linecenter calculated for $D = 4\,\text{cm}$, $V_{\rm HV} = 49.86\,\text{kV}$, $E_0^{\rm rf} = 8\,\text{V/cm}$: its reduced chi-squared is $\chi_r^2 = 2.37$ for 14

[43]To calculate the average, the same procedure of minimization of weights described in Sec. 4.3 is performed, but without the constraint to allocate 25% of the total weight to each of the 4 waveguide separations.

degrees of freedom, with a probability of 0.4% to obtain a larger chi-squared value. If the statistical uncertainty for this particular linecenter is expanded by $\sqrt{2.37}$, then the average chi-squared becomes 112, 1.0 standard deviations away from the expected value. If the analysis for calculating the weighted average of the linecenters described in Sec. 4.3 is performed with the expanded statistical uncertainty for the aforementioned linecenter (by calculating a new set of weights), then the final result for the resonant frequency decreases by 0.2 kHz, and its uncertainty increases by 0.05 kHz. These changes are insignificant compared to a total uncertainty of 3.2 kHz reported for this measurement, and we have not expanded the uncertainties.

5 Conclusion

We performed a high-precision measurement of the frequency difference between the $2S_{1/2}, f = 0$ and $2P_{1/2}, f = 1$ states in atomic hydrogen using a novel method of the frequency-offset separated oscillatory fields (Sec. 1.3.2). The obtained result (cf. Table 4.2) is

$$f(2S_{1/2},\ f = 0\ \rightarrow 2P_{1/2},\ f = 1)[\text{this work}] = 909\,871.7(32)\,\text{kHz},$$

with the 3.2-kHz uncertainty resulting from a statistical uncertainty of 1.4 kHz and a systematic uncertainty of 2.9 kHz.

Table 5.1 lists the result of the current measurement and the previously most precise measurement of this transition, performed in 1981 by Lundeen and Pipkin [10], as well as the result obtained from the recent reanalysis of that experiment [9]. The transition frequency quoted in this work is 1.7 standard deviations away from the transition frequency reported by Lundeen and Pipkin and 1.1 standard deviations different from the reanalysis of their measurement. Our measurement reduces the uncertainty in the experimentally determined frequency of the $2S_{1/2}f = 0 \rightarrow 2P_{1/2}, f = 1$ transition by a factor of 2.8 and 6.2, compared to the original and reanalyzed measurements performed by Lundeen and Pipkin, respectively.

A careful study of systematic effects was performed (Ch. 3), and consistent corrected linecenters (Sec. 4.4) were found for 4 separations between the FOSOF

Table 5.1: Measurements of the frequency difference between the $2S_{1/2}, f = 0$ and $2P_{1/2}, f = 1$ states in atomic hydrogen.

	$f(2S_{1/2},\, f = 0 \rightarrow 2P_{1/2},\, f = 1)$ (kHz)
This work	909871.7 ± 3.2
Lundeen and Pipkin (1981) [10]	909887 ± 9
Lundeen and Pipkin (reanalyzed, 2018) [9]	909894 ± 20

regions, different rf power levels in the regions, and different speeds of the metastable beam.

The $n = 2$ Lamb shift can be determined from our result, by adding the hyperfine contribution to the frequency difference between the $2S_{1/2}, f = 0$ and $2P_{1/2}, f = 1$ states, listed in Table 1.1:

$$\begin{aligned} f(2S_{1/2} \rightarrow 2P_{1/2}) &= 909\,871.7(32)\,\text{kHz} + 147\,958.1(0)\,\text{kHz} \\ &= 1\,057\,829.8(32)\,\text{kHz} \end{aligned} \tag{5.1}$$

The root-mean-squared charge radius of the proton can be determined from Eq. 1.1. Using the CODATA 2014 value for the Rydberg constant [5], the result is

$$r_p[\text{this work}] = 0.833(10)\,\text{fm}. \tag{5.2}$$

Note that compared to proton radius determinations from transition frequencies between states with different principal quantum numbers, this determination is insensitive to the value of the Rydberg constant used.

Figure 1.1 shows various ways to determine the proton radius, including the proton radius from our measurement. The CODATA 2014 recommended value for the proton radius is:

$$r_p[\text{CODATA 2014}] = 0.8751(61)\,\text{fm}. \tag{5.3}$$

Our result is 4.2 standard deviation away from this value. However, it is consistent (within 0.8 standard deviations) with the proton radius value, extracted from muonic-hydrogen spectroscopy:

$$r_p[\mu\mathrm{H}] = 0.840\,87(39)\,\mathrm{fm}. \tag{5.4}$$

This experiment serves as the direct comparison of the frequencies of the $2S \rightarrow 2P$ transitions in ordinary hydrogen and muonic hydrogen. Our measurement suggests that both types of hydrogen yield consistent values for the root-mean squared charge radius of the proton.

Using the value of the proton radius, determined by the CREMA collaboration (Eq. 5.4), the predicted transition frequency between the $2S_{1/2}, f = 0$ and $2P_{1/2}, f = 1$ states is (cf. Table 1.1):

$$f(2S_{1/2},\ f = 0 \rightarrow 2P_{1/2},\ f = 1)[\mathrm{predicted}] = 909\,874.2(3)\,\mathrm{kHz}. \tag{5.5}$$

Our result is consistent with the predicted value.

A FOSOF lineshape for a small driving-field amplitude

The derivation of the FOSOF lineshape, presented in Sec. 1.3.2, is based on direct solution of the Schrödinger equation. The FOSOF lineshape can also be derived from perturbation theory (for sufficiently small rf electric field amplitudes)[44]. Such a derivation permits an alternative lineshape, which is valid for small rf fields.

In this formalism, the probability amplitude for the atom in the state $|1\rangle$ to remain in this state after passing through two temporally-separated regions of rf field is the sum of the probability amplitudes of two "paths", shown in Fig. A.1. The first path has the particle passing unperturbed through both of the fields; this is the zeroth-order contribution. For the second path the atom experiences two transitions: in the first region the atom is transitioned to state $|2\rangle$, and in the second regions it transitions back to state $|1\rangle$; this is the second-order term in the

[44]Perturbation theory is used extensively in the thesis of S. R. Lundeen, and is developed in Appendix A of [38] with a phenomenological incorporation of the spontaneous decay.

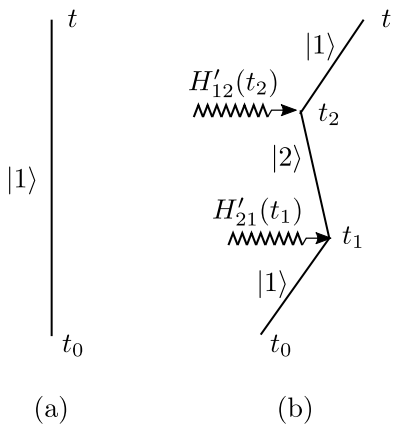

Figure A.1: Probability amplitudes in FOSOF. The zeroth-order (a) and the second-order (b) contributions are shown, with $H'_{i,j}(t) = \langle i|H'(t)|j\rangle$, and H' is equal to $W^{(\mathrm{RWA})}(t)$ (cf. Eq. 1.10). The diagrams follow the style of [37].

series. The total probability contains an interference term between these two paths, $P^{(\mathrm{int})}_{|1\rangle\to|1\rangle}$. With the omission of the spontaneous decay, this term is equal to

$$P^{(\mathrm{int})}_{|1\rangle\to|1\rangle} = A\cos(\Omega(T+\tau)+\Delta\omega t), \tag{A.1}$$

where

$$A = -2\frac{E_0^2|p_z|^2}{\hbar^2}\frac{\sin^2(\Omega\tau/2)}{\Omega^2}. \tag{A.2}$$

The FOSOF lineshape is then

$$\theta = \Omega(T+\tau), \tag{A.3}$$

which has the slope of $T+\tau$, equal to the slope of Eq. 1.23 in the limit of weak rf field amplitude.

B Data tables

Table B.1: FOSOF lineshape parameters determined from the 116 data sets. For each of these 116 data sets, the FOSOF phases were determined for the same set of 41 rf frequencies, which are listed in Table B.2. The first three columns specify experimental parameters, which are the separation between the waveguides D, the nominal accelerating voltage V_{HV}, related to the speed of the atomic beam, and the amplitude of the rf electric field in the FOSOF waveguides E_0^{rf}. Determination of zero-crossing frequencies, f_{zc}, and FOSOF slopes, S, is described in Sec. 4.1. Reduced chi-squared values, χ_r^2, of the fits of FOSOF data to a straight line are listed. The f_{zc} values listed are not corrected for systematic corrections, and therefore need to be corrected for AC Stark shift, second-order Doppler shift, and phase uncertainties, as described in Chapter 3.

D (cm)	V_{HV} (kV)	E_0^{rf} (V/cm)	f_{zc} (kHz)	χ_r^2	S (mrad/kHz)
4	16.27	14	909 874.6(172)	1.12	0.1054(15)
4	16.27	14	909 877.0(163)	1.22	0.1078(15)
4	16.27	14	909 884.6(178)	1.12	0.1029(15)
4	16.27	14	909 848.7(173)	0.98	0.1049(15)

Continued on next page

Table B.1 – continued from previous page

D (cm)	V_{HV} (kV)	E_0 (V/cm)	f_{zc} (kHz)	χ^2_r	S (mrad/kHz)
4	22.17	14	909 880.1(124)	1.39	0.1061(11)
4	22.17	14	909 841.7(133)	1.39	0.1060(12)
4	22.17	14	909 881.0(122)	1.20	0.1059(11)
4	22.17	14	909 865.5(122)	0.93	0.1064(11)
4	22.17	14	909 873.1(117)	0.83	0.1043(10)
4	22.17	14	909 872.7(113)	1.13	0.1064(10)
4	22.17	14	909 879.0(111)	1.00	0.1063(10)
4	22.17	14	909 890.8(110)	1.09	0.1069(10)
4	22.17	14	909 892.6(99)	1.23	0.1065(9)
4	49.86	5	909 820.2(113)	1.16	0.0923(9)
4	49.86	5	909 811.4(114)	1.23	0.0913(8)
4	49.86	5	909 820.0(127)	1.05	0.0895(9)
4	49.86	5	909 821.3(143)	1.16	0.0946(11)
4	49.86	5	909 804.7(153)	1.19	0.0935(12)
4	49.86	5	909 814.7(141)	0.74	0.0922(11)
4	49.86	5	909 836.9(157)	1.12	0.0917(12)

Continued on next page

Table B.1 – continued from previous page

D (cm)	V_{HV} (kV)	E_0 (V/cm)	f_{zc} (kHz)	χ^2_r	S (mrad/kHz)
4	49.86	5	909 832.6(142)	1.24	0.0924(11)
4	49.86	5	909 816.3(149)	0.90	0.0919(11)
4	49.86	5	909 839.8(164)	1.10	0.0910(12)
4	49.86	5	909 820.5(175)	1.60	0.0917(13)
4	49.86	5	909 833.0(150)	1.02	0.0913(11)
4	49.86	5	909 822.9(146)	0.93	0.0904(11)
4	49.86	5	909 847.2(146)	1.03	0.0904(11)
4	49.86	5	909 841.9(146)	0.96	0.0907(11)
4	49.86	5	909 838.4(138)	0.85	0.0915(10)
4	49.86	8	909 817.4(81)	1.53	0.0925(6)
4	49.86	8	909 850.6(78)	0.82	0.0925(6)
4	49.86	8	909 853.9(72)	0.95	0.0927(6)
4	49.86	8	909 820.8(75)	0.74	0.0911(6)
4	49.86	8	909 836.2(74)	0.62	0.0920(6)
4	49.86	8	909 822.8(77)	0.79	0.0912(6)
4	49.86	8	909 831.8(72)	1.06	0.0922(5)

Continued on next page

Table B.1 – continued from previous page

D (cm)	V_{HV} (kV)	E_0 (V/cm)	f_{zc} (kHz)	χ^2_r	S (mrad/kHz)
4	49.86	8	909 850.4(73)	0.87	0.0932(6)
4	49.86	8	909 834.8(73)	0.95	0.0920(6)
4	49.86	8	909 843.7(81)	1.36	0.0917(6)
4	49.86	8	909 823.4(89)	1.40	0.0926(7)
4	49.86	8	909 842.3(45)	0.79	0.091 67(34)
4	49.86	8	909 834.4(106)	1.10	0.0909(8)
4	49.86	8	909 833.8(86)	1.11	0.0906(6)
4	49.86	14	909 867.6(33)	1.22	0.095 26(26)
4	49.86	14	909 863.1(31)	1.31	0.095 42(25)
4	49.86	14	909 871.7(31)	1.10	0.095 11(24)
4	49.86	14	909 862.1(26)	1.46	0.095 51(20)
4	49.86	14	909 865.3(26)	0.98	0.095 55(21)
4	49.86	14	909 869.3(27)	0.79	0.095 59(21)
4	49.86	14	909 868.5(27)	0.94	0.095 49(21)
4	49.86	18	909 896.5(22)	0.75	0.099 04(18)
4	49.86	18	909 894.8(25)	1.06	0.099 39(20)

Continued on next page

Table B.1 – continued from previous page

D (cm)	V_{HV} (kV)	E_0 (V/cm)	f_{zc} (kHz)	χ^2_r	S (mrad/kHz)
4	49.86	18	909 890.0(17)	1.37	0.097 47(14)
4	49.86	18	909 888.3(17)	0.77	0.097 51(14)
4	49.86	18	909 896.2(15)	0.88	0.098 25(12)
4	49.86	24	909 976.1(15)	1.38	0.110 04(13)
4	49.86	24	909 968.5(32)	0.83	0.110 07(29)
4	49.86	24	909 976.3(30)	1.14	0.110 38(28)
5	49.86	8	909 834.5(100)	1.02	0.1099(9)
5	49.86	8	909 839.8(105)	0.96	0.1098(10)
5	49.86	8	909 822.3(106)	0.63	0.1110(10)
5	49.86	8	909 829.7(109)	0.98	0.1101(10)
5	49.86	8	909 813.0(125)	1.00	0.1089(11)
5	49.86	8	909 839.7(164)	1.04	0.1133(15)
5	49.86	14	909 847.5(57)	0.96	0.1139(5)
5	49.86	14	909 841.3(56)	1.10	0.1125(5)
5	49.86	14	909 853.6(57)	0.90	0.1132(5)
5	49.86	18	909 874.5(44)	1.05	0.1174(4)

Continued on next page

Table B.1 – continued from previous page

D (cm)	V_{HV} (kV)	E_0 (V/cm)	f_{zc} (kHz)	χ^2_r	S (mrad/kHz)
5	49.86	18	909 870.6(43)	1.08	0.1172(4)
5	49.86	18	909 877.1(45)	0.82	0.1175(4)
5	49.86	24	909 948.4(38)	1.15	0.1278(4)
5	49.86	24	909 935.8(39)	1.11	0.1273(4)
5	49.86	24	909 935.9(39)	1.34	0.1278(4)
6	49.86	8	909 830.5(329)	0.97	0.1269(34)
6	49.86	8	909 821.6(371)	1.05	0.128(4)
6	49.86	8	909 884.1(363)	1.06	0.133(4)
6	49.86	8	909 735.9(375)	1.12	0.127(4)
6	49.86	8	909 839.4(307)	1.06	0.1324(33)
6	49.86	8	909 792.5(323)	0.70	0.1310(34)
6	49.86	8	909 835.1(922)	0.95	0.140(11)
6	49.86	8	909 945.2(395)	1.25	0.128(4)
6	49.86	8	909 842.5(386)	0.88	0.131(4)
6	49.86	8	909 794.2(360)	1.20	0.135(4)
6	49.86	8	909 781.0(415)	0.89	0.130(4)

Continued on next page

Table B.1 – continued from previous page

D (cm)	V_{HV} (kV)	E_0 (V/cm)	f_{zc} (kHz)	χ^2_r	S (mrad/kHz)
6	49.86	8	909 867.3(402)	0.91	0.129(4)
6	49.86	8	909 844.9(411)	0.86	0.136(5)
6	49.86	8	909 785.2(406)	1.11	0.120(4)
6	49.86	8	909 799.5(330)	1.06	0.1298(35)
6	49.86	8	909 808.5(354)	1.06	0.132(4)
6	49.86	8	909 829.4(337)	0.92	0.130(4)
6	49.86	8	909 826.3(324)	1.08	0.1329(35)
6	49.86	14	909 837.3(122)	0.70	0.1327(13)
6	49.86	14	909 850.5(114)	0.81	0.1326(12)
6	49.86	14	909 863.4(113)	0.64	0.1340(13)
6	49.86	14	909 853.4(151)	0.85	0.1329(17)
6	49.86	14	909 866.1(100)	0.73	0.1365(11)
6	49.86	14	909 844.9(102)	1.37	0.1333(11)
6	49.86	14	909 850.6(113)	1.18	0.1363(13)
6	49.86	18	909 879.6(101)	1.02	0.1351(11)
6	49.86	18	909 875.9(68)	0.98	0.1366(8)

Continued on next page

Table B.1 – continued from previous page

D (cm)	V_{HV} (kV)	E_0 (V/cm)	f_{zc} (kHz)	χ^2_r	S (mrad/kHz)
6	49.86	18	909 868.1(67)	1.25	0.1358(8)
6	49.86	18	909 866.6(68)	0.93	0.1367(8)
6	49.86	24	909 930.7(62)	0.83	0.1483(8)
6	49.86	24	909 929.2(66)	1.12	0.1486(8)
7	49.86	14	909 836.5(115)	0.87	0.1520(14)
7	49.86	14	909 846.3(92)	0.69	0.1512(11)
7	49.86	14	909 861.5(104)	1.27	0.1519(13)
7	49.86	18	909 863.1(150)	0.54	0.1568(19)
7	49.86	18	909 874.6(138)	0.86	0.1553(17)
7	49.86	18	909 862.8(126)	1.49	0.1572(16)
7	49.86	18	909 878.7(126)	1.16	0.1574(16)
7	49.86	18	909 852.9(127)	0.98	0.1559(16)
7	49.86	18	909 841.6(122)	1.55	0.1567(16)
7	49.86	24	909 896.3(98)	0.87	0.1655(13)
7	49.86	24	909 919.5(96)	0.88	0.1659(13)
7	49.86	24	909 922.0(68)	1.22	0.1652(9)

Table B.2: The set of rf frequencies used for acquiring FOSOF data sets. For each of the 116 FOSOF data sets, the FOSOF phases were determined for this set of 41 rf frequencies, f.

Index	f (Hz)	Index	f (Hz)	Index	f (Hz)
1	907939783	15	909480082	29	910881506
2	908071901	16	909505038	30	910980061
3	908140347	17	909623630	31	911130105
4	908376575	18	909731246	32	911209870
5	908468910	19	909835108	33	911275607
6	908485918	20	909875152	34	911382077
7	908656235	21	909990845	35	911455257
8	908723967	22	910169587	36	911482447
9	908881612	23	910207255	37	911703477
10	908919497	24	910301269	38	911727553
11	908959606	25	910335027	39	911858616
12	909165531	26	910573831	40	911865534
13	909177652	27	910660782	41	912085283
14	909314795	28	910705934		

Bibliography

[1] W. E. Lamb and R. C. Retherford, Phys. Rev. **72**, 241 (1947).

[2] H. A. Bethe, Phys. Rev. **72**, 339 (1947).

[3] D. Hanneke, S. Fogwell, and G. Gabrielse, Phys. Rev. Lett. **100**, 120801 (2008).

[4] R. H. Parker, C. Yu, W. Zhong, B. Estey, and H. Müller, Science **360**, 191 (2018).

[5] P. J. Mohr, D. B. Newell, and B. N. Taylor, Rev. Mod. Phys. **88**, 35009 (2016).

[6] P. J. Mohr, B. N. Taylor, and D. B. Newell, Journal of Physical and Chemical Reference Data **41**, 43109 (2012).

[7] R. Pohl, A. Antognini, F. Nez, F. D. Amaro, F. Biraben, J. M. R. Cardoso, D. S. Covita, A. Dax, S. Dhawan, L. M. P. Fernandes, A. Giesen, T. Graf, T. W. Hänsch, P. Indelicato, L. Julien, C.-Y. Kao, P. Knowles, E.-O. Le Bigot, Y.-W. Liu, J. A. M. Lopes, L. Ludhova, C. M. B. Monteiro, F. Mulhauser,

T. Nebel, P. Rabinowitz, J. M. F. Dos Santos, L. A. Schaller, K. Schuhmann, C. Schwob, D. Taqqu, J. F. C. A. Veloso, and F. Kottmann, Nature **466**, 213 (2010).

[8] A. Antognini, F. Nez, K. Schuhmann, F. D. Amaro, F. Biraben, J. M. R. Cardoso, D. S. Covita, A. Dax, S. Dhawan, M. Diepold, L. M. P. Fernandes, A. Giesen, A. L. Gouvea, T. Graf, T. W. Hänsch, P. Indelicato, L. Julien, C.-Y. Kao, P. Knowles, F. Kottmann, E.-O. Le Bigot, Y.-W. Liu, J. A. M. Lopes, L. Ludhova, C. M. B. Monteiro, F. Mulhauser, T. Nebel, P. Rabinowitz, J. M. F. dos Santos, L. A. Schaller, C. Schwob, D. Taqqu, J. F. C. A. Veloso, J. Vogelsang, and R. Pohl, Science **339**, 417 (2013).

[9] A. Marsman, M. Horbatsch, Z. A. Corriveau, and E. A. Hessels, Phys. Rev. A **98**, 12509 (2018).

[10] S. R. Lundeen and F. M. Pipkin, Phys. Rev. Lett. **46**, 232 (1981).

[11] N. Bezginov, T. Valdez, M. Horbatsch, A. Marsman, A. C. Vutha, and E. A. Hessels, Science **365**, 1007 (2019).

[12] M. Horbatsch and E. A. Hessels, Phys. Rev. C **93**, 15204 (2016).

[13] H. Fleurbaey, S. Galtier, S. Thomas, M. Bonnaud, L. Julien, F. Biraben, F. Nez, M. Abgrall, and J. Guéna, Phys. Rev. Lett. **120**, 183001 (2018).

[14] A. Beyer, L. Maisenbacher, A. Matveev, R. Pohl, K. Khabarova, A. Grinin, T. Lamour, D. C. Yost, T. W. Hänsch, N. Kolachevsky, and T. Udem, Science **358**, 79 (2017).

[15] M. Horbatsch and E. A. Hessels, Phys. Rev. A **93**, 22513 (2016).

[16] V. A. Yerokhin and V. M. Shabaev, Phys. Rev. Lett. **115**, 233002 (2015).

[17] U. D. Jentschura, Phys. Rev. A **74**, 62517 (2006).

[18] U. D. Jentschura and P. J. Mohr, Phys. Rev. A **72**, 14103 (2005).

[19] S. Kotochigova, P. J. Mohr, and B. N. Taylor, Canadian Journal of Physics **80**, 1373 (2002).

[20] P. J. Mohr, B. N. Taylor, and D. B. Newell, Journal of Physical and Chemical Reference Data **37**, 1187 (2008).

[21] T. Kinoshita, *Quantum electrodynamics*, Advanced series on directions in high energy physics (World Scientific, 1990).

[22] W. L. Wiese and J. R. Fuhr, Journal of Physical and Chemical Reference Data **38**, 565 (2009).

[23] S. R. Lundeen and F. M. Pipkin, Phys. Rev. Lett. **34**, 1368 (1975).

[24] A. C. Vutha and E. A. Hessels, Phys. Rev. A **92**, 52504 (2015).

[25] K. Kato, T. D. G. Skinner, and E. A. Hessels, Phys. Rev. Lett. **121**, 143002 (2018).

[26] C. W. Fabjan and F. M. Pipkin, Phys. Rev. A **6**, 556 (1972).

[27] S. P. Goldman and G. W. F. Drake, Phys. Rev. A **24**, 183 (1981).

[28] P. C. Thonemann, J. Moffatt, D. Roaf, and J. H. Sanders, Proceedings of the Physical Society **61**, 483 (1948).

[29] V. Isaac, Project report. (Unpublished), York University (2013).

[30] T. Valdez, Project report. (Unpublished) York University (2018).

[31] I. Ferchichi, Project report. (Unpublished) York University (2015).

[32] J. H. Carver and P. Mitchell, Journal of Scientific Instruments **41**, 555 (1964).

[33] A. P. French, *Special relativity*, M.I.T. Introductory Physics Series (W. W. Norton & Company, New York, 1968), pp. 139–144.

[34] A. Marsman, M. Horbatsch, and E. A. Hessels, Phys. Rev. A **96**, 62111 (2017).

[35] S. R. Lundeen and F. M. Pipkin, Metrologia **22**, 9 (1986).

[36] S. J. Orfanidis, *Electromagnetic waves and antennas* (2016).

[37] A. Messiah, *Quantum mechanics*, Vol. 2 (North-Holland publishing company, 1965), p. 726.

[38] S. R. Lundeen, PhD thesis. (Unpublished), Harvard University (1975).